Theses and Dissertations

Fall 2016

Mechanical and micro-structural modeling of trabecular bone by in vivo imaging

Cheng Chen
University of Iowa

Recommended Citation

Chen, Cheng. "Mechanical and micro-structural modeling of trabecular bone by in vivo imaging." PhD (Doctor of Philosophy) thesis, University of Iowa, 2016.
http://ir.uiowa.edu/etd/2193.

Follow this and additional works at: http://ir.uiowa.edu/etd

Part of the Electrical and Computer Engineering Commons

MECHANICAL AND MICRO-STRUCTURAL MODELING OF TRABECULAR
BONE BY IN VIVO IMAGING

by

Cheng Chen

A thesis submitted in partial fulfillment of the
requirements for the Doctor of Philosophy
degree in Electrical and Computer Engineering
in the Graduate College of
The University of Iowa

December 2016

Thesis Supervisor: Professor Punam K. Saha

Graduate College
The University of Iowa
Iowa City, Iowa

CERTIFICATE OF APPROVAL

———————————————

PH.D. THESIS

——————————

This is to certify that the Ph.D. thesis of

Cheng Chen

has been approved by the Examining Committee for the
thesis requirement for the Doctor of Philosophy degree
in Electrical and Computer Engineering at the December
2016 graduation.

Thesis Committee: ———————————————
                  Punam K. Saha, Thesis Supervisor

                  ———————————————
                  Nicole M. Grosland

                  ———————————————
                  Jia Lu

                  ———————————————
                  Erwer Bai

                  ———————————————
                  Xiaodong Wu

ACKNOWLEDGEMENTS

Thank my wife for going through the tough but colorful days during the PhD in Iowa. Cheer for PhD degree for both of us. Never forget support of Mom and Dad.

ABSTRACT

Osteoporosis is a bone disease associated with fracture risk. Accurate assessments of fracture risk, guidelines to initiate preventive intervention, and monitoring treatment response are of paramount importance in public health. Clinically, osteoporosis is defined by low bone mineral density, which explains 65-75% of the variance in bone stiffness. The remaining variability is due to the cumulative and synergistic effects of various factors, including trabecular bone micro-architecture. Osteoporostic imaging is critically important in identifying fracture risks for planning of therapeutic intervention and monitoring response to treatments. In this work, quantitative analysis of trabecular bone micro-architecture using volumetric imaging techniques and computational biomechanical simulation through finite element modeling (FEM) are applied on *in vivo* imaging for various human studies. The ability of imaging methods in characterizing trabecular bone micro-architecture was experimentally examined using MRI and multi-row detector CT. They were found suitable for cross-sectional and longitudinal studies in monitoring changes of trabecular micro-architectural quality in clinical research. A framework which consists of robust segmentation of *in vivo* images and quality mesh generator, was constructed for FEM analysis. The framework was experimentally demonstrated efficient and effective to predict bone strength under limited spatial resolution. The ability of distinguishing bone strengths of different groups were evaluated on various human studies. And the relation between FEM and image-based micro-architectural measures was explored. Quantitative analysis

supports the hypothesis that trabecular bone have distinct structural properties in different anatomic sites and the osteoporosis related change of the micro-architecture also varies. It highlight the importance of standardizing the definition of bone scan locations and the segmentation of such well-defined regions. A shape modeling method was proposed to solve the problem and its application in human proximal femur using MRI were presented. The method was compared with manual segmentation and found highly accurate. Together with tools developed for quantitative analysis, this work facilitates future researches of trabecular bone micro-architecture in different anatomic sites.

PUBLIC ABSTRACT

Osteoporosis is a bone disease associated with fracture risk. Accurate assessments of fracture risk, guidelines to initiate preventive intervention, and monitoring treatment response are of paramount importance in public health. Osteoporostic imaging is critically important in identifying fracture risks for planning of therapeutic intervention and monitoring response to treatments.

Quantitative analysis of trabecular bone micro-architecture using volumetric imaging techniques and finite element modeling (FEM) are applied on *in vivo* imaging for various human studies. The ability of imaging methods in characterizing trabecular bone micro-architecture was experimentally examined using MRI and multi-row detector CT. They were found suitable for cross-sectional and longitudinal studies in monitoring changes of trabecular micro-architectural quality in clinical research.

A framework which consists of robust segmentation of *in vivo* images and quality mesh generator, was constructed for FEM analysis. The framework was experimentally demonstrated efficient and effective to predict bone strength under limited spatial resolution.

A shape modeling method was proposed to solve the problem of standardizing the definition of bone scan locations and the segmentation. The method was compared with manual segmentation and found highly accurate. Together with tools developed for quantitative analysis, this work facilitates future researches of trabecular bone micro-architecture in different anatomic sites.

TABLE OF CONTENTS

LIST OF TABLES

LIST OF FIGURES

LIST OF ALGORITHMS

Algorithm

CHAPTER 1
INTRODUCTION

Osteoporosis is associated with an increased risk of low trauma fractures lead-
ing to increased mortality and morbidity. Its incidence increases progressively with
age [120, 80]. In the United States, about eight million women and two million men
have osteoporosis [102] with medical costs estimated at twenty two billion dollars in
2008 [13].

Osteoporotic imaging is critically important in identifying fracture risks of in-
dividuals for planning of therapeutic intervention and, also, in monitoring response
to treatments. Dual-energy X-ray absorptiometry (DXA) is the clinical standard
technique to classify bone mineral density (BMD) measurements in postmenopausal
women or older men (age 50 years) as osteopenic (T-score less than 1 to greater
than 2.5) or osteoporotic (T-score of 2.5 or lower). DXA BMD accounts for 60 to
70% of the variability in bone strength [177], and the remaining variability is due to
the cumulative and synergistic effects of various factors, including trabecular bone
(TB) micro-architecture [145, 81]. Thus, reliably measuring TB micro-architecture
could be of clinical significance, particularly as trabecular bone may be more sus-
ceptible to hormonal, pharmacological, and toxic effects. There is evidence in the
literature demonstrating that effects of therapeutic agents are greater on TB as com-
pared to overall BMD [9, 38, 175]. Results from several studies support the hypothe-
sis that bone structural metrics representing cortical geometry, individual trabecular
micro-architecture and plate-rod distribution are important determinants of fracture-

risk [81, 118, 9, 38, 8, 87, 139, 97, 99]. Effective measures of TB micro-architecture from in vivo imaging are useful to assess bone strength and fracture risk in the realm of clinical therapy and treatment guidance, including growth and peak bone accrual, aging, post-menopausal bone loss, cancer-related bone loss and conditional bone loss, such as eating disorders, renal osteodystrophy, osteogenesis imperfacta, osteoarthritis, rheumatoid arthritis, corticosteroid medicinal intake, etc [93].

The conventional tool for assessing TB structure is two-dimensional (2D) cross-sectional histomorphometry from bone biopsies [112]. More recently, direct three-dimensional (3-D) analysis of biopsy specimens using micro-computed tomography (μ-CT) has gained interest [19, 64]. μ-CT instruments have maximum resolution on the order of 8 μm isotropic voxels, providing detailed insight into TB micro-architecture. Although it provides the highest resolution while being nondestructive, μ-CT requires bone biopsy, which is rarely indicated clinically and is not suited for monitoring treatment response.

High resolution in vivo imaging techniques provide an advanced tool for understanding of trabecular bone micro-architecture and its properties. Recent advancements in volumetric bone imaging, such as magnetic resonance (MR) [177, 108, 29], high resolution peripheral quantitative computed tomography (HR-pQCT) [17, 24], and multi-row detector computed tomography (MDCT) [95, 139], allow characterization of bone micro-architecture without the need for biopsy. High complexity of TB micro-architecture adds difficulty to construct a limited set of optimum TB micro-architectural metrics comprehensively explaining osteoporotic fracture risks.

Researchers have adopted various topologic and geometric approaches to character-
ize TB architecture using ex vivo and in vivo bone imaging technologies, and linked
their metrics to bone strength and/or fracture risks [113, 169, 65, 62, 51]. These re-
searches reveal that trabecular bone micro-architecture is an important determinant
of bone quality and monitor of fracture risk. A popular and widely used approach
of quantitatively characterization for TB micro-architecture is to classify individual
trabecular plates and rods and assess their compositions and distributions. Also, a
large number of histologic studies [81, 118] have confirmed the relationship between
erosion of trabeculae from plates to rods and fracture risk. Quantitative analysis of
trabecular bone micro-architecture using in vivo imaging is of high influence clinically
and is becoming the mainstream in research.

Another pathway of understanding fracture risk by bone imaging is to estimate
bone strength using computational biomechanical simulation through finite element
modeling (FEM) techniques. Despite the great success FEM has achieved in the
field of bone research using μ-CT [68, 48], application of FEM on *in vivo* imaging
remains a challenging task, due to the limited spatial resolution, and strong partial
volume effect. Specifically, constructing FE models of trabecular bone using clinical
MDCT images often fails due to loss of trabecular structure or filling or marrow holes
which miss represent the topology of trabecular network. Therefore, a reliable and
robust segmentation of trabecular bone network is a fundamental in FEM analysis
for *in vivo* imaging. Besides, in the field of bone research, few attention is paid on
the mesh generation for FEM, while for images of limited spatial resolution, coarse

mesh representation would introduce inaccuracy for FEM simulation. And thus a mesh generator which could guarantee the quality of mesh is also important. FEM and imaging algorithms are both tools to understand trabecular bone properties. However, the interaction between FEM metrics and micro-architecture at the level of individual trabeculae and its implication fracture risk has been somewhat overlooked. The relation between trabecular bone quantitative micro-architectural properties and FEM metrics are of great interests and are explored in this research at human distal tibia using MDCT imaging.

According to Wolff's law, the remodeling of trabecular bone reacts to the load under which it is placed. The remodeling of bone in different anatomical sites will result in varying trabecular micro-architecture with distinct structural properties due to different geometries and shapes of bones where external loads come from various directions. In literature, quantitative analysis have revealed that trabecular networks have shown distinguishable characteristics at different anatomical sites at human distal femur [60]. Even though these anatomical are closely located and conventionally grouped as an intact region. Further understanding of trabecular bone micro-architecture in such particular sites demands an advanced segmentation algorithm to subdivide original region. A shape modeling method was proposed to solve the problem and its application in human proximal femur using MRI are presented in this work.

The overall objective of this research is to develop, validate, and optimize clinically suitable in vivo methods for quantitative assessment of trabecular bone

micro-architectural and mechanical properties over anatomically consistent regions for cross-sectional and longitudinal studies.

Specific aims of this study involve (1) optimization of algorithms for quantitative micro-architectural analysis of trabecular bone at in vivo imaging and studying relationships among micro-architectural properties and various metrics of bone strength at the levels of individual and whole bone, (2) development, validation of methods for FEM of trabecular bone at in vivo CT imaging, and investigating FEM measures in distinguishing various in vivo human groups, (3) development of an automated algorithm to compute subject-specific anatomic regions of interest for regional analysis and comparison of bone measures.

1.1   Trabecular Bone Micro-architecture

Various topologic and geometric analytic approaches have been reported [113, 169, 65, 62, 51, 107] for characterizing TB micro-architecture. Parfitt *et al.* [113] conceived a parallel interconnected plate model of TB yielding bone area fraction, TB volume fraction, spacing, and number from 2-D histomorphometric sections. Vesterby *et al.* [169] conceived a new stereologic parameter, called star volume, which is the average volume of an object region that can be seen from a point inside that region unobscured in all directions. Hahn *et al.* [62] introduced the trabecular bone pattern factor which captures TB connectivity in terms of the convexity property of the TB surface defined as the ratio of the differences in perimeter and area under dilation. Hildebrand *et al.* [65] developed a 3-D structure model index, a function of

global plate-to-rod ratio, based on the observation that the rate of volume change with thickness for a plate is different from that for a rod. Majumdar *et al.* [107] adopted apparent TB number, thickness, spacing and fractal dimension measures to quantify TB structural quality. Feldkamp *et al.* [51] showed that the makeup of TB networks can be expressed in terms of topological entities such as the 3-D Euler number. Stauber *et al.* proposed methods that classifies trabecular bone plate and rod [158, 160, 159]. Saha *et al.* developed digital topological analysis (DTA) [134, 133, 131, 132] to quantify structural properties of TB, based on topological and geometrical characteristics of TB network.

In this work, volumetric imaging algorithms, named Volumetric Topological Analysis (VTA) and Tensor Scale (TS), were applied on *in vivo* imaging to measure the quality of trabecular bone micro-architecture. These two methods compute the plate-width of individual trabeculae in units of micrometers and locally classify individual trabecular type on the continuum between a perfect plate and a perfect rod. Skeleton representation of tarbecular network is first extracted and used as a core step in both methods. Traditional binary skeleton methods require the target as a binary object, while in *in vivo* imaging, the binarization step often introduces data loss. I therefore applied a new fuzzy skeleton algorithm to avoid binarization related data loss. The improvement of skeleton accuracy and the measure of trabecular plate-width in *in vivo* imaging was examined.

The improved method yields accurate and robust measure of plate-widths. We applied the improved VTA method to MRI imaging. The repeat scan reproducibility

of the method was examined using two different in vivo MRI protocols at distal femur and distal radius. In addition, we examined the methods ability to detect testosterone treatment effects on hypogonnadal men in a 2 years follow-up study and the results are presented in Chapter 2. The performance of the method is compared with the conventional methods of digital topological analysis for plate/rod characterization.

In addition to MRI, we are also interested in MDCT imaging. Recent advances in MDCT technology have shown prominent improvements that overcome major deficits of MRI and HR-pQCT related to scan-speed and size of field of view (FOV). MDCT has ultra-fast scan speed and large FOV, which enables researches for whole body study and longitudinal studies with accurate scanning protocols that is easy to achieve clinically. However, in longitudinal studies, researchers often encounter a situation that a new and more advanced CT scanner replaces the older scanner at the middle of the study, which may result in an incomplete process for data acquisition and analysis, or a waste of previous data collected from the older machine. It raises concerns of data uniformity in large-scale multi-site or longitudinal studies that typically involve data from multiple scanners. Therefore, the relation of data between different scanners and the continuity of scientific analysis results remain a question to answer. In particular, we are interested in the relation and consistency of MDCT based TB micro-architectural measures, in the condition of switching scanners. One of the goals of this study is to compare TB micro-architectural measures from two different MDCT scanners to determine if a longitudinal study can jump scanners and still maintain longitudinal continuity. For MDCT imaging, we examine

the effectiveness of two state-of-the-art scanners, namely Definition FLASH and SO-MATOM Force, Siemens (Munich, Germany), in terms of accuracy and reproducibility of derived TB micro-architectural measures as well as their ability to predict actual bone strength. We examine the association of TB measures derived from scans from the two Siemens scanners with notably different spatial resolution features. Finally, we seek the optimum TB imaging protocol for the latest SOMATOM Force scanner, and determine its true spatial resolution feature in terms of modulation transfer function (MTF).

1.2 Finite Element Modeling

Finite element modeling has been widely applied to various medical imaging applications over the past two decades. The remarkable progress in high-resolution imaging techniques draw great research interests in computing trabecular bone stiffness from three-dimensional volumetric imaging using FEM. It is a powerful tool to analyze bone stiffness and reactions under influences of external forces, which provides an insightful understanding of TB behaviors of human activities and helps to model bone deformations and fractures. Advanced bone imaging techniques provide high spatial resolution that enables researchers to build accurate FE models. Among these imaging modalities, μ-CT achieves the highest spatial resolution, but it is invasive to bone. In vivo imaging techniques, including MRI, HRpQCT, and MDCT, draw more research interests. In literature, various FE methods have been reported and applied on MRI [50], HRpQCT [17] and μ-CT [48]. Only a few results [47, 46]

are available on MDCT due to challenging image resolution. Compared with MRI and HRpQCT, MDCT has advantages of fast acquisition, widely availability and capability of visualizing large bone structures, which make it appropriate for clinical use.

This work focused on FEM using MDCT images. It introduced image processing methods to preserve trabecular bone connections under limited resolution for MDCT images and a high quality mesh generator for FEM analysis. The reproducibility of FEM-based bone stiffness on repeat MDCT images is evaluated. We also show the relation between bone stiffness generated by FEM and actual bone stiffness determined by mechanical testing. Our FEM consists of four sequential steps: (1) image processing; (2) surface mesh generation; (3) volume mesh generation; (4) FEM simulation. Output of each step is the input for the next step.

Original volumetric data is not always applicable for FE modeling because medical images contain noise and artificial effects. Therefore proper processing steps are necessary. The difficulty is to avoid eliminating bone structures during noise removal procedures. In other words, preserving the connectivity of TB micro-architecture is important, especially for MDCT images, which are of low spatial resolution. For image processing, novel image processing algorithms for segmentation of treabcular network under in vivo imaging were developed and will be presented in detail in Chapter 3.1.

In the community of bone study, most studies focus on FEM simulations [50, 18], while little attention is paid on the mesh model. Several studies use basic cubic

bricks as the approximation of bone structure model [50, 47, 96]. Some others use Marching Cubes for surface mesh generation. Marching Cubes generates surface mesh with bad triangles that is not satisfactory for FEM simulation and therefore relies on post-processing tools. Several studies rely on commercial software for volume rendition, which limits adoption for automation.

To generate meshes of high quality that suits the FEM analysis, a brief review of mesh generation is presented in this work, with discussing of advantages and disadvantages of different methods. And our framework of FEM mesh model is then introduced. The framework possesses several desirable properties required for FEM simulation: image topology preservation, surface and volume mesh with well-shaped elements. With these properties, the presented framework is also applicable to other types of imaging modalities and various applications. It is also a general tool for FEM modeling in a broader range.

Experiments were designed to evaluate the proposed FEM framework. First of all, the segmentation accuracy was examined by ROI-specific segmentation by human experts and its ability of preserving connectivity of trabecular bone network, as well as marrow spacing was evaluated. With the proper segmentation for *in vivo* MDCT imaging, FEM analysis are then applicable. In a cadaveric study, FEM computed Young's modulus were compared with actual Young's modulus determined by mechanical tests, to validate the ability of the proposed model in prediction of bone strength. The FEM were also applied on *in vivo* experiments which involves several human groups. Compressive modulus and shear modulus were computed on

subject-specific ROIs, in hypothesis that FEM based measures are able to characterize different groups. Finally, the computed FEM measures were compared with bone micro-architectural measures that are computed from volumetrical imaging algorithms to understand their relations. More details are presented in Chapter 3.

1.3   Shape Model and Subregional Segmentation

Osteoporosis is a degenerate bone disease affecting all bones. The bone structure decreases systematically which leads to loss of bone mass and deterioration of micro-architecture. However, the severity of bone loss and deterioration were found different in various anatomic sites in human body. In literature, researchers have shown that bone mass percentage decreases and separation of trabecular structure increases with the increase of distance from the end of bone on human distal radius [143, 106]. Recently, trabecular bone deterioration was found varying along the longitudinal axis of the distal radius [60]. Increasing evidence supports the hypothesis that trabecular bone have distinct structural properties in different anatomic sites and the osteoporosis related change of the micro-architecture also varies.

The differences of trabecular micro-architecture in various regions highlight the importance of standardizing the definition of bone scan locations and the segmentation of such well-defined regions for further study of trabecular micro-architecture for both cross-sectional and longitudinal studies. The ability of locating the same region of interest (ROI) across different patients is the prerequisites in cross-sectional studies. And the accuracy of registering the same ROI on the same patient in longitu-

dinal studies must also be a great impact factor. To facilitate the study of trabecluar micro-architecture in different bone regions, I developed a shape model based method to achieve automatic and robust segmentation. It is noted that the purpose is to subdivide a complete bone region, for example, the proximal femur, into sub-regions that are likely of distinct bone qualities, instead of segmentation of the whole bone region.

In the field of medical imaging, shape models are widely used and proved to be an effective approach for image segmentation [45]. In the past two decades, model-based segmentation approaches have achieved a great success in medical imaging analysis [46]. Shape models are adopted in areas where target objects have similar shapes and structures. Generally, a mean shape, which represents the most significant geometric features of target objects, is generated from a collection of training samples. By matching the mean shape to individual objects, the segmentation is conducted. The shape model makes use of prior information of target objects and are therefore well suited for shapes that are of small variability, for example, in medical fields, lung, tumor, distal and proximal femur. Active shape modeling has achieved success in a few applications, it is still an active research area and suitable for medical applications.

The most common and generic way of representing a shape model is a set of points that capture the most significant features of the shape. Usually, the set of points are referred as landmarks. Let $X = \{L_1, L_2, L_3, \cdots, L_n\}$ denote a vector that contains n landmarks L_1 to L_n. To generate the mean shape is to optimize the vector X that is trained from different samples. However the success of generating a mean shape involves multiple influence factors, such as, the selection of feature points,

manual annotation accuracy, the selection of training shapes, total coverage rate of the eigensystem, etc. More details will be discussed in Chapter 4.

Once the mean shape is obtained, one can register the mean shape onto new shape subjects. The most natural way of registration is point to point matching. Traditionally, dense points matching is required to ensure accuracy of matching. However, the procedure need manual annotation that requires large amount of labor work and expertise in medical fields and anatomical knowledge. Automatic registration is therefore preferred for shape matching. I developed a two-step matching scheme that successfully accomplished the shape matching task. The matching of reference ans target surface enables us to deploy the landmark system defined on the reference shape onto the new shape. Consequently, we constructed correspondence of surface landmarks between two shapes.

To construct a dense volume correspondence, volume meshes were generated inside the object surface. Similar to the correspondence of surface landmarks on reference and target shape, volume landmarks are also paired. We defined a quasi-uniform volume landmark system on the reference shape and deformed it to the target shape using an elastic deformable model. Together with the surface landmark correspondence, a discrete set of dense and quasi-uniform landmarks represents the 3D space R^3. Transformation of volume on the lattice grid Z^3 is then approximated using the transform of landmarks. Landmark correspondence were constructed on a few manual annotated subjects, which are volumes with each subregion marked by an unique label, using the elastic deformable model. The 3D lattice grid Z^3 of the

mean shape is then labeled using averaged labels transformed from each annotated subject to the mean shape space, using the spatial transform determined by landmark correspondence.

Finally, to achieve the ultimate goal, segmentation of volume subregions, the mean shape is deformed to any given new shape. Deformation process follows the surface shape matching and elastic volume deformation. Spatial transform is then determined after the deformation. And labeling of new shape is achieved by transform the labeled lattice grid of the mean shape.

In Chapter 4, we will describe the entire work flow to achieve shape subregional segmentation. Shape subjects are from human femur bone and a new landmark system is defined using anatomic geometrical features determined by experts. Active shape model will be generated using the landmark system defined on training shapes. I will validate the shape model and evaluate its robustness with leave-one-out test. The constructed active shape model is used to achieve shape matching from the mean shape to the target shape, through a two-step matching scheme. The elastic deformation model is presented in detail and its ability for preserving the shape information will be examined. The accuracy of automatic registered sub-regions are examined using those of manual annotations. The system provide an automatic and robust solution for femur bone regional segmentation that can be widely applied on various medical researches.

CHAPTER 2
TRABECULAR BONE MICRO-ARCHITECTURAL ANALYSIS

Osteoporosis is linked to reduced bone mineral density (BMD) and structural degeneration. This bone disease is associated with increased fracture risk, and the fracture-incidence increases progressively with age [80]. The continued increase in life expectancy is predicted to increase in fracture incidence, and Cooper et al. estimated that the annual number of hip fractures will rise to 6.3 million by 2050 [41]. Approximately, 40% of women and 13% of men suffer at least one osteoporotic fracture in their lifetime. Osteoporotic hip fractures reduce life expectancy by 10-20%, and the annual healthcare cost for the United States alone is 19 billion dollars [109]. Although, effective therapies are available for treatment of osteoporosis [82, 173], these therapies are often expensive and associated with side effects [43, 27, 12]. Thus, accurate assessments of fracture risk, clear guidelines to initiate preventive intervention, and monitoring treatment response are of paramount importance in public health [56, 55, 92].

Osteoporostic imaging is critically important in identifying fracture risks of individuals for planning of therapeutic intervention and, also, in monitoring response to treatments. Dual-energy X-ray absorptiometry (DXA) is the clinical standard technique to classify BMD measurements in postmenopausal women or older men (age 50 years) as osteopenic (T-score less than 1 to greater than 2.5) or osteoporotic (T-score of 2.5 or lower). DXA BMD accounts for 60 to 70% of the variability in bone strength [177], and the remaining variability is due to the cumulative and synergistic

effects of various factors, including trabecular bone (TB) micro-architecture [145, 81]. Thus, reliably measuring TB micro-architecture could be of clinical significance, particularly as trabecular bone may be more susceptible to hormonal, pharmacological, and toxic effects [28, 31].

2.1   Quantitative Trabecular Bone Measures

Volumetric topological analysis [139] and tensor scale [136] were previously proposed to characterize TB and quantitatively measure the local structure plate-width at individual voxel in a digitized object, and characterizes the local structure type on the continuum between a perfect plate and a perfect rod. The original VTA algorithm [139] was developed for binary objects requiring thresholding on fuzzy representations of TB images, which is a sensitive and undesired step at in vivo resolution [38]. An improved algorithm for fuzzy TB images was applied to eliminate the thresholding step. Fuzzy skeleton improves accuracy of skeletons, which is also an intermediate step for tensor scale, generated from fuzzy object. Below I will briefly introduce these two methods. Fuzzy skeletonization will also be introduced and its improvement of accuracy will be presented.

2.1.1   Volumetric Topologic Analysis

The overall objective of VTA was to measure the plate-width of individual trabeculae in units of micrometers and locally classify individual trabecular type on the continuum between a perfect plate and a perfect rod (Fig. 2.1(a)). Essentially, the VTA algorithm computes local trabecular plate-width (Fig. 2.1(b)), which is different
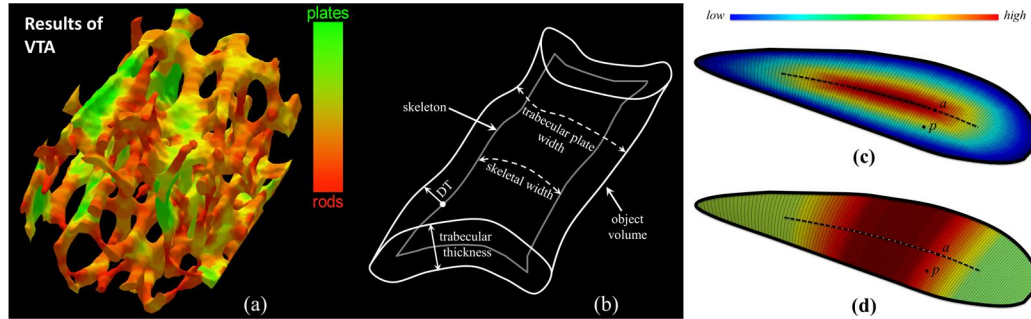
Figure 2.1: (a) Trabecular bone plate/rod classification of trabecular bone using volumetric topological analysis. (b) Various measures on a schematic drawing of a plate-like structure. (c) Color-coded geodesic distance transform from the surface edge, providing one half of the local plate-width at an axial point, e.g. the axial point a; but geodesic distance transform fails to provide local plate-width at a non-axial point, e.g., the point p. (b) Color-coded local plate-width at a non-axial point, e.g., p, is derived from its most-representative axial point, here the axial point a.

from either trabecular thickness or skeletal width. The original VTA algorithm [139] was developed for binary objects requiring thresholding on fuzzy representations of TB images, which is a sensitive and undesired step at in vivo resolution [83]. Here, we present an improved algorithm, which is directly applicable to fuzzy TB images eliminating the thresholding stepa major source of error, especially, at in vivo image resolution.

The VTA algorithm consists of five sequential steps: (1) fuzzy skeletonization, (2) digital topological analysis, (3) geodesic distance transform, (4) geodesic scale computation, and (5) volumetric feature propagation. The principle of VTA is de-

scribed in figures 1(c) and (d). Let us assume that (c) represents the surface skeleton of a plate-like object with varying plate-widths. A surface representation of an object is obtained by surface skeletonization [133, 69]. After surface skeletonization, the VTA algorithm identifies different topological entities, including surface edges (the thick outline in figures 1(c) and (d)), on the skeleton using digital topological analysis. The geodesic distance between two points on a surface skeleton is the length of the shortest path between the two points such that the entire path lies on the skeletal surface. VTA computes the geodesic distance at every surface interior point from its nearest surface edge, which is referred as the geodesic distance transform (GDT) (2.1(c)).

The central dotted line in both (c) and (d) represents the arc-skeleton, and the points on the arc-skeleton are referred to as axial points. Note that, essentially, the computed GDT is equal to the half of the local plate-width at an axial point, e.g. the point a in (d). However, GDT fails to determine the local plate-width at non-skeletal points, e.g. the point p in (c). A feature propagation step is applied, where a non-axial point inherits the local plate-width from its mostrepresentative axial point. For example, the point p is assigned the same plate-width as that of a after feature propagation as illustrated in (d). Finally, another level of feature propagation is applied where the plate-width values are propagated from the surface-skeleton to the entire object volume, e.g. from figures 2(d) and (e). In this paper, we apply fuzzy skeletonization in Step 1 instead of binary skeletonization. Steps 25 are implemented using methods described in our previous work [139]. The feature propagation in
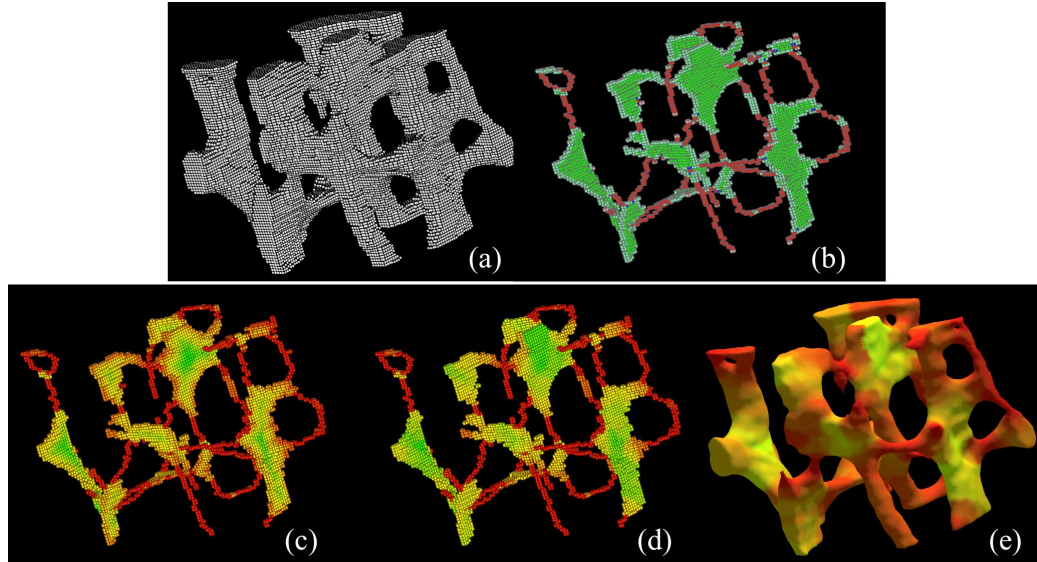
Figure 2.2: Intermediate steps of VTA. (a) A TB region from a μCT image of a cadaveric distal tibia. (b) Classified topolog-ical entities including plates (green), rods (red), edges (light colors), and junctions (blue) on the fuzzy skeleton of (a). (c-e) Color-coded (see 2.1(a) for the color bar) display of geodesic distance transform (c), geodesic scale (d) and surface rendition of VTA results at individual trabeculae (e).

Step 5 is accomplished using the principle established by Liu *et al* [100, 101] that is independent of scan or processing order. Results of intermediate steps of VTA are presented in Fig. 2.2.

2.1.2   Tensor Scale

Tensor scale algorithm [136] is directly applied on a volumetric fuzzy digital object that generates an optimum ellipsoidal representation of the local struc-

ture at each individual curve-skeletal location. This ellipsoidal representation at a curve-skeletal location is used to define different microarchitectural parameters, e.g., local plate-width, platelikeliness, rodlikeliness, orientation etc. of the local trabecula. These local parameters at curve-skeletal locations are propagated to the object volume using the two-level feature propagation approach described for VTA. Two overall parameters in a TB region, namely PW_{TS} and PRR_{TS} were computed similar to PW_{VTA} and PRR_{VTA}, defined in Sec. 2.3 Eqn. 2.8. Although, both VTA and tensor scale methods [140, 136] attempt to measure local structure plate-width, their basic approaches are different. While VTA is a topologic approach based on geodesic manifold path lengths, tensor scale use the geometry of local ellipsoid fits. Therefore we investigate both measures in our experiments. Besides the plate-width measure, the orientation information of tensor scale ellipsoid is used to distinguish between longitudinal and transverse trabeculae. Finally, an overall parameter, namely tBMD was computed as the volumetric BMD in TB regions contributed by transverse trabecular structures. This specific measure is investigated in this work, because, there is evidence suggesting that reductions in the number of transverse trabeculae are associated with marked reduction in bone strength leading to failure due to buckling of longitudinal trabeculae [153].

2.2 Fuzzy Skeleton Improves Skeleton Accuracy on Fuzzy Object

The performance of the TB plate-width computation method is highly dependent on the quality of the surface skeleton generated from the volumetric represen-

tation of a TB network acquired in vivo. Binary skeletonization is always associated with binarization-related data loss adding skeletal inaccuracies such as disruption of trabecular rods, perforation of plates, and filling of small marrow holes. For our studies under *in vivo* imaging conditions, the partial voluming effect introduces apparent fuzziness for the target object. Therefore calibrating fuzziness in skeletonization and avoiding binarization-related data loss could have significant improvements for our studies.

2.2.1 Skeleton In Medical Imaging

Skeletonization provides a compact yet effective representation of an object while preserving important topological and geometrical features; see [122, 126] for thorough surveys on applications of skeletonization. Various implementations of skeletonization following the basic principle of Blum's grassfire propagation are available in literature [122, 152]. Traditional skeletonization algorithms are defined on binary objects. Recently, Jin and Saha [69] have presented a comprehensive solution for skeletonization of fuzzy object using the theory of fuzzy grassfire propagation and collision impact. However, the influence of fuzzy skeletonization in different applications has not been studied.

Image resolution is a major bottleneck in medical imaging. Often, anatomic structures are acquired in the presence of partial voxel voluming. Despite this bottleneck, most medical imaging applications [122, 126] use the binary skeletonization, which is associated with thresholding-induced data-loss and the effects are magnified

at low image resolutions. On the other hand, fuzzy skeletonization may be directly applied on the fuzzy representation of an object in the presence of partially volumed voxels without requiring the binarization step. In this paper, we examine the role of fuzzy skeletonization in measuring trabecular bone (TB) structure-width or plate-width with limited resolution.

The significance of TB plate/rod distribution in assessing osteoporosis and low-trauma fracture-risk has long been recognized in histologic studies [81, 118], which have confirmed the relationship between erosion of trabeculae from plates to rods and higher fracture risk. Various approaches have been reported to distinguish between rod-like and plate-like trabeculae. The volumetric topological analysis (VTA) [139] is an effective and powerful method to quantitatively characterize TB plate/rod [33] by computing local TB plate-width based on topological classification, geodesic distance analysis, and feature propagation on the skeleton of an object. The performance of VTA is highly dependent on the accuracy of the skeleton used for plate-width analysis. The original VTA algorithm [139] was developed for binary objects requiring thresholding on TB images, which is a sensitive and undesired step at *in vivo* image resolution [83].

The purpose of this work is to determine the influence of fuzzy skeletonization on the performance of VTA at *in vivo* image resolution [35], where most bone voxels are partially volumed. More specifically, we examine the accuracy and reproducibility of plate-widths computed using the fuzzy and binary skeletonization-based VTA and analyze their abilities to predict the actual bone strength.

In this section, a few definitions and notations and brief outlines of the fuzzy and binary skeletonization algorithms are presented followed by a short description of the VTA [139] method used for TB plate-width computation. The *3-D cubic grid*, denoted as $\mathbb{Z}^3$, where $\mathbb{Z}$ is the set of integers, is used for image representation; each grid element is referred to as a *voxel*. Conventional definitions of 8- and 4-adjacencies in 2-D and 6-, 18-, and 26-adjacencies in 3-D are followed. This paper starts with the assumption that the target object is fuzzily segmented using a suitable segmentation algorithm [128, 168, 167, 155]. A *fuzzy object* $\mathcal{O} = (O, f_{\mathcal{O}})$ is a fuzzy set of $\mathbb{Z}^3$, where $f_{\mathcal{O}} : \mathbb{Z}^3 \rightarrow [0, 1]$ is the *membership function* and $O = \{p \in \mathbb{Z}^3 | f_{\mathcal{O}}(p) > 0\}$ is its *support*. In this paper, 26-adjacency is used for object voxels, i.e., voxels in O, while 6-adjacency is used for background voxels, i.e, voxels in $\bar{O} = \mathbb{Z}^3 - O$.

2.2.2   Binary And Fuzzy Skeletonization

The fuzzy and binary skeletonization algorithms using morphological erosion under certain topologic and geometric constraints [69, 72, 123, 141, 133, 74] were chosen for our comparative study. This simple yet effective approach, outlined in the following, has become popular [122].

Primary Skeletonization

- Locate all *quench* or *skeletal voxel*s in the input object.

- Filter noisy quench voxels and mark *significant skeletal voxel*s.

- Delete unmarked voxels in the increasing order of distance values while preserving the *object topology* and the *continuity of skeletal surfaces*.

Final Skeletonization

- Convert *two-voxel thick* structures into *single-voxel thin* surfaces and curves.

- Remove voxels with *conflicting topologic* and *geometric* properties.

Skeleton Pruning

- Remove *noisy skeletal branches* with low *global significance*.

Binary Skeletization: In binary skeletonization, a fuzzy object $\mathcal{O} = (O, f_{\mathcal{O}})$ is first binarized into $O_{\text{bin}} = \{p | p \in O \wedge f_{\mathcal{O}}(p) > \text{thr}\}$, which is used as input. A constant threshold value of '0.5' is used for 'thr' for all experiments presented in this paper. During primary skeletonization, the centers of maximal balls (CMBs) [3] are located as *binary quench voxel*s using 3-4-5 weighted distance transform (DT) [16, 15]. The filtering algorithm by Saha *et al.* [133] is applied to remove noisy quench voxels and select significant surface and curve quench voxels. The four-condition constraint of the (26,6) simple point/voxel characterization by Saha *et al.* [123] is applied for topology preservation. Primary skeletonization produces a "thin set" [2] that has at least one background neighbor except at very busy intersections. During the final skeletonization step, two-voxel thick structures are eroded under topology preservation and some additional geometric constraints [141, 133, 4] to generate a one-

voxel thin skeleton while maintaining its overall shape. Finally, noisy skeletal branches are removed during the pruning step using a *global significance measure* [139].

Fuzzy Skeletization: The fuzzy skeletonization algorithm is directly applied on the fuzzy object $\mathcal{O} = (O, f_\mathcal{O})$ without requiring the thresholding step. Here, fuzzy distance transform (FDT) [130] is used instead of binary DT. A *fuzzy quench voxel* [69, 162] is located in a fuzzy object by detecting singularity voxels on the FDT map that holds the following inequality for each 26-neighbor q:

$$\text{FDT}(q) - \text{FDT}(p) < \tfrac{1}{2}(f_\mathcal{O}(p) + f_\mathcal{O}(q))|p - q|, \tag{2.1}$$

where $|p - q|$ is the Euclidean distance between p, q. During the filtering step in primary skeletonization, the measure of *collision impact* ξ_D [69] is used to define the local significance of individual fuzzy quench voxels.

$$\xi_\text{D}(p) = 1 - \max_{q \in N_{26}^*(p)} \frac{f_+(\text{FDT}(q) - \text{FDT}(p))}{\tfrac{1}{2}(f_\mathcal{O}(p) + f_\mathcal{O}(q))|p - q|}. \tag{2.2}$$

Collision impact at a quench voxel relates to the angle where independent fire-fronts collide. The value is high when fire-fronts make a head-on collision. Quench voxels on a core skeletal structure have high values of collision impact, while those on a skeletal branch emanating from a noisy protrusion have low values [69]. Jin and Saha [69] locally characterized the surface- and curve-like fuzzy quench voxels and argued the use of different filtering kernels for them.

For topology preservation, the constraints of 3-D simple pints/voxels [123] are applied on the support of the fuzzy object. Moreover, it is possible to find examples in fuzzy skeletonization, where the criteria of quench voxels and 3-D simple voxels

fail to maintain the continuity of skeletal surfaces. Thus, to ensure the continuity of skeletal surfaces, additional constraints of (8,4) 2-D simple points are applied on each of the three coordinate planes through the candidate voxel [69]. Similar to binary skeletonization, two-voxel thick structures are converted into a single-voxel thin skeleton during final skeletonization. A few thick-voxels survive the first step of final skeletonization, which are eliminated using the conflict between their topologic and geometric properties. Finally, a collision impact-weighted path length of individual skeletal branches is used as their global significance during the pruning step [69].

2.2.3   Experiment and Results

Results of surface skeleton and local plate-width computation from VTA are presented in Fig. 2.3. In general, binary skeletonization over erodes TB surfaces, which makes the computed plate-width lower than true plate-width and results in more rod-like (reddish) trabeculae. Also, binary skeletonization created a few noisy branches (indicated by red arrows) and less-smooth skeletal surfaces (indicated by blue arrows). On the other hand, fuzzy skeletonization generated smoother surfaces and yielded expected measures of plate-width.

Three quantitative experiments were designed to evaluate the following — (1) accuracy, (2) repeat scan reproducibility, and (3) ability to predict bone strength. Computer-generated phantoms were used for Experiment 1. Multi-row detector CT (MD-CT) imaging of cadaveric TB specimens were used for Experiments 2 and 3. For Experiment 3, bone strength of cadaveric specimens was determined by mechanical
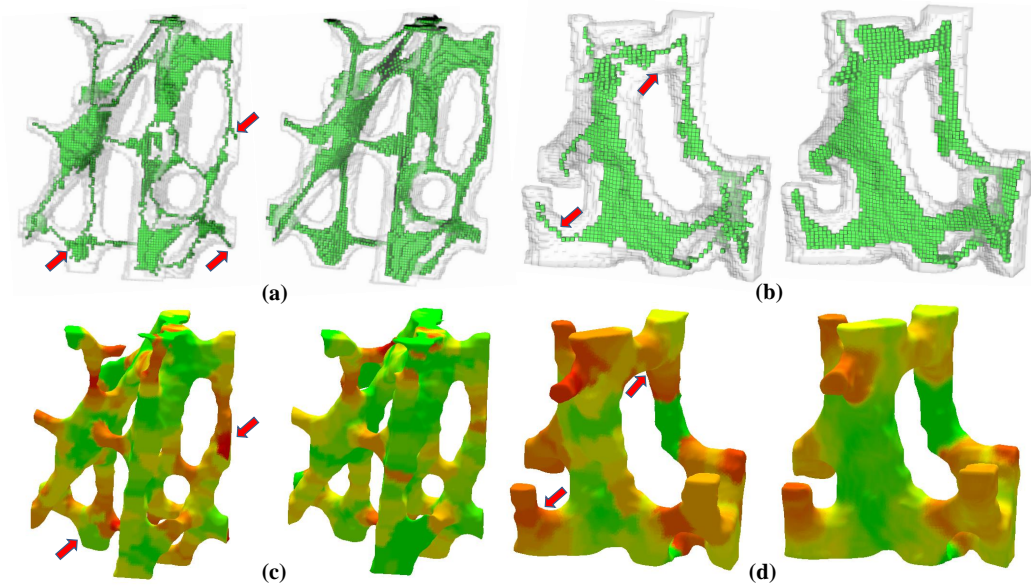
Figure 2.3: Results of binary and fuzzy skeletonization on two small regions from TB images are shown in (a) and (b), respectively. Results of local plate-width on the same image regions using binary and fuzzy skeletonization-based VTA are shown in (c) and (d) respectively. The same color coding bar of Fig.2.1 are used here.

testing.

Computer-Generated Phantoms.

Computerized phantoms with known plate-widths were generated to examine the accuracy of fuzzy and binary skeletonization-based VTA algorithms. First, 3-D binary objects with boundary-noise and their true skeletons were generated at a high resolution over an array of $512 \times 512 \times 512$. Test phantoms were generated from binary objects by down-sampling. The process starts by sampling ideal sinusoids of known skeleton-width, say w_S; let S denote the set of sampled points. A 3-D object V

was computed from S by computing a distance transform from S, thresholding it at a value, say w_d, and, finally, adding random noisy protrusion of three-voxel diameter on the object boundary. The plate-width of the binary object V was recorded as $w_V = w_S + 2 \times w_d$. The test phantom V_{test} was generated by down-sampling V using a $3 \times 3 \times 3$ window to simulate fuzziness. Ten test phantoms were generated with their plate-width $w_V = 3, 5, \cdots, 21$ in the voxel unit of the down-sampled image. For fuzzy skeletonization-based VTA, the test phantom V_{test} was directly used as the input. For binary skeletonization, a threshold of 0.5 was applied on V_{test}.

Cadaveric Specimens and MD-CT Imaging.

Fifteen fresh-frozen human cadaveric ankle specimens were obtained from 11 body donors (age: 55 to 91 years) under the Deeded Bodies Program, The University of Iowa. The ankle specimens were removed at the mid-tibia region. Exclusion criteria for this study were evidence of previous fracture or knowledge of bone tumor or bone metastasis. These specimens were kept frozen until the performance of MD-CT imaging. High resolution MD-CT scans of the distal tibia were acquired on a 128-slice SOMATOM Definition Flash scanner (Siemens, Munich, Germany) using the following CT parameters: single tube spiral acquisition at 120 kV, 200 effective mAs, 1 sec rotation speed, pitch factor: 1.0, nominal collimation: 16×0.3 *mm*, scan length: 10 cm beginning at the distal tibia end-plateau, and total effective dose equivalent to 17 mrem $\approx$ 20 days of environmental radiation in the USA. Images were reconstructed at 0.2 *mm* slice thickness and 0.2×0.2 in-plane resolution using a special U70u kernel achieving high structural resolution. Three MD-CT repeat scans

were acquired for each specimen with repositioning the phantom between scans.

Mechanical Testing for Bone Strength.

To determine TB strength, a cylindrical TB core 8 *mm* in diameter and 20.9±3.3 *mm* in length was cored from the distal tibia *in situ* along the proximal-distal direction. Each TB core was mechanically tested for compression using an electromechanical materials testing machine. To minimize specimen end effects, strain was measured with a 6 *mm* gauge length extensometer attached directly to the midsection of the bone. A compressive preload of 10 N was applied and strains were set to zero. At a strain rate of 0.005 $\sec^{-1}$, each specimen was preconditioned to a low strain with at least ten cycles and then loaded to failure. Yield stress was determined as the intersection of the stress-strain curve and a 0.2% strain offset of the modulus.

2.2.4 Results and Discussion

Accuracy.

To examine the accuracy of computed plate-width, an error was defined as the mean absolute difference between computed and true plate-widths; let $Error_{FSK}$ and $Error_{BSK}$ denote errors of fuzzy and binary skeletonization-based plate-width computation. The mean and standard deviation of $Error_{BSK}$ over ten test phantoms were 1.50±0.15 in the down-sampled voxel unit. The observed mean and standard deviation of $Error_{FSK}$ was 0.40±0.02, a 73% reduction compared to $Error_{BSK}$. A paired t-test result ($p < 0.001$) comfirmed the significance of the error reduction. Also, it is encouraging to note that the mean error of $Error_{FSK}$ is around 0.4 voxel

unit, while the digital localization error in skeletonization is 0.38 [129]. Thus, it may be inferred that the primary source of error in $\text{Error}_{\text{BSK}}$ is digital localization.
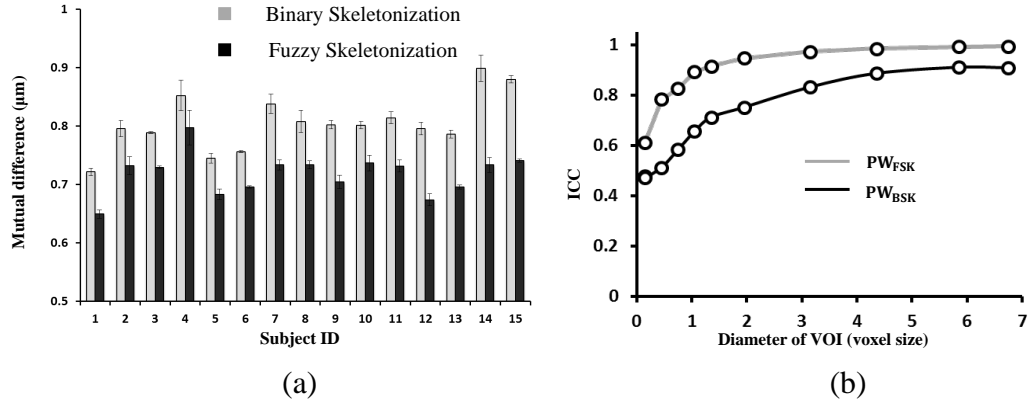
Figure 2.4: (a) Mutual difference between fuzzy skeletons and binary skeletons of three repeat-scan CT images of fifteen cadaveric trabecular bone specimens. (b) Reproducibility of plate-width computed from binary and fuzzy skeleton in three repeat scans of CT images.

Reproducibility.

Two different analyses were performed using the three repeat-scan MD-CT images of fifteen cadaveric TB specimens to examine the reproducibility. First, the mean absolute mutual difference (MAMD) of PW_{FSK} (or PW_{BSK}) was computed over matching regions in post-registered repeat MD-CT scans of each TB specimen. The results of MAMD analysis are presented in Fig. 2.4(a). It is observed that MAMD of PW_{FSK} is consistently lower than that of PW_{BSK} for each TB specimen and a paired t-test confirmed that the reduction in MAMD using fuzzy skeletonization is statistically significant ($p < 0.001$)

The intraclass correlation (ICC) of PW_{FSK} (or PW_{BSK}) was computed over matching spherical volume of interests (VOIs) in post-registered TB repeat MD-
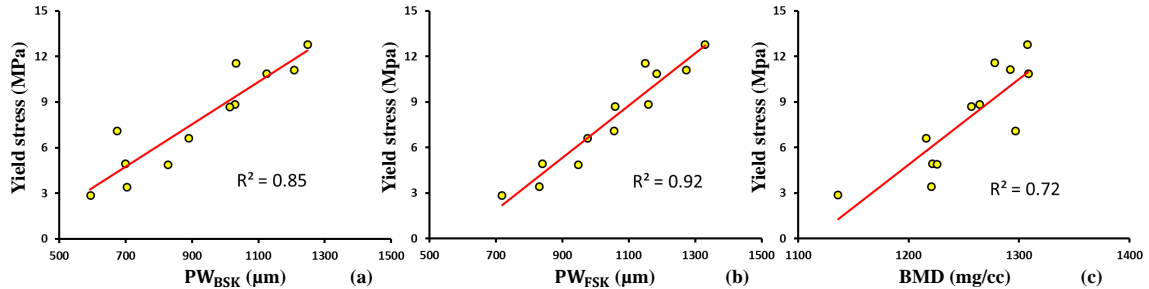
Figure 2.5: Ability of different TB measures to predict experimental bone strength: (a) PW_{BSK} (b) PW_{FSK} (c) BMD. The ability is computed in terms of the R^2 of linear correlation between bone strength and respective measures.

CT scans. Ten spherical VOIs were randomly selected in the first scan of each TB specimen (a total of 150 VOIs). Each VOI was located at least 8 mm proximal to the distal endplate. A post-registration algorithm was used to locate the matching VOIs in the second and third repeat scans. The VOI size was varied, and the ICC values were presented in Fig. 2.4(b) as a function of VOI diameter. The fuzzy skeletonization-based measure PW_{FSK} achieves an ICC of 0.95 at a VOI diameter of 1.05 mm or greater and it converges to the value of 0.98. In contrast, the binary skeletonization-based measure PW_{BSK} achieves the highest ICC value of 0.91 over the range of VOI diameters of our experiment.

Ability to Predict Bone Strength.

Results of correlation analysis between TB yield stress and the average plate-width computed from binary and fuzzy skeletonization are presented in Fig. 2.5. PW_{FSK} achieves the value of 0.92 for R^2 or the coefficient of determination from

linear regression analysis. On the other hand, R^2 of $\mathrm{PW_{BSK}}$ was 0.85. Note that both measures achieves higher linear correlation with yield stress as compared to the simple measure of average bone mineral density (BMD), in which the R^2 was 0.74. This observed results reaffirm the importance of TB plate/rod mirco-architecture as well as the superiority of fuzzy skeletonization over the binary method in capturing TB micro-structural properties at *in vivo* resolution.

In summary, this work has evaluated the role of fuzzy skeletonization in characterizing TB micro-architecture at *in vivo* image resolution. The experimental results have demonstrated that fuzzy skeletonization effectively eliminates the binarization step which is always associated with data loss, especially, at regions with limited resolution. It is experimentally confirmed that fuzzy skeletonization-based TB plate-width is significantly more accurate and reproducible as compared to the binary skeletonization-based measure. Further, it was found in a cadaveric study that the fuzzy skeletonization-based TB plate-width measure has a stronger association with actual bone strength than the binary method. In the context of the specific application, the quality of surface skeleton influences the performance of volumetric topological analysis (VTA) where surface skeleton heavily determines the accuracy of plate-width. The improvement of plate-width using fuzzy skeletonization also indicates that fuzzy skeletonization generates more accurate skeleton than the binary method, possibly, by removing over erosion and false branches.

2.3   Trabecular Bone Micro-architecuture Analysis using MRI

MRI has been successful in measuring trabecular bone micro-architecture [66, 178, 58, 57, 179, 176]. Here, we improved the VTA algorithm using the fuzzy skeletonization algorithm [69] to eliminate data loss in the binarization step and evaluated it on in vivo MRI. The improved method yields accurate and robust measure of plate-widths. We propose a new characterization of plate-like structures using plate-width information. The repeat scan reproducibility of the method was examined using two different in vivo MRI protocols at distal femur and distal radius. In addition, we examined the methods ability to detect testosterone treatment effects on hypogonnadal men in a 2 years follow-up study and the results are presented. The performance of the method is compared with the conventional methods of digital topological analysis for plate/rod characterization.

The following notations are used in this section. Let $O = \{(p, BVF(p)) \mid p \in Z^3\}$ be the bone volume fraction (BVF) representation of a TB image, where Z is the set of integers, Z^3 is the rectangular grid, p is a voxel location, and $BVF(p)$ is the BVF value at p. Let O denote the set of voxels with non-zero BVF, i.e. $O = \{p \mid p \in Z^3 \wedge BVF(p) \neq 0\}$. In the following, we describe the basic principle of the fuzzy skeletonization algorithm, which eliminates data loss in the binarization step and improves the performance.

The performance of our TB plate-width computation method is highly dependent on the quality of the surface skeleton generated from the volumetric representation of a TB network acquired by in vivo imaging. In our previous algorithm, a binary

skeletonization algorithm was used, which is always associated with binarization related data loss adding skeletal inaccuracies such as disruption of trabecular rods, perforation of plates, and filling small marrow holes. Recently, Jin and Saha [69, 75] developed a fuzzy skeletonization algorithm based on fuzzy grassfire propagation, which eliminates binarization related data loss. Blums grassfire transform, originally defined for binary objects, was modified for fuzzy representation of TB images where the BVF is used to define the instantaneous speed of the grassfire front at a given bone voxel. The speed of grassfire front at a given TB voxel p is inversely proportional to its BVF. Using this notion, it can be shown that the fuzzy distance transform (FDT) [130, 138, 40, 137] value at p defines the time that the fire front reaches p. Therefore, the propagation time of a fire front at a TB voxel p to its neighbor q is equal to the local BVF-weighted distance between p and q, and this equality is violated only at skeletal or quench points where the propagation process is interrupted and stopped. Thus, a TB voxel p is a fuzzy quench voxel (Fig. 2.6(c)) if the following inequality holds for every neighbor q of p Following the above definition, a quench voxel fails to pass the grassfire front to any of itsneighbors, and thus, grassfire is extinguished at quench voxels.

Although the fuzzy quench voxel captures medial axes or symmetry structures using the notion of fuzzy grassfire transform, it creates a large number of spurious quench voxels. Spurious quench voxels generate noisy skeletal branches, which are not necessary to describe the overall object shape and topology. Often, such noisy branches add undesired complexities in the skeleton and reduce the effectiveness of
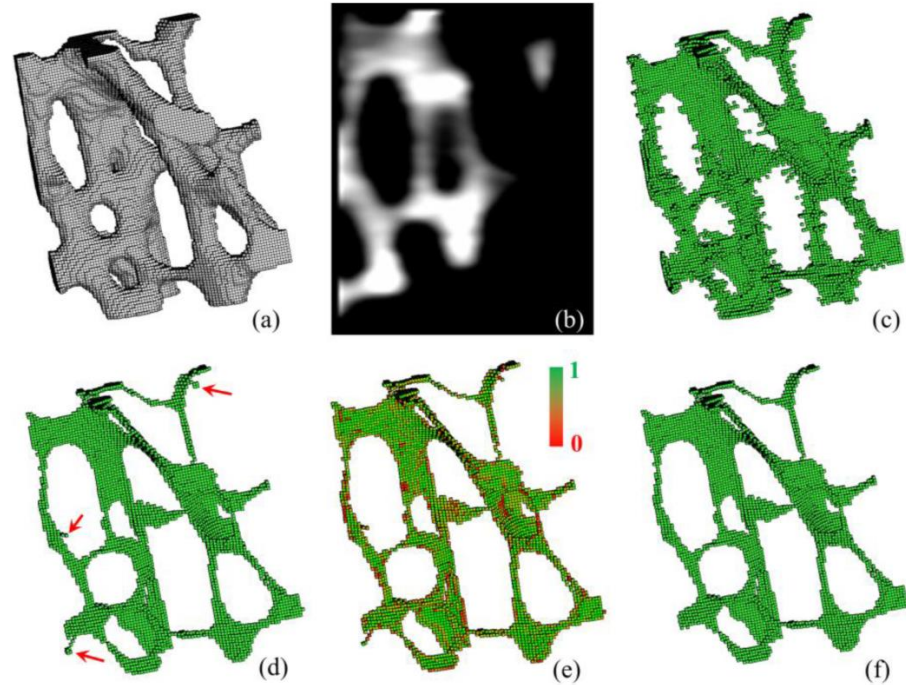
Figure 2.6: Results of intermediate steps of fuzzy skeletonization. (a) 3-D display of TB region in a μ-CT image of a cadav-eric distal tibia specimen. (b) A sagittal image slice displaying the fuzziness in the image. (c) All quench voxels before filtering. (d) Results of final skeleton after filtering noisy quench voxels in (c); red arrows highlight noisy branches. (e) Results of local significance computation. (f) Final results after noisy branch pruning.

skeleton-derived measures. Therefore, it is necessary to remove spurious quench voxels, which is accomplished using their significance measures. Here, a function that resembles the "collision impact" of individual TB voxels is used to determine the significance of a quench voxel as Eqn. 2.2. There are two types of quench voxelsa surface quench voxel where two opposite fire fronts meet and a curve quench voxel where fire

fronts meet from all directions on a plane. These unique geometric properties of a surface or a curve quench voxel, are optimally used to determine its significance based on the collision impact values of its neighboring voxels. For example, a significant surface quench voxel ensures a 3×3 structure of quench voxels with high collision impact in its neighborhood, while a significant curve quench voxel requires a three-voxel curve in its neighborhood with high collision impact. A quench voxel with its significance value above a threshold value thrsignificance, is referred as a significant quench voxel or a fuzzy axial voxel. As illustrated in Fig. 2.6(d), the set of fuzzy axial voxels captures the essential geometry of the original TB object; also, it reduces a large set of non-significant quench voxels of (c).

In this work, the fuzzy skeletonization step starts with identifying the set of all fuzzy quench voxels followed by computation of fuzzy axial voxels using the above filtering method for significant quench voxels. Subsequently, TB object voxels, which are not fuzzy axial voxels, are sequentially removed in the increasing order of their FDT values while preserving the topology of the object. The notion of 3D simple points [132] is used for topology preservation. It should be noted that, despite the filtering of quench voxels, a few spurious branches may survive in the skeleton. Therefore, a post-skeletal-pruning step is applied to prune noisy branches based on their global significance computed as the collision- impact-weighted branch length. Figure 2.6 shows results of intermediate steps of fuzzy skeletonization.

Fuzzy skeletonization reduces binarization related data loss, which improves the preservation of trabecular network connectivity especially at relatively thin tra-
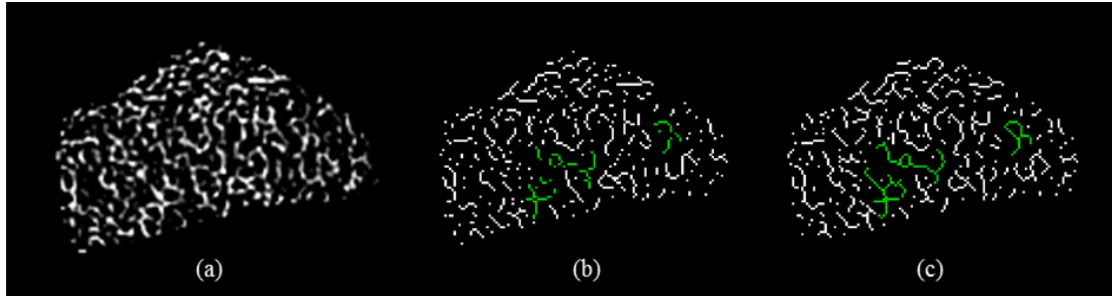
Figure 2.7: Connectivity preservation of TB network using binary and fuzzy skeletonization methods. (a) The BVF map in an axial image of distal radius acquired in vivo at 1.5 T MRI. The regions with relatively thin trabeculae are high-lighted with arrows. (b,c) Results of binary and fuzzy skeletonization. In-plane connectivity loss in the binary skeleton in (b) is highlighted in green; the matching trabeculae in (c) are also highlighted.

beculae. Figure 2.7(a) shows the BVF map of TB network in an axial image slice of distal radius acquired in vivo at 1.5 T MRI. Results of binary and fuzzy skeletonization are presented in (b) and (c), respectively. A few examples of trabecular connectivity loss in the binary skeleton shown in (b) are highlighted in green; the matching regions in the fuzzy skeleton are also highlighted. It should be noted that the examples of in-plane connectivity loss of TB network as shown in (b) do not contradict with 3D topology preservation using simple points [132], which guaranteed by most skeletonization algorithms [122].

Micro-architectural measures.

The output of the VTA algorithm is a local plate-width (PW) function PW :

$O \to R^+$, where $PW(p)$ yields the local TB plate-width in units of micrometers at a given bone voxel $p \in O$, R^+ are real numbers. Three different measures of average bone density, namely, bone volume by total volume (BV/TV), plate-like BV/TV, and rod-like BV/TV, over a target region of interest (ROI) V are defined as follows:

$$\text{BV/TV} = \frac{\sum\limits_{p \in V} \text{BVF}(p)}{V} \tag{2.3}$$

$$\text{BV/TV}_{plate} = \frac{\sum\limits_{p \in V \text{ and } PW(p) \geq \text{TH}_{plate}} \text{BVF}(p)}{V} \tag{2.4}$$

$$\text{BV/TV}_{rod} = \frac{\sum\limits_{p \in V \text{ and } PW(p) < \text{TH}_{plate}} \text{BVF}(p)}{V} \tag{2.5}$$

The threshold TH_{plate} was determined based on observed results of TB BMD distribution over the range of TB plate-width (see Fig. 2.10). A clear deflation of BMD distribution at the platewidth of ~450 μm was noted on all curves in Fig. 2.10. This deflation point of 450 μm was used to determine the threshold separating plate-like and rod-like trabeculae. The platelikeness and rodlikeness measures of a TB voxel p are defined using the eccentricity between the average TB thickness and the local plate-width as follows:

$$platelikeness(p) = \begin{cases} 0, & \text{if } PW(p) < \text{av}_{\text{th}} \\ 1 - \left(\dfrac{\text{av}_{\text{th}}}{PW(p)}\right)^2, & \text{otherwise,} \end{cases} \tag{2.6}$$

$$rodlikeness(p) = 1 - platelikeness(p) \tag{2.7}$$

The parameter av_{th} was determined as the average TB thickness reported in [129]. Note that the platelikeness measure is modelled using the eccentricity of an ellipse;

here the smaller diameter captures the structure thickness, while the larger one represents TB plate-width. It should be emphasized that the above formulation of plate-likeness and rodlikeness requires no threshold value. The average plate-width and plate-to-rod ratio measures are defined as follows:

$$\text{PW}_{\text{VTA}} = \frac{\sum\limits_{p \in O} PW(p)\text{BVF}(p)}{\sum\limits_{p \in O} \text{BVF}(p)} \tag{2.8}$$

$$\text{PRR}_{\text{VTA}} = \frac{\sum\limits_{p \in O} platelikeness(p)\,\text{BVF}(p)}{\sum\limits_{p \in O} rodlikeness(p)\,\text{BVF}(p)} \tag{2.9}$$

Besides the above measure, two measures of TB plate/rod micro-architecture, namely SCR_{DTA} (surface-to-curve ratio) and EI_{DTA} (erosion index), using the conventional method of digital topological analysis were computed using the protocol prescribed in [134].

2.3.1 Experiment

The aims of our experimental plans were – (1) evaluation of reproducibility for in vivo repeat MRI scans using VTA measures at wrist and knee and (2) assessment of the methods ability to detect treatment effects in hypogonadal men subjected to testosterone treatment. For the first experiment, ultra high-field 7 tesla (T) MRI of the distal femur at the right knee as well as 1.5 T MRI of the distal radius at the right wrist were used. For the second experiment, 1.5 T MRI of distal tibia was used.

MR Imaging.

All MR datasets used in this paper were collected in vivo and several properties have previously been published [8, 9, 85, 30]. The knee MRI was collected at New

York University [30]. The right distal femur of each subject was scanned on a 7 T whole body MR scanner (Siemens Medical Solutions, Erlangen, Germany) using a quadrature knee coil (18 cm diameter, transmit-receive). A high-resolution 3D-fast low angle shot (FLASH) sequence was employed to obtain all images (TR/TE = 20/4.5; flip angle 10°; bandwidth 130 Hz/pixel; one signal acquired; 130 axial images with resolution 0.195 mm × 0.195 mm × 1 mm). Scanning time was ~12 min total.

The wrist MRI data for assessment of reproducibility had been acquired previously at the University of Pennsylvania [85]. The right distal radius of each subject was acquired on a Siemens 1.5 T MAGNETOM Sonata MR scanner (Siemens Medical Solution, Erlangen, Germany), with a protocol described in detail in [85]. In brief, 3D fast large-angle spin echo (3DFLASE) sequence (36) yielded 0.137 mm × 0.13 7 mm × 0.410 mm voxel size. The imaging ROI of a 70 mm × 42 mm × 13 mm slab centered 7 mm proximal to the most proximal tip of the epiphyseal line was located during the first visit using a number of low resolution orthogonal 2D localizer sequences. For followup exams, the 13 mm slab was selected by means of prospective registration [117].

For the second experiment assessing the sensitivity of the new bone measures to detect structural abnormalities, prior MRI data of the right distal tibia were re-examined to evaluate the TB micro-structural implications of hormone therapy in hypogonadal men. Full details of the prior studies are in [8, 9].

Subjects.

For the knee reproducibility experiment, MR bone data of four healthy male

subjects (35±7.8 years) [30], without history of fracture, musculoskeletal disorder, or any history of intake of bone altering medication were recruited in the Department of Radiology at New York University. Each subject was scanned twice within the same day with repositioning between scans. For the wrist reproducibility experiment, previously acquired MR data of twenty women (62±8.1 years; 17 postmenopausal, three premenopausal), were used [85]. Exclusion criteria included a history of fracture or treatment for osteoporosis, a body mass index (BMI) greater than 30 kg m^{-2}, and the presence of primary bone cancer or metastases to the bone. Each subject had been scanned three times over the course of 8 weeks with average interval between scans being 20.2 d (standard deviation = 14.5 d).

For the second experiment, TB MR data of a previous longitudinal study [8] on hypogonadal men under testosterone treatment were used. Specifically, 10 previously untreated hypogonadal men (age range: 1880 years) were recruited under that study, and their TB MRI data at baseline, 6, 12, and 24 months visit under testosterone treatment were collected. Full details of human subjects and imaging protocols are given in [8]. In brief: all 10 men had secondary hypogonadism for a duration of more than 2 years with average duration of hypogonadism of 7.9 years (S.D. = 8.2 years). Men were excluded if they had been consuming less than 750 mg of calcium per day as determined by a food frequency questionnaire.

Image Processing.

Image processing steps are as follows: (1) BVF computation, (2) interpolation to 150 m isotropic voxel size, (3) analysis using the improved VTA method, (4) ROI

selection, and (5) computation of TB measures. BVF images were computed using intensity connectivity and a local marrow intensity computation approach without requiring global thresholding. In a BVF image, pixel intensity corresponds to the fractional occupancy of bone. BVF images were resampled using the windowed-sinc interpolation method producing 150 m isotropic voxel size, and the images were subjected to VTA analysis. We first draw the ROI manually on the first MR scan and generated ROIs of follow-up scans using transformation matrices that register original image of the first scan to follow-up scans. The process involves only ROI transformation and avoids interpolation related resolution loss of original BVF images. Finally, we compute proposed measures for each BVF image.

Statistical Analyses.

Statistical analyses that quantitatively assess reproducibility of the VTA derived TB measures in vivo repeat MR scans are: the mean, the root-mean-square of coefficients of variation, and the intra-class correlation coefficient. For each subject, the coefficient of variation (CV) of a given TB measure was calculated across repeat scans. For a given study and a given measure, an average CV was obtained as the root mean square average of CV across all subjects (denoted RMS-CV) to measure the global variability across repeat scans. In addition, the intra-class correlation coefficient (ICC) was computed as a measure of reliability via one-way analysis of variance (ANOVA). To examine a methods ability to detect longitudinal changes in TB micro-architecture in the second experiment, we computed both p-values and effect-size of changes. The effect-size was computed as the mean paired change of a
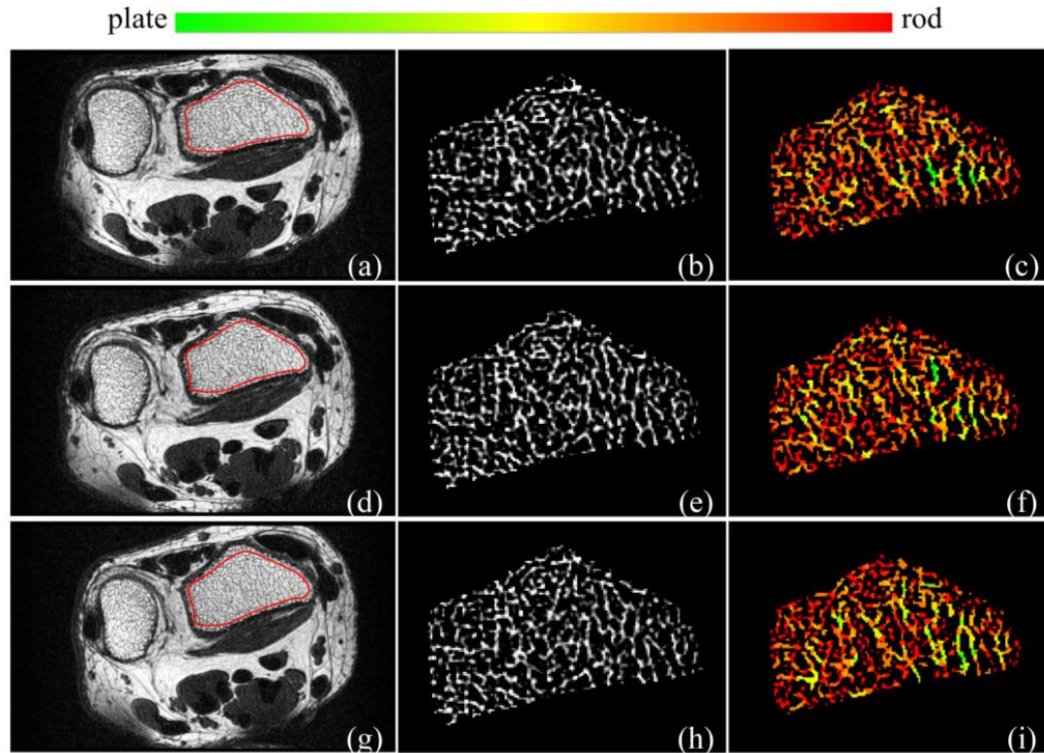
Figure 2.8: Reproducibility of VTA-based characterization of TB plate/rod micro-architecture for in vivo repeat MR scans of the distal radius on a 1.5T whole-body MR scanner: (a) axial image and ROI (red). (b) Bone volume fraction (BVF). (c) VTA-based color-coded plate/rod classification of individual trabeculae. (d-f), (g-i) Same as (a-c) over the matching image slice from the post-registered repeat scan data.

measure between baseline and follow-up normalized by the standard deviation of the paired changes among individual subjects.

2.3.2 Results

Reproducibility of TB Plate/Rod Measures in MR Repeat Scans.

Matching image slices of distal radius from post-registered wrist MR repeat
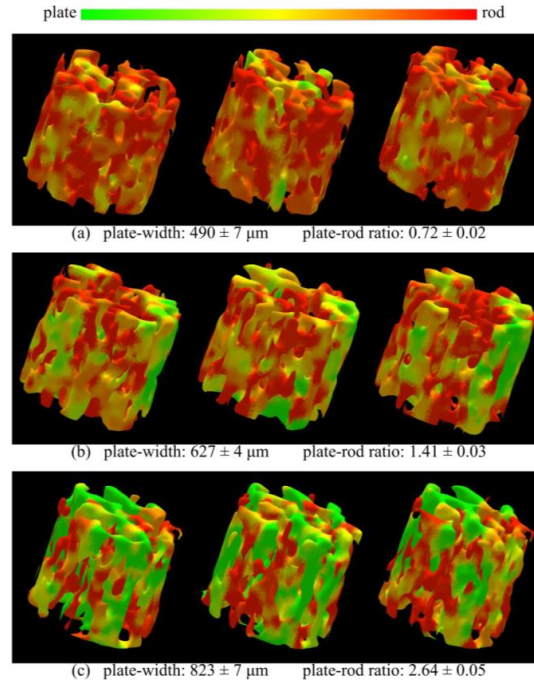
Figure 2.9: Reproducibility of the TB plate-width measure for in vivo MR repeat scans of distal radius. (a) Color-coded 3-D rendition of local TB plate-width in post-registered virtual image cores from three MR repeat scans of a subject. (b,c) Same as (a) for two other subjects with different TB characteristics. For each subject, the mean and stand-ard deviation of the TB plate-width and plate-to-rod ratio measures across three repeat scans are indicated.

scans along with parametric images are shown in Fig. 2.8. Color-coded renditions of VTA plate-rod classification over matching ROIs in three repeat scans of a subject from the wrist study is presented in Fig. 2.9. Quantitative results of the reproducibility study are summarized in table 2.1. RMS-CV values of repeat scans for knee and wrist MRI are in the range of (1.0%, 4.7%) while the intra-class correlation coefficient

Table 2.1: Results of in vivo repeat scan reproducibility analysis for the knee and the wrist MRI studies.

	Knee MRI study			Wrist MRI study		
Parameter	Mean	RMS-CV(%)	ICC	Mean	RMS-CV (%)	ICC
BV/TV(%)	23.9	3.2	0.96	7.1	2.9	0.97
BV/TV$_{plate}$ (%)	19.4	3.9	0.96	4.5	4.0	0.97
BV/TV$_{rod}$ (%)	4.5	2.0	0.96	2.6	4.2	0.96
PW$_{VTA}$ (μm)	937	1.0	0.93	621	2.1	0.95
PRR$_{VTA}$	4.14	1.4	0.94	1.40	4.6	0.96

(ICC) values are in the range of (0.93, 0.97). Similar values of ICC for reproducibility of DTA parameters SCR$_{DTA}$ and EI$_{DTA}$ were reported in [85]. For the knee MRI data, we computed the ICC values for SCR$_{DTA}$ and EI$_{DTA}$ and the observed values are 0.91 and 0.93, respectively.

Effects of Testosterone Treatments on TB Micro-architecture in Hypogonadal Men.

The baseline distribution of trabecular BVF at various TB plate-width among the hypogonadal men used in the testosterone study is presented in Fig. 2.10. Changes in TB plate-rod microarchitecture at different follow-ups under the hormone therapy are presented in Fig. 2.11. Figure 2.11(a) to (d) presents color-coded 3D TB plate/rod micro-architecture over matching ROIs from post-registered distal tibia MRI of a hypogonadal man at baseline, 6, 12, and 24 months follow-ups. Figure 2.11(e) depicts the mean changes in trabecular BVF distributions across TB plate-widths at three
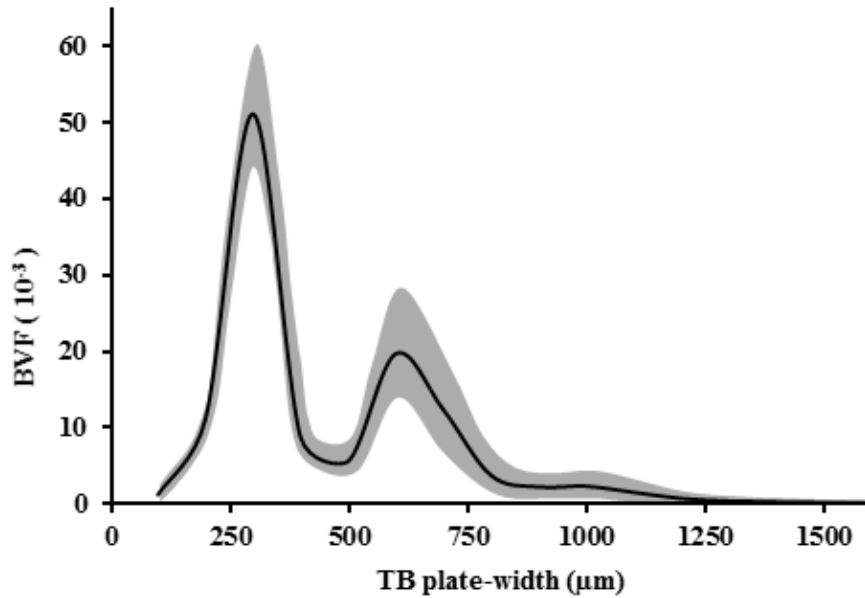
Figure 2.10: The baseline trabecular BVF distribution at various TB plate-widths among hypogonadal men from the testosterone treatment study. The shaded area represents the mean $\pm$ std of trabecular BVF values at corresponding TB plate-width.

follow-up time points; see table 2.2 for quantitative results. Figure 2.12 compares the effect-size of changes in different DTA and VTA measures of TB plate/rod micro-architecture under hormone therapy at baseline, 6, 12, and 24 months followups. High effect-size was observed for the two VTA measures PRR_{VTA} and PW_{VTA} than the two DTA measures surface-to-curve ratio (SCR_{DTA}), erosion index (EI_{DTA}), especially, at 6 and 24 months follow-ups.

Table 2.2: Progressive changes in VTA-based TB measures derived from a 2 years follow-up distal tibia MRI study during testosterone hormone therapy in hypogonadal men.

Baseline	% change			p		
	6 mo	12 mo	24 mo	6 mo	12 mo	24 mo
BV/TV(%)	2.1±4.3	2.1±5.7	6.0±5.7	0.10	0.14	0.005
BV/TV$_{\text{plate}}$ (%)	6.5±10.7	7.2±13.8	16.2±14.7	0.06	0.07	0.003
BV/TV$_{\text{rod}}$ (%)	1.1±3.4	0.7±5.8	2.2±4.7	0.19	0.35	0.09
PW$_{\text{VTA}}$ (μm)	1.9±2.5	2.5±3.5	4.4±3.9	0.03	0.02	0.003
PRR$_{\text{VTA}}$	5.1±8.1	7.3±9.9	14.1±10.7	0.05	0.02	0.001
SCR$_{\text{DTA}}$	1.7±10.6	5.1±6.8	5.2±8.5	0.23	0.02	0.04
EI$_{\text{DTA}}$	-5.3±10.6	-6.1±9.8	-9.2±11.2	0.10	0.04	0.01

2.3.3   Discussion and Conclusion

TB Plate/Rod Measures And Their MR Repeat Scan Reproducibility.

The significance of plate/rod distribution in trabecular bone has long been recognized. A large number of histologic studies [81, 118, 87] have confirmed the relationship between erosion of trabeculae from plates to rods and higher fracture risk. Kleerekoper *et al* [81] found lower mean TB plate density in individuals with osteoporotic vertebral compression deformities compared with a BMD-matched control group without fractures. Recker [118] found differences in TB plate density on two BMD-matched groups with (lower density) and without (higher density) vertebral crush fractures. Various approaches have been reported to distinguish rod-like from
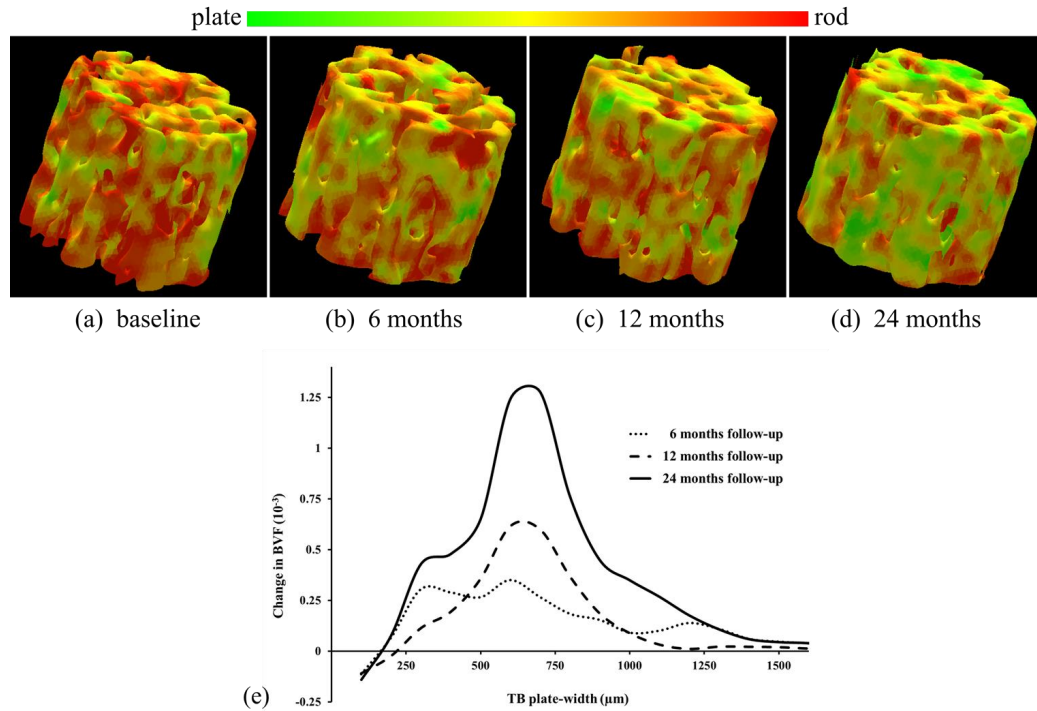
Figure 2.11: Changes in TB plate/rod micro-architecture over a 24-month MRI study monitoring effects of hormone therapy in hopogonadal men. (a-d) Color-coded display of TB plate/rod classification from distal tibia MRI at baseline, 6-, 12-, and 24-month follow-ups. (e) Mean changes of BVF at different TB plate-width in ten hypogonadal men as observed at different follow-ups.

plate-like trabeculae. Hahn *et al* [62] expressed the relation of trabecular plates to rods in terms of the ratio of concave to convex surfaces of the bone pattern in 2D histologic bone sections. Specifically, the ratio of trabecular plates and rods was defined in terms of the ratio of the differences in perimeter and area under a simulated dilation. This line of thought was extended into a direct 3D measure of structure model index [65], where the global plate-to-rod ratio was expressed in terms of the
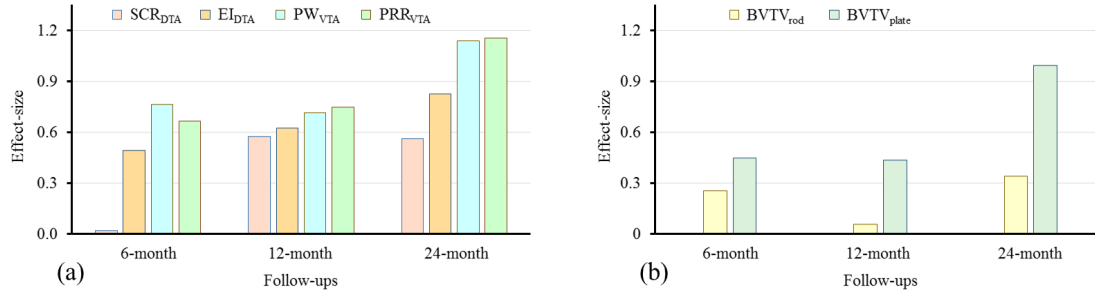
Figure 2.12: Effect-size of changes in different TB measures from MRI at 6-, 12-, and 24-month follow-ups under the testos-terone hormone therapy in ten hopogonadal men.

ratio of volume change with thickness under simulated 3D dilation. Notably, however, these prior studies were all based on bone biopsies.

In previous work, Saha and his colleagues developed DTA [132, 131, 133, 134] that characterizes topological plates, rods, and junctions at individual TB voxels. This method was applied to in vivo studies assessing implications of hormonal changes [8, 175] or renal osteodystrophy [179] on TB plate-rod micro-architecture. DTA based assessment of TB micro-architecture revealed reduced trabecular plates in subjects with vertebral fracture [98] or deformity [174]. However, a major limitation of the DTA method is that resulting classifications are inherently discrete, failing to distinguish between narrow and wide plates. The balance between plates and rods during bone formation at younger ages, as well as during bone loss or anti-resorptive treatment, changes gradually and, therefore, demands classification of TB micro-architecture on the continuum between a perfect plate and a perfect rod. Also,

theoretically, the discrete TB plate/rod classification by DTA is sensitive to image voxel size. For example, a trabecula classified as rod at one voxel size may be classified as a plate at a smaller voxel size. In contrast, the VTA algorithm solved the problem by computing local plate-width in the units of micrometers for individual trabeculae. Color-coded illustrations of the TB network in Fig. 2.8 and 2.9 confirm the methods ability to classify individual trabeculae on the continuum between a perfect plate and a perfect rod. Regional agreements of TB plate/rod classification in repeat MR scans are visually observed in these figures. The three rows in Fig. 2.9 represent repeat scans of TB from three different subjects with distinct trabecular plate/rod composition. The method successfully represents the large difference across the three subjects and shows much smaller variance at repeat scans. In the discussion of effects of testosterone treatment on TB micro-architecture in hypogonadal men, we also compared DTA with VTA in measuring quality changes of TB micro-architecture.

It is noted in table 2.1 that RMS-CV values are small for all TB measures for both the knee and the wrist MRI studies. The lowest RMS-CV value of 1.0 was observed for the core VTA measure PW_{VTA}, which indicates that the PW_{VTA} measure is reproducible with 1.0% variability relative to its mean value. The ICC, i.e. the variability of the measure relative to the range of values obtained across the population, was found to be 0.93 and 0.95 for the same measure for the two studies. PRR_{VTA} shows somewhat greater RMS-CV since the variability in both platelikeness and rodlikeness measures are combined in this ratio measure (see Eqn. 2.8). However, the observed ICC values of PRR_{VTA} are similar to those of PW_{VTA}, which suggests

that the across-population variation of PRR_{VTA} is higher than that of PW_{VTA}. High reproducibility of the VTA measures establishes their suitability for clinical or research studies including multi-center studies and longitudinal ones where multiple follow-up scans are needed.

Beyond the measures given in table 2.1, the method yields unique information on the distribution of BV/TV at different values of trabecular plate-width (Fig. 2.10). These distributions provide insight into the pathogenesis of bone degeneration (or, development) process at the level of TB micro-architecture. For example, besides early detection of trabecular bone conversion from plates to rods, the method is potentially capable of distinguishing gradual conversion of trabecular plates to rods from rapid perforation of trabecular plates. We observed that there is an apparent separation gap at around 450 m, which differentiates rod- and platelike trabeculae.

Effects of Testosterone Treatments on TB Micro-architecture in Hypogonadal Men.

Benito *et al* [9] reported the results of a 2 years follow-up study examining the effects of testosterone replacement treatment on TB micro-architecture using the same imaging tools. The MR image from these two studies were re-analyzed using the improved VTA algorithm. Here, we present the result and compare it with DTA in assessing effects of testosterone treatment on TB micro-architecture among hypogonadal men.

Figure 2.10 presents the distribution of TB volume at different plate-widths for hypogonadal men at different time-points in the follow-up study. Here, the VTA

algorithm provides unique information not obtainable by DTA or any other existing tools. Figure 2.11(a)(d) depicts the change in TB micro-architecture over a matching ROI for a hypogonadal subject during the 2 years treatment period. A gradual and progressive shift in trabecular composition toward more plate-like structures is noted in the figure. The quantitative results of table 2.2 confirm this effect on TB micro-architecture of the hormone treatment. The mean plate-width PW_{VTA} and plate-to-rod ratio PRR_{VTA} showed statistically significant changes as early as 6 months of the treatment. After 24 months of treatment, all TB measures showed statistically significant improvements, except BV/TV_{rod} over rod-like trabeculae. BV/TV_{plate} was found to increase 6.5% at the 6 months but did not quite reach significance ($p = 0.07$). Distributions of changes in BVF at different trabecular plate-width during the 2 years treatment period are presented in Fig. 2.11(e). At 12 and 24 months follow-ups, there is apparent increase in BVF around $\sim$625 μm plate-width, which is close to the mean TB plate-width observed in table 2.1. In table 2.2, quantitative results of changes for 2 years follow-up study on hypogonadal men during testosterone hormone therapy are presented. Figure 2.12 presents the effect-size of changes of VTA and DTA measures at different follow-ups.

The above results shed light on the mechanism of hormone therapy in terms of TB microarchitecture. A net increase in BV/TV_{plate} occurs due to gradual conversion of TB rods into plates under hormone therapy, and the shift is detectable as early as at 6 months. On the other hand, the relative constancy of the BV/TV_{rod} measure is associated with the uncertainty of the balance between the rates of rod to plate

conversion and generation of new TB rods. While the conversion of TB rods to plates decrease rod density, generation of new TB rods increases it. These two opposite effects nearly cancel each other.

There is histologic evidence demonstrating improvements in TB microarchitecture in hypogonadal men after testosterone treatment. Baran *et al* [6] reported increases in relative osteoid volume, total osteoid surface, linear extent of bone formation, and bone mineralization in an osteoporotic hypogonadal male after 6 months of testosterone replacement. Francis *et al* [53] observed increased total and free plasma 1,25-dihydroxyvitamin D in hypogonadal men on testosterone treatment, and bone biopsy at 6 weeks after treatment confirmed increase in skeletal retention of calcium and bone formation by testosterone treatment. It is in accordance with our observations of positive changes in TB micro-architectural changes after testosterone treatment. The early detection of positive changes in TB microarchitecture using VTA in hypogonadal men after 6 months of testosterone treatment (table 2.2) suggests that VTA may be a more responsive or sensitive way to monitor osteoporosis or treatment effect as compared to DTA or BV/TV, which required more time to detect treatment effects. Specifically, as compared to DTA measures, two VTA measures plate-width PW_{VTA} and plate-to-rod ratio PRR_{VTA} show statistically significant changes under treatment at 6 months, while none of the DTA measures produced significant difference at 6 months. In addition, VTA offers resolutionindependent measures in units of micrometers, and insight into the mechanism of a treatment at the level of individual trabecular plate/rod micro-architecture.

In summary, We improved the VTA algorithm to eliminate data loss in the binarization step using fuzzy skeletonization. The method offers reproducible measures of TB plate/rod micro-architecture at in vivo MRI. It computes local plate-width and characterizes individual trabeculae on the continuum of a perfect plate and perfect rod. The method yields the width information of individual trabeculae and offers an insight speculation into the bone structure at micrometer level, which existing tools are not able to provide. By studying a group of human subjects, we observe a pattern of width distribution of human TB. The method is suitable for cross-sectional and follow-up studies toward answering clinical and biological questions. The method should be equally suited for studies with other modalities providing trabecular bone images with limited spatial resolution, including high-resolution CT. However, evaluation of the methods full potential requires drug intervention studies in larger cohorts of patients.

The method presented in this paper is based on direct microstructural analysis of TB network in high-resolution MR imaging, and provides measures of plate/rod distribution of individual trabeculae. Unlike the indirect methods, the morphologic interpretations of our measures are well defined, and histologic evidence confirms the relationship between osteoporosis and the gradual conversion of trabecular plates to rods, a process well known to increase fracture risk. Further, our method offers plate/rod characterization at the level of individual trabeculae, which may be useful as a regional biomarker, especially, in recognizing heterogeneous bone loss. Lastly, it would be worthwhile to compare the relationship between highresolution image-based

direct morphologic measures of TB micro-architecture and indirect MRI measures and their strengths and weaknesses in assessing fracture risk and their ability to monitor disease progression or response to treatment.

2.4   Trabecular Bone Micro-architecuture Analysis using MDCT Imaging

State-of-the-art volumetric bone imaging modalities, including magnetic resonance imaging (MRI) [177, 107, 94, 29] and high resolution peripheral quantitative computed tomography (HR-pQCT) [17, 83, 25], have been investigated for quantitative assessment of bone microarchitecture at peripheral skeletal sites. Despite considerable efforts and successes, these techniques suffer from slow-speed scanning causing motion artifacts [17, 105, 77], smaller field of view (FOV) susceptible to positioning error [105, 20], need for a specialized scanner and/or associated hardware, and, in the case of MRI, failure to provide quantitative BMD. Recent advances in multi-row detector CT (MDCT) technology have shown prominent improvements that overcome major deficits of MRI and HR-pQCT related to scan-speed and FOV. A state-of-the-art MDCT scanner, specifically, Siemens SOMATOM Force, achieves xy-plane 10% modulation transfer function (MTF) of 30.0lp/cm $\approx$ 167 μm true in-plane resolution and z-plane 10% MTF of 17.7lp/cm $\approx$ 282 μm true z-plane resolution using ultra-high resolution (UHR) mode. This scanner acquires a 10 cm scan-length at a peripheral site using the UHR mode in just 6sec as compared to $\sim$2.9min for 0.9cm scan-length using HR-pQCT [23]. Also, it offers major dose reduction while

simultaneously increasing spatial resolution and SNR. If MDCT is established as effective for quantitative bone microarchitectural imaging, its wide availability in clinical environments will immediately put it as a front runner for large multi-center bone studies.

A pertinent challenge with CT for bone research emerges due to wide variation in imaging and reconstruction features from different vendors and rapid upgrades in technology. It raises concerns of data uniformity in large-scale multi-site or longitudinal studies that typically involve data from multiple scanners. In longitudinal studies, researchers often encounter a situation that a new and more advanced CT scanner replaces the older scanner at the middle of the study, which may result in an incomplete process for data acquisition and analysis, or a waste of previous data collected from the older machine [61, 71, 73]. Therefore, the relation of data between different scanners and the continuity of scientific analysis results remain a question to answer. In particular, we are interested in the relation and consistency of MDCT based TB micro-architectural measures, in the condition of switching scanners. One of the goals of this study is to compare TB micro-architectural measures from two different MDCT scanners to determine if a longitudinal study can jump scanners and still maintain longitudinal continuity.

In this section, we examine the effectiveness of two state-of-the-art scanners, namely Definition FLASH and SOMATOM Force, Siemens (Munich, Germany), in terms of accuracy and reproducibility of derived TB micro-architectural measures as well as their ability to predict actual bone strength. Also, as mentioned earlier, we

examine the association of TB measures derived from scans from the two Siemens scanners with notably different spatial resolution features. Finally, we seek the optimum TB imaging protocol for the latest SOMATOM Force scanner, and determine its true spatial resolution feature in terms of MTF.

2.4.1 Methodology

The overall objective of our experiments is to evaluate the role of a state-of-the-art MDCT imaging technology in computing TB microarchitectural metrics at a peripheral sites. Specifically, the methods and experiments were designed to perform the following tests on a Siemens SOMATOM Force scanner.

(1) To examine the accuracy and reproducibility of TB microarchitectural measures computed using MDCT imaging at a peripheral site, namely distal tibia, and to assess their ability to predict actual bone strength.

(2) To determine if a longitudinal study can jump two different MDCT scanners and still maintains longitudinal data continuity.

(3) To determine the optimum MDCT imaging protocol in a state-of-the-art Siemens SOMATOM Force scanner achieving the highest spatial resolution.

To comprehensively perform these tests, the following materials and methods were used (1) cadaveric ankle specimens, (2) UHR MDCT scanning of distal tibia specimens under in vivo conditions using Siemens Definition FLASH and Siemens SOMATOM Force scanners, (3) micro-CT scanning of cadaveric ankle specimens, (4) mechanical testing on cadaveric ankle core specimens determining their strengths and

elastic moduli, (5) UHR MDCT ankle scans of healthy volunteers on two different scanners at a short time gap, (6) image processing and computation of TB microarchitectural metrics, and (7) estimation of modulation transfer functions (MTFs) of two scanners at different scan protocols. The overall design of materials and methods of our experiments are summarized in Fig. 2.13.
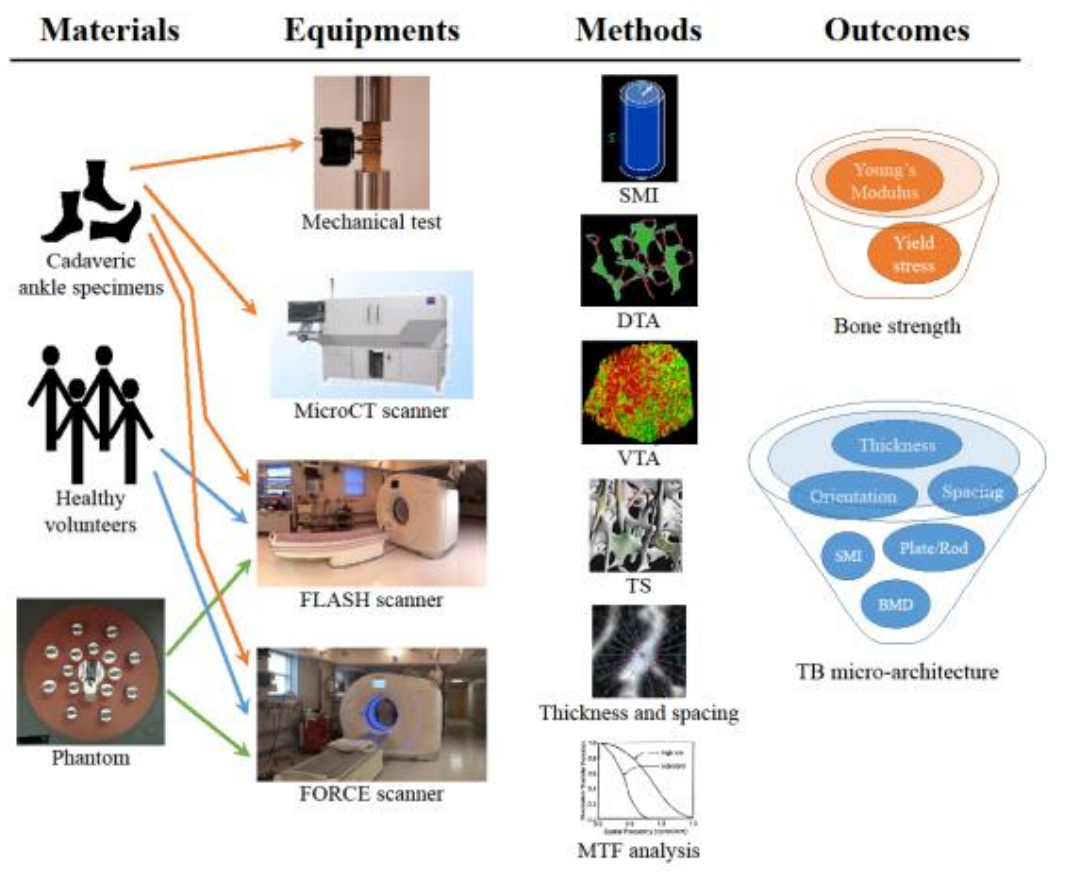
Figure 2.13: The overall design of methods and materials used in the current study.

2.4.1.1   Study Groups

Cadaveric Ankle Specimens.

Twenty-two fresh-frozen cadaveric ankle specimens were removed at mid-tibia from seventeen body donors (age at death: 79.6±13.2 yr; 8 males, 9 females). Those bodies were collected under the Deeded Bodies Program at The University of Iowa, Iowa City, IA. Exclusion criteria were evidence of previous fracture or knowledge of bone tumor or bone metastasis. After collection, these specimens were placed in a sealed plastic bag and kept frozen until MDCT imaging. This set of twenty-two specimens, referred to as Specimens A, was used for repeat UHR MDCT imaging on a Siemens Definition Flash scanner as well as for micro-CT imaging and mechanical testing. Another set of three ankle specimens from two body donors, referred to as Specimens B, was collected and used for repeat MDCT scans under each of numerous CT scan protocols on the Siemens SOMATOM Force scanner.

Healthy Volunteers.

MD-CT distal tibia scans were obtained for twenty healthy volunteers (age: range 35 to 20; 26.2±4.5 years; 10 females) in two state-of-the-arts scanners. This study was designed around the transition period of the MDCT scanner upgrade at the University of Iowa Comprehensive Lung Imaging Center (ICLIC) research CT facility. First, each volunteer was scanned in old scanner before upgrade who were recalled after upgrade and rescanned in the new scanner. The range of time gaps between the two scans on an individual participant was 48 to 40 days with the meanstd. 44.6±2.7 days. All experiments involving human subjects were approved by The University

of Iowa Institutional Review Board and all participants provided written informed consent.

2.4.1.2   Ultra-High Resolution MDCT Imaging

UHR MDCT scans of distal tibia using two state-of-the-arts scanners (old scanner: Siemens Definition FLASH, Munich, Germany; new scanner: Siemens SO-MATOM Force, Munich, Germany) were used for experiments. For both scanners, imaging experiments were performed at ICLIC. UHR mode: Both FLASH and Force scanners have two 64 rows of 0.6 mm detectors. The highest resolution single gun scan mode was used, which activates the 32 inner most 0.6 mm detectors to maximize beam quality. Siemens double z-sampling allows for a dual sampling of the 0.6 mm detectors, splitting the signal so that each detector creates a 0.3 mm slice in the z-plane [115, 52]. The UHR scan mode provides a more accurate slice profile and lowered partial volume artifacts enabling high image detail with a maximum achievable in-plane as well as z-plane resolutions. For both scanners, a scan-length of 10 cm beginning at the distal tibia end-plateau were used; an AP projection scout scan of the entire tibia was acquired to locate the field of view. A Gammex RMI 467 Tissue Characterization Phantom (Gammex RMI, Middleton, WI) was scanned to calibrate CT Hounsfield units into BMD (mg/cm^3). Scanner-specific CT parameters are described in the following.

FLASH Scanner.

Single tube spiral acquisition at 120 kV, 200 effective mAs, 1 sec rotation speed,

pitch factor: 1.0, nominal collimation: 16×0.3 mm, total effective dose equivalent: 170 μSv $\approx$ 20 days of environmental radiation in the US. After scanning in a helical mode with a 0.4 mm slice thickness, data were reconstructed at 0.2 mm slice thickness using a normal cone beam method with a special U70u kernel achieving high structural resolution.

FORCE Scanner.

Single X-ray source spiral acquisition at 120kV, 200 effective mAs, 1sec rotation speed, pitch = 1.0, and nominal single collimation width of 0.6mm, total effective dose equivalent: 50 μSv $\approx$ 5 days of environmental radiation in the US. Images were be reconstructed at 0.3 mm slice-thickness with 0.2 mm slice-spacing and 0.1 mm pixel-size using Siemenss special kernel Ur77u with Edge Technology to achieve high spatial resolution. For the cadaveric ankle specimens in Specimens B, MDCT scans the effective mAs of 100 and 50 and the pitch of 0.85 were also collected.

2.4.1.3 Mechanical Testing of Specimens

A cylindrical TB core was harvested from each of the twenty-two distal tibia sample of Specimens A, and compressive mechanical tests were performed. Youngs modulus (E) of each specimen was determined using an extensometer test, while the Yield stress was determined in a platen test. The platen test was performed because during the first test, most TB cores failed near their ends rather than within the extensometer span. Therefore, specimen lengths were shortened to obtain more homogeneous properties across each length. All specimen preparation and mechanical

testing were performed at the University of Iowas Orthopaedic Biomechanics Laboratory.

Specimen Preparation.

Cylindrical TB specimens of nominally 8 mm in diameter were cored from distal tibia in situ along the proximal-distal direction. A-P and M-L radiographs were first used to determine the central axis of the bone and thus the core location and to ensure elimination of the growth plate from a test specimen. Specimen were cored with saline immersion using an 8.25 mm inner diameter diamond coring bit (Starlite Indus- tries, Rosemont, PA). The core was released from the distal radius by cutting it with a razor saw, and the specimen ends were sanded smooth, flat, and parallel. Specimen length and diameter were measured three times and averaged, and the middle 6 mm of the specimen length was marked for extensometer attachment position. Each core was wrapped in saline-soaked gauze, and frozen until thawed for testing. For the non-extensometer testing, the specimen ends were again sanded to remove damaged bone from the specimen ends. For extensometer testing, a minimum specimen length of 18 mm was desired, to achieve both the minimum aspect ratio of 2:1 recommended for TB compression specimens [79] and a 3:1 ratio of specimen length to extensometer gage length used in an earlier study [78]. For the subsequent platen testing, specimen length was dependent on how much bone needed to be removed from the damaged ends; the resulting aspect ratios were all greater than 1:1.

Mechanical Testing.

The TB cores were mechanically tested in compression using an electrome-

chanical materials testing machine (MTS Insight, MTS Systems Corp., Eden Prairie, MN). Each specimen was placed between unlubricated, polished, plano-parallel steel platens. For the extensometer test, to minimize specimen end effects, strain was measured with a 6 mm gage length extensometer (model 632.29F-30, MTS Systems Corp., Eden Prairie, MN) attached directly to the mid-section of the bone. For the second test, strain was measured with the testing machine at the compressing platens. A compressive preload of 10 N was applied and strains then set to zero. At a strain rate of 0.005 s^{-1}, each specimen was preconditioned to a low strain with at least ten cycles and then loaded to failure. Youngs modulus was determined for each specimen as the highest 20% section slope of the stress-strain curve. Yield stress was determined as the intersection of the stress-strain curve and a 0.2% strain offset of the modulus.

2.4.1.4 Imaging Processing and TB Microarchitectural Metrics

The complete list of TB measures investigated in this study is shown in Table 2.3. Each MD-CT image was processed through an image-processing cascade in the following sequence (1) conversion of CT Hounsfield unit (HU) numbers to bone mineral density (BMD) (unit: mg/cm^3) and computation of vBMD , (2) interpolation at isotropic voxels, (3) selection of volumes of interest (VOIs), (4) fuzzy skeletonization and computation of TB network area density (NAD), (5) digital topological analysis for computation of erosion index (EI_{DTA}), (6) volumetric topological analysis for computation of TB average plate-width (PW_{VTA}) and plate-to-rod ratio (PRR_{VTA}), (7) tensor scale analysis for computation of TB average plate-width

Table 2.3: List of MDCT-based TB measures examined in this study.

Parameter (unit)	Description
vBMD (mg/cm^3)	Volumetric trabecular bone mineral density
tBMD (mg/cm^3)	Volumetric BMD contributed by transverse trabeculae
NAD (cm^{-1})	Trabecular bone network area density
EI$_{\text{DTA}}$ (no unit)	Trabecular bone erosion index computed using DTA
PW$_{\text{VTA}}$ (μm)	Trabecular bone average plate-width computed using VTA
PRR$_{\text{VTA}}$ (no unit)	Trabecular bone plate-to-rod ratio computed using VTA
PW$_{\text{TS}}$ (μm)	Trabecular bone plate-width computed using tensor scale
PRR$_{\text{TS}}$ (no unit)	Trabecular bone plate-to-rod ratio using tensor scale
TB-Th (μm)	Trabecular bone average thickness
TB-Sp (μm)	Trabecular bone marrow spacing
SMI (no unit)	Trabecular bone structural model index

(PW$_{\text{TS}}$) and plate-to-rod ratio (PRR$_{\text{TS}}$) and trabecular BMD contributed by transverse trabeculae (tBMD), (8) star-line analysis for computation of TB thickness (TB-Th) and spacing (TB-Sp) measures, and (9) computation of structure model index (SMI). These image processing methods are briefly described in the following.

BMD Computation and Isotropic Voxel Interpolation.

An MDCT scan of a Gammex RMI 467 Tissue Characterization Phantom (Gammex RMI, Middleton, WI) was performed after scanning a cadaveric specimen or a human subject with the matching CT protocol and reconstruction kernel. The calibration phantom contains sixteen cylinders with known physical densities; see Fig. 2.14(a). A fully automated algorithm was developed in our laboratory to locate and segment those cylinder using their known dimensions and relative locations. Each
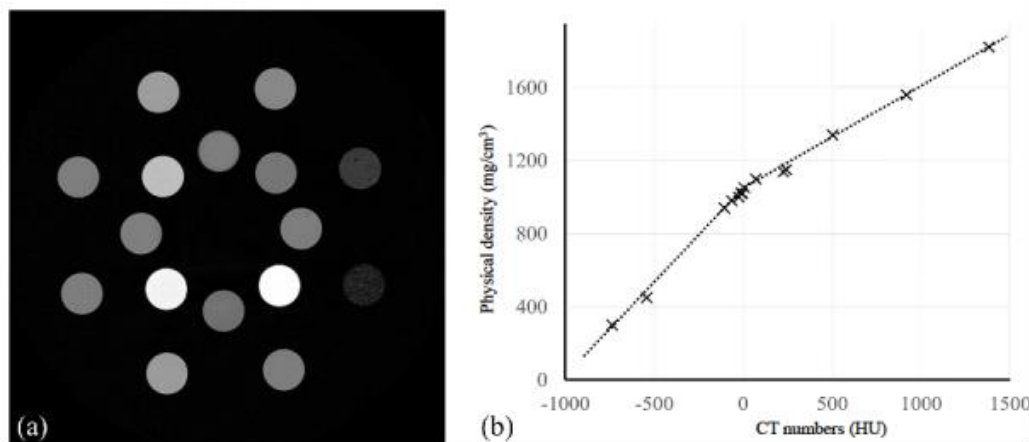
Figure 2.14: Conversion of CT HU numbers into BMD using a calibration phantom. (a) An axial image slice from an MDCT scan of a Gammex RMI 467 Tissue Characterization Phantom. The image shows the cross-sectional profile of sixteen cylinders with known physical density. (b) A typical conversion function. Each cross represents the computed average CT number for the corresponding cylinder and its known physical density.

segmented cylinder was eroded by five voxels to eliminate partial voluming effects and the average CT number over the eroded region was computed. A conversion function was computed using the correspondence between computed average CT numbers and the known physical density of individual cylinders; see Fig. 2.14(b). As shown in the figure, the conversion function has two segments, the lower segment was computed using the calibration data from the cylinders with their physical density greater or equal to that of pure water; the other segment of the calibration function was computed using the remaining cylinders. After converting an MDCT image into a BMD

image, it was interpolated at 150 μm isotropic voxels using a windowed sync inter-polation method.29 All subsequent image processing operations were performed on BMD images at 150 μm isotropic voxels.

VOI Selection.

Different VOI selection schemes were applied for different experiments depend-ing upon their purposes. VOI selection methods for different experiments are briefly outlined in the following.

VOI selection for the bone strength experiment: The twenty-two cadaveric an-kle specimens from SpecimenA were used for this experiment. The size and location of VOIs for image analysis of the cadaveric bone strength study were chosen as per the information recorded during specimen preparation for mechanical testing. First, the tibial bone region was filled using distance transform [16, 130] and connectivity analysis [128] and the bone axis was aligned with the coordinate z-axis [89, 88, 90]. After reorienting the bone image, a VOI cylinder of 8-mm diameter along the coordi-nate z-axis was generated and its proximal end was manually positioned at the center of the cortical rim using in-plane translation through a graphical user interface. The location of the distal end of the VOI cylinder in the slice direction and its length were determined as per the core location and length recorded during specimen preparation; the growth plate was visually located in the CT data of each specimen. Finally, the central 6-mm region from the cylinder was used as the VOI for the extensometer test; for the non-extensometer study, the length of the VOI was determined as per data collected during specimen preparation for the second mechanical test.

VOI selection for the repeat scan reproducibility experiment: The twenty-two cadaveric ankle specimens from SpecimenA were used for this experiment. The purpose of this experiment was to examine the reproducibility performance index as a function of VOI size to assess the localization scale yielding a reliable TB microarchitectural measure. For a given VOI size, ten spherical VOIs were randomly selected in the first MDCT scan of each cadaveric specimen (a total of 250 VOIs). Each VOI was randomly located within 30% peeled region covering 1.5 to 4.3 cm proximal sites of distal tibia, or equivalently, 4 to 12% of an average distal tibia. A post-registration algorithm was used to locate the matching VOIs in the second and third repeat scans. The range of VOI diameter covered in this experiment was 0.15 mm to 6.75 mm, i.e., 1 to 45 voxels.

VOI selection for the between-scanner human study: UHR MDCT scans of distal tibia of twenty human volunteers on two scanners were used for this study. The correlation between measures using images from two MDCT scanners was analyzed at a regional scale using smaller VOIs. Also, the correlation of summary measures from two scanners were analyzed using larger VOIs adjusting for variations among individual-specific tibial length and width values. For the correlation study of regional measures, fifty spherical VOIs each of diameter 4.65 mm, i.e., 31 voxels were randomly selected within 30% peeled region covering 4 to 12% proximal sites of an individual participants distal tibia. Thus, for a given TB microarchitectural measure, a total of 1000 observed data were used for analysis. These VOIs were first selected in the image from the old scanner, and a post-registration algorithm was used to locate the

matching VOIs in the image from the new scanner. For the correlation study of a global measure, regions covering 4 to 6% and 6 to 8% proximal sites of an individual participants distal tibia were used for VOIs. Inner VOIs were determined using 60% peel, while outer VOIs were determined in the region between 30% and 60% peels. Global VOIs were independently determined in the images from the two scanners.

Fuzzy Skeletonization.

The performance of the TB plate-width computation method [139, 34] is highly dependent on the quality of the surface skeleton [122] generated from the volumetric representation of a TB network acquired in vivo. Binary skeletonization [133] is always associated with binarization-related data loss adding skeletal inaccuracies such as disruption of trabecular rods, perforation of plates, and filling of small marrow holes. Fuzzy skeletonization reduces binarization-related data loss, which improves the preservation of trabecular network connectivity especially at regions containing relatively thin trabeculae. The fuzzy skeletonization algorithm [69] uses fuzzy distance transform to simulate a grassfire propagation of a fuzzy object, where the fire-front speed at a location depends on its object membership; here, the bone volume fraction. The fire propagation is interrupted and stopped at fuzzy quench points, which fail to pass fire-fronts to their neighbors. Although fuzzy quench points capture the medial axis or symmetry-structures, they create numerous spurious skeletal structures; and this phenomenon is further aggravated in fuzzy skeletonization. Spurious quench points are detected and only significant quench points are kept using a measure of *collision impact* [70] capturing the angle between colliding fire-fronts. Subsequently,

object points, excluding significant quench points, are sequentially removed in the increasing order of their FDT values while preserving object topology, which is accomplished using the characterization of 3-D simple points [132, 124]. It should be noted that, despite the filtering of quench points, a few spurious skeletal branches may still survive. A post-skeletal-pruning step [139, 4] is applied to prune noisy branches based on their global significance computed as the collision-impact-weighted branch length.

2.4.1.5 Other Quantitative Methods

Digital Topological Analysis.

Digital topological analysis or DTA [131] is a three-dimensional method that accurately determines the topological class (e.g., surfaces, curves, junctions) of each individual voxel in a digitized structure; see Figure 3. This method has been popularly applied for quantifying quality of TB architectural makeup. Before applying DTA, a fuzzy segmented TB volume image is skeletonized. A skeleton of a TB volume image is a network of one- and two-dimensional digital structures representing trabecular rods and plates, respectively. DTA involves inspecting local topological numbers, i.e., numbers of bone components, tunnel, and cavities in the $3{\times}3{\times}3$ excluded (i.e., the central voxel is excluded) neighborhood each bone voxel [131]. The algorithm use a three-step approach to achieve a unique topological classification at every bone voxel using lookup tables and topological analysis in the extended neighborhood solving for local topological ambiguities in digital manifolds and their junctions. These topo-

logical classes are then used to compute several topological parameters for trabecular bone networks. The specific parameter, namely erosion index (EI) was found to be highly sensitive in most studies using DTA, and this DTA parameter is used in our experiments. The EI is defined as the ratio of all topological parameters expected to increase during the erosion process (specifically, curve, curve-edge, surface-edge, profile-edge, and curve-curve-junction types) compared with those that are expected to decrease (surface and surface-surface junction types).

Structure Model Index.

The structure model index or SMI [65] is an indirect global estimation of the plate-rod characteristic of a three-dimensional structure. SMI is calculated by a differential analysis of a triangulated surface of a structure, which is defined using the surface area derivative with respect to the half-thickness or the radius assumed constant over the entire structure. This derivative is estimated by a simulated thickening of the structure by translating the triangulated surface by a small extent Δ_r in its outward normal direction and dividing the associated change of surface area with Δ_r. For an ideal plate and rod structure the SMI value is 0 and 3, respectively. For a structure with both plates and rods of equal thickness, the value is between 0 and 3, depending on the volume ratio of rods to plates.

2.4.2 Results

2.4.2.1 Reproducibility of quantitative measures on cadaveric subjects.

The reproducibility of each quantitative measure was summarized in Figure 4 as a function of VOI size. For a given VOI size, each measure was calculated over the randomly located VOIs for all three repeat scans. The ICC value was then computed and used as reproducibility index. It was observed that the ICC values increase with the enlargement of VOI size and gradually converge to a stable level. At the final stable stage (VOI diameter of around 4 mm), most measures, namely vBMD , tBMD, NAD, PW_{VTA}, PRR_{VTA}, PW_{TS}, PRR_{TS}, TB-Th, TB-Sp, reach the ICC value of 0.95. In contrast, structure model index converges to around 0.86 and erosion index oscillates between 0.80 and 0.90. We also observed that the ability of reaching convergence is different for each measure. The PW_{TS} and PRR_{TS} were found of ICC value of 0.8 at VOI diameter of 0.15 mm. And other measures reach this level and remain at VOI diameter of 2 mm, except SMI and EI. In addition, we ranked these measures by calculating the area under the curve, as an index of its reproducibility. The ranked order is as follows: $PW_{TS} > $ TB-Sp $ > PRR_{TS} > $ tBMD $ > $ TB-Th $ > PW_{VTA} > $ NAD $ > PRR_{VTA} > $ SMI $ > $ EI

2.4.2.2 Consistency of quantitative measures on μ-CT and MDCT.

Correlations of proposed quantitative measures between μ-CT and MDCT were computed using linear regression. For MDCT, mean value was used as the average of three repeat scan. The correlation coefficient (R^2) was plotted as a function
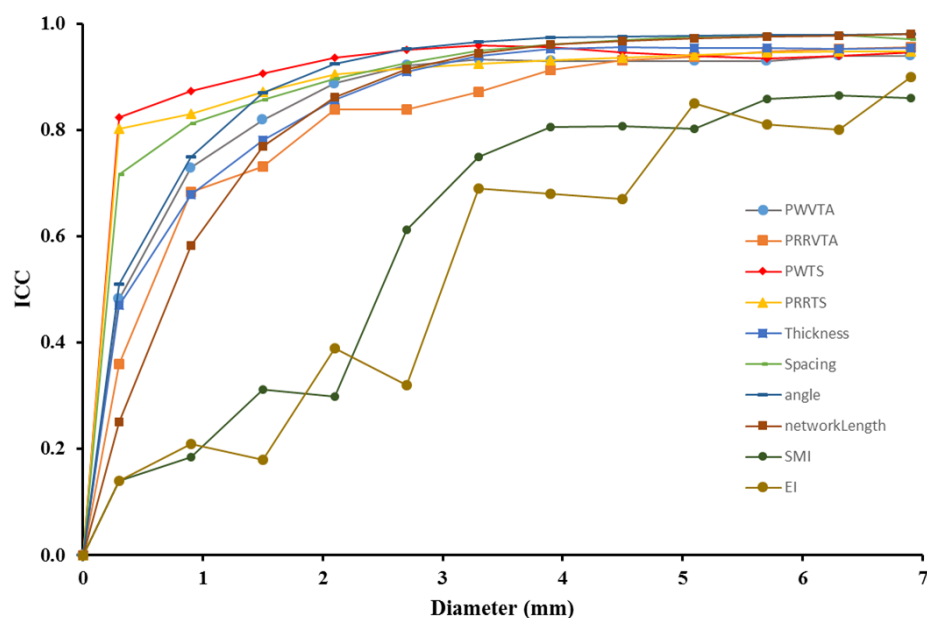
Figure 2.15: The reproducibility of all quantitative measures. Intra-class correlation coefficient (ICC) value is plotted as a function of VOI size. The range of VOI diameter is from 0.15 to 6.75 mm.

of VOI diameter size as shown in Fig. 2.16.

With the enlargement of VOI diameter size, correlations of quantitative measures were found increasing and then saturated. Although different measures saturate at different VOI diameter size, when the VOI is sufficient large, i.e., diameter is larger than 3.5 mm, all measures reach convergence. Such correlation remains even when the VOI diameter size grows. In addition, the slope of linear regression equation remains stable for each of the quantitative measure.

The network length measure was found with the highest correlation ($R^2 >$
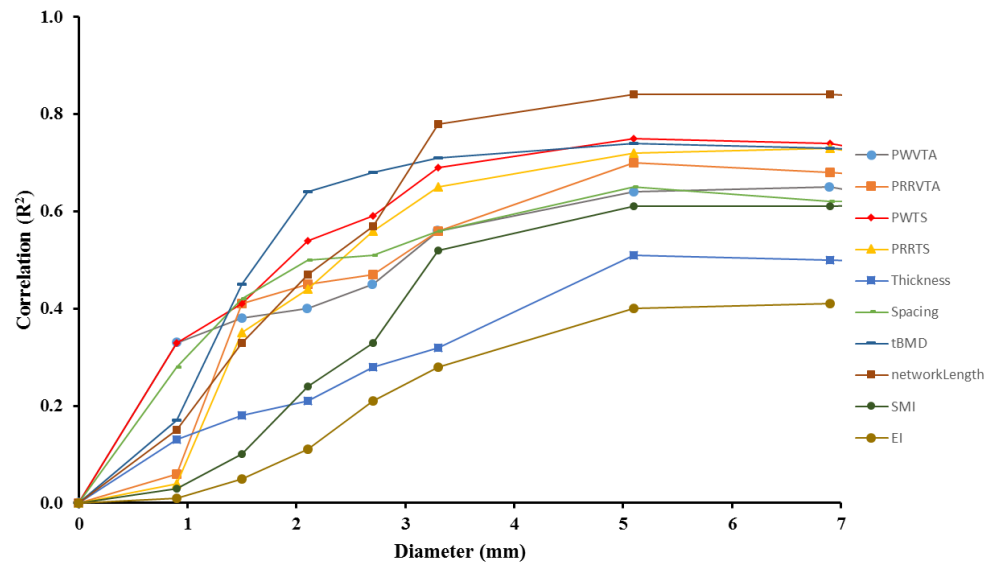
Figure 2.16: The correlation of quantitative measures between μ-CT and MDCT. Correlation coefficient (R^2) was computed using linear regression.

0.80) between μ-CT and MDCT. This observation reveals the ability of MDCT imaging to identify trabecular network compared with high-resolution μ-CT. It is noted that, on the contrary, the thickness measure was found with less correlation (R^2 is approximate 0.50). The reason is that although MDCT imaging is capable of identifying more than 80 percent trabecular structures, the strong partial volume effect adds fuzziness at TB boundaries and thus thickens the network. The plate-width measure, either computed by VTA or tensor scale method, has higher correlations between imaging modalities since naturally, the plate-width of trabecular was thicker than the thickness, and the partial volume effect was less influential. We can also observe that quantitative measures computed by tensor scale, including tBMD, PW_{TS} and PRR_{TS},

Table 2.4: Average slopes and intersects of linear regression lines of several measures when the diameter of ROI is largt than 5 mm.

	PW_{VTA}	PRR_{VTA}	PW_{TS}	PRR_{TS}	NAD
slope	1.22±0.03	2.84±0.02	1.93±0.08	3.41±0.16	0.018±0.001
intersect	233.6±33.4	-0.66±0.37	-119.3±42.2	-1.65±0.41	0.03±0.003

are better than measures computed by VTA, which indicates that the tensor scale method is more accurate in computing trabecular plate-width under limited imaging resolution.

2.4.2.3 Ability to predict bone strength.

The ability of proposed TB measures to predicted bone strength was summarized in Fig. 2.17. Linear regression was applied between each measure and the yield stress and the corresponding correlation coefficient (R^2) was computed. In the figure, each dot represents the mean value calculated as the average of values from three repeat scans of each subject.

The R^2 value of BMD was found 0.61, which is in accordance with DXA BMD meta-analysis that in general it accounts for 60 to 70% of the variability in bone strength. The plate-width measures computed by VTA and tensor scale, i.e., PW_{VTA}, PRR_{VTA}, were observed with the closest trends with that of yield stress, $R^2 = 0.81$ and $R^2 = 0.80$, respectively. Structure model index and erosion index were observed with relatively low correlation with yield stress, $R^2 = 0.62$ and $R^2 = 0.61$,

respectively. All listed measures have shown better or at least the same correlation with yield stress than BMD.

2.4.2.4 Continuity and consistency of quantitative measures between two scanners.

Trabecular bone measures were computed using MDCT images from FLASH and FORCE scanners over inner, outer regions and 50 randomly selected ROIs for each subject. For random ROIs, trimming algorithm was done so that any pairs of observation for FLASH and FORCE scanner for which at least one is above 90th percentile of distribution or below 10th percentile of distribution for data combined, these pairs were not used in analysis.

Complete data analysis results were summarized in multiple tables: table 2.5, table 2.6, table 2.7, table 2.8, table 2.9.

Lin's Concordance Correlation Coefficient (CCC), the Pearson Correlation Coefficient (PCC) were computed between FLASH scan measures and FORCE scan measures. CCC can be interpreted as the agreement between continuous measurements about a 45-degree line.

Overall, a very high correlation between FLASH measures and FORCE measures were observed for various measures over different ROIs. It confirms that trabecular bone measures can be continuously and consistently computed from different imaging conditions. Therefore keeping data consistent in the case of switching scanners in longitudinal studies would be possible.

Comparing results between inner and outer regions, it is observed that generally measures in the outer region have better correlation than measures in the inner region. The reasons is that trabecular network in the outer region (closer to cortical bone) are generally stronger than that in the inner region, which can be observed by computed mean values, for example PW_{TS}, BMD. In fact, various researches also show that trabecular bone in outer region consists of more plate-like structure [136]. Due to thin trabeculae, structure in the inner region is more sensitive to noise. This explains the difference of correlations between inner and outer regions. The results of random ROIs were observed of lower correlation because these ROIs are of smaller size than inner and outer regions, which represent more local information than global characteristics. The variety is reasonably higher.

Other observations are the ability of different bone micro-architectural measures. Compared with BMD, which is the DXA information, TB-Th, PW_{TS}, PW_{VTA} are more robust measures in different ROIs, while TB-Sp and NAD have larger variances, because they are more vulnerable to noise.

In total, combined measures over both inner and outer regions in 4-8% tibia length (shown in Fig. 2.18) have shown a promising consistency. Most measures were observed well predicted by the 45 degree line. We may draw the conclusion the micro-architectural measures are consistent computed from two scanners.

2.5 Conclusion

Osteoporostic imaging is critically important in identifying fracture risks of individuals. Reliably measuring trabecular bone micro-architecture could be of clinical significance. In vivo volumetric bone imaging modalities, including MRI and MDCT, have been investigated for quantitative assessment of bone microarchitecture at peripheral skeletal sites in this study. We have shown prominent improvements that overcome major deficits of MRI and MDCT related to limited spatial resolution and partial volume effect. My study establishes a complete micro-architectural measurements of trabecular bone quality and have shown the effectiveness and robustness which encourages future studies.
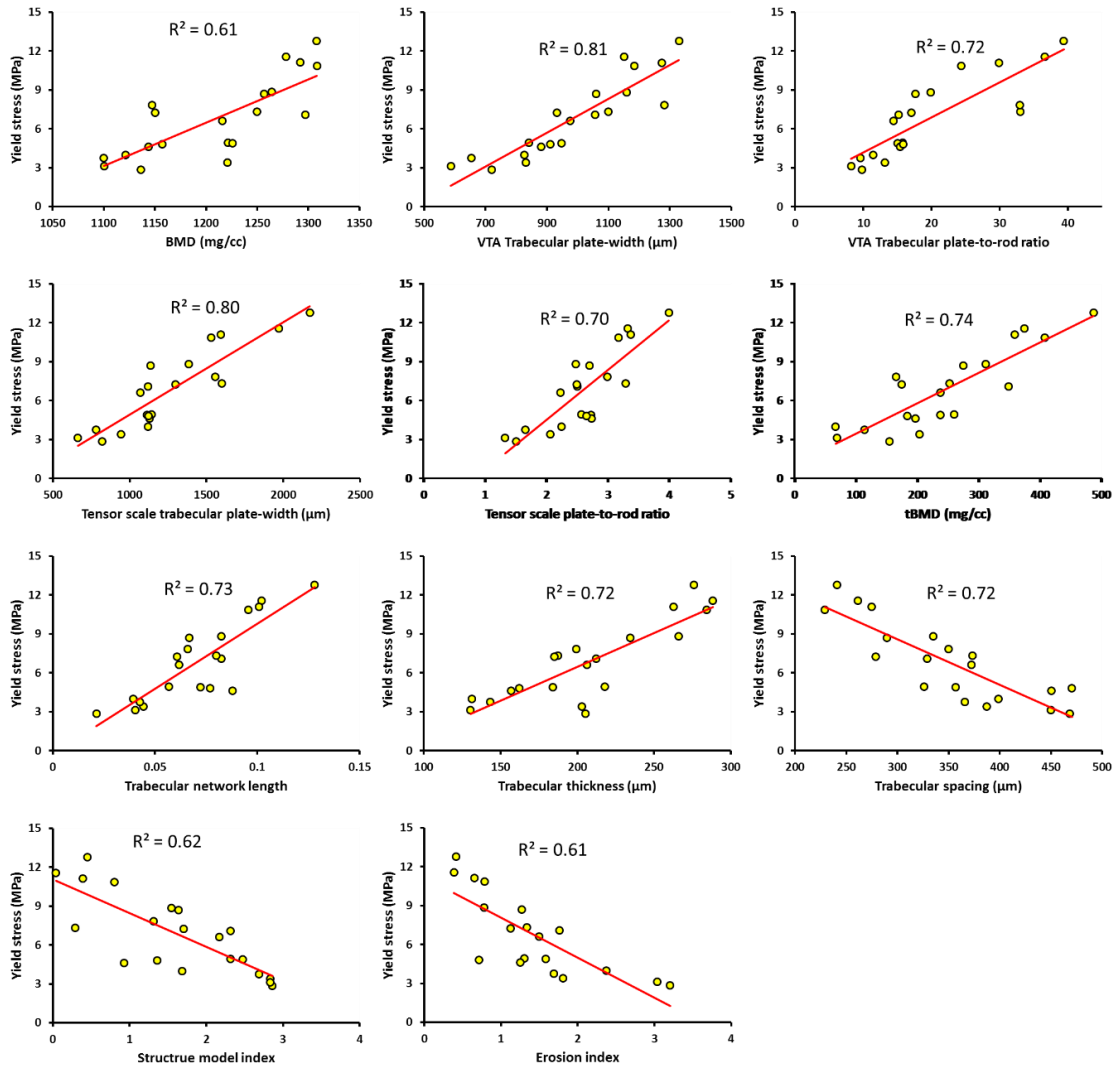
Figure 2.17: The ability of quantitative measures to predict bone strength. Linear regression is applied between each measure and the yield stress. The correlation coefficient (R^2) was computed and shown for each measure.
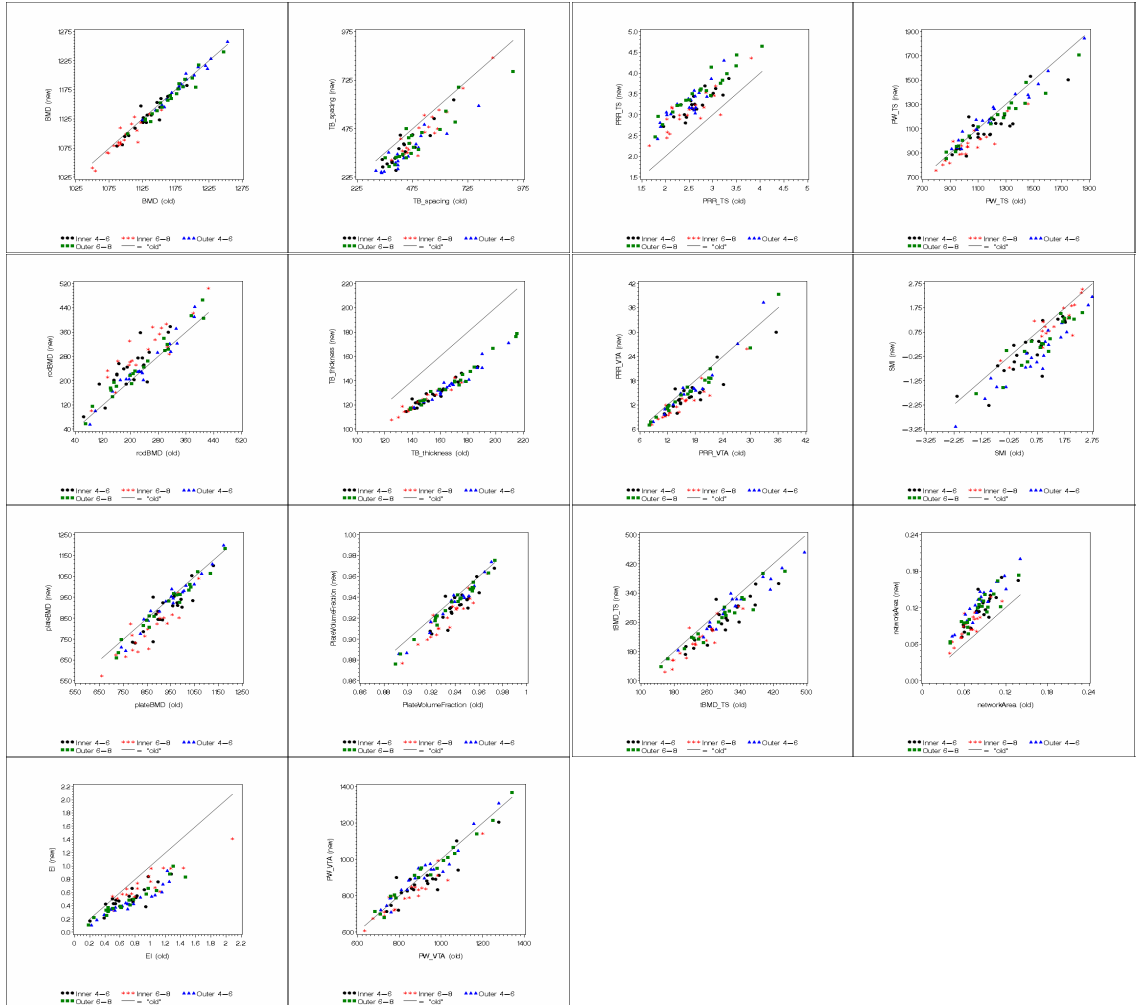
Figure 2.18: Correlations between FLASH (old) and FORCE (new) scanners using various measures over the region (inner and outer combined) of distal tibia in 4-8% length.

Table 2.5: Descriptive statistics, Lin's Concordance Correlation Coefficient (CCC), the Pearson Correlation Coefficient (PCC) for bone measures obtained from FLASH and FORCE scanners, for inner region in 4-6% tibia length.

Variable	FLASH	FORCE	CCC	PCC
BMD (mg/cc)	1132.4 (25.91)	1128.3 (28.06)	0.923 (0.822, 0.967)	0.933
PRR_{TS}	2.65 (0.34)	3.26 (0.30)	0.308 (0.144, 0.455)	0.863
PRR_{VTA}	17.43 (5.45)	14.89 (4.75)	0.803 (0.617, 0.904)	0.906
$PW_{TS}(\mu m)$	1178.7 (199.05)	1109.0 (171.00)	0.809 (0.608, 0.912)	0.87
$PW_{VTA}(\mu m)$	916.04 (129.42)	879.37 (113.61)	0.844 (0.668, 0.931)	0.885
PVF	0.94 (0.01)	0.93 (0.02)	0.714 (0.486, 0.851)	0.869
TB-Sp (μm)	435.06 (82.72)	370.34 (90.68)	0.715 (0.515, 0.842)	0.915
TB-Th (μm)	155.05 (13.77)	128.68 (9.94)	0.267 (0.127, 0.396)	0.957
NAD (cm^{-1})	0.09 (0.02)	0.12 (0.03)	0.427 (0.216, 0.600)	0.858
pBMD (mg/cc)	932.83 (84.29)	888.88 (96.58)	0.779 (0.570, 0.893)	0.873
rBMD (mg/cc)	199.53 (62.78)	239.41 (74.68)	0.712 (0.469, 0.855)	0.837
t-BMD_{TS} (mg/cc)	300.26 (59.87)	266.50 (56.84)	0.770 (0.572, 0.883)	0.895
SMI	0.39 (0.99)	-0.03 (1.03)	0.789 (0.578, 0.901)	0.854
EI	0.71 (0.26)	0.51 (0.18)	0.577 (0.321, 0.755)	0.846

Table 2.6: Descriptive statistics, Lin's Concordance Correlation Coefficient (CCC), the Pearson Correlation Coefficient (PCC) for bone measures obtained from FLASH and FORCE scanners, for outer region in 4-6% tibia length.

Variable	FLASH	FORCE	CCC	PCC
BMD (mg/cc)	1185.4 (30.83)	1184.1 (32.76)	0.983 (0.960, 0.993)	0.985
PRR_{TS}	2.45 (0.39)	3.25 (0.41)	0.290 (0.137, 0.430)	0.878
PRR_{VTA}	16.25 (5.89)	15.51 (6.68)	0.962 (0.911, 0.984)	0.975
$PW_{TS}(\mu m)$	1221.2 (252.94)	1224.1 (230.40)	0.976 (0.942, 0.990)	0.979
$PW_{VTA}(\mu m)$	912.75 (148.35)	918.20 (148.45)	0.967 (0.921, 0.987)	0.966
PVF	0.94 (0.02)	0.93 (0.02)	0.960 (0.910, 0.982)	0.984
TB-Sp (μm)	442.37 (109.61)	346.56 (91.17)	0.631 (0.424, 0.776)	0.929
TB-Th (μm)	167.41 (17.48)	136.89 (13.60)	0.325 (0.170, 0.464)	0.971
NAD (cm^{-1})	0.09 (0.02)	0.13 (0.03)	0.403 (0.222, 0.557)	0.947
pBMD (mg/cc)	946.89 (113.25)	935.84 (123.88)	0.974 (0.938, 0.989)	0.981
rBMD (mg/cc)	238.47 (85.35)	248.26 (95.07)	0.965 (0.917, 0.985)	0.975
t-BMD_{TS} (mg/cc)	319.79 (81.56)	302.08 (74.24)	0.947 (0.883, 0.977)	0.975
SMI	0.64 (1.24)	-0.22 (1.29)	0.780 (0.621, 0.877)	0.962
EI	0.74 (0.31)	0.46 (0.20)	0.535 (0.310, 0.704)	0.948

Table 2.7: Descriptive statistics, Lin's Concordance Correlation Coefficient (CCC), the Pearson Correlation Coefficient (PCC) for bone measures obtained from FLASH and FORCE scanners, for inner region in 6-8% tibia length.

Variable	FLASH	FORCE	CCC	PCC
BMD (mg/cc)	1097.9 (25.44)	1092.4 (28.07)	0.901 (0.777, 0.957)	0.921
PRR_{TS}	2.52 (0.51)	3.08 (0.47)	0.514 (0.291, 0.683)	0.855
PRR_{VTA}	15.00 (4.78)	12.43 (4.15)	0.804 (0.637, 0.898)	0.943
$PW_{TS}(\mu m)$	1042.4 (159.87)	967.34 (134.99)	0.798 (0.611, 0.901)	0.91
$PW_{VTA}(\mu m)$	852.99 (133.86)	812.36 (118.00)	0.896 (0.778, 0.953)	0.947
PVF	0.93 (0.02)	0.92 (0.02)	0.758 (0.578, 0.868)	0.942
TB-Sp (μm)	529.24 (107.99)	468.00 (130.50)	0.821 (0.658, 0.911)	0.942
TB-Th (μm)	146.76 (14.40)	122.85 (9.55)	0.307 (0.150, 0.448)	0.969
NAD (cm^{-1})	0.07 (0.02)	0.09 (0.02)	0.537 (0.308, 0.708)	0.872
pBMD (mg/cc)	859.64 (99.62)	792.81 (109.79)	0.753 (0.555, 0.870)	0.907
rBMD (mg/cc)	238.31 (85.59)	299.55 (92.13)	0.731 (0.529, 0.855)	0.904
t-BMD_{TS} (mg/cc)	240.19 (51.21)	211.31 (51.13)	0.797 (0.621, 0.896)	0.921
SMI	1.37 (0.85)	1.12 (0.89)	0.856 (0.689, 0.937)	0.885
EI	0.91 (0.40)	0.71 (0.27)	0.726 (0.497, 0.860)	0.924

Table 2.8: Descriptive statistics, Lin's Concordance Correlation Coefficient (CCC), the Pearson Correlation Coefficient (PCC) for bone measures obtained from FLASH and FORCE scanners, for outer region in 6-8% tibia length.

Variable	FLASH	FORCE	CCC	PCC
BMD (mg/cc)	1168.2 (33.49)	1162.8 (34.79)	0.965 (0.919, 0.985)	0.976
PRR_{TS}	2.74 (0.60)	3.56 (0.55)	0.476 (0.290, 0.627)	0.957
PRR_{VTA}	17.03 (7.01)	15.85 (7.23)	0.966 (0.923, 0.986)	0.979
$PW_{TS}(\mu m)$	1210.4 (254.88)	1171.1 (215.08)	0.954 (0.893, 0.981)	0.98
$PW_{VTA}(\mu m)$	944.46 (181.33)	944.46 (174.33)	0.985 (0.963, 0.994)	0.985
PVF	0.94 (0.02)	0.93 (0.02)	0.967 (0.929, 0.985)	0.992
TB-Sp (μm)	505.45 (136.28)	425.44 (129.22)	0.785 (0.607, 0.888)	0.926
TB-Th (μm)	168.90 (22.72)	139.06 (18.06)	0.467 (0.284, 0.617)	0.985
NAD (cm^{-1})	0.08 (0.02)	0.11 (0.03)	0.503 (0.296, 0.666)	0.907
pBMD (mg/cc)	937.38 (126.21)	915.04 (131.70)	0.970 (0.932, 0.987)	0.985
rBMD (mg/cc)	230.78 (99.38)	247.75 (104.50)	0.969 (0.928, 0.986)	0.982
t-BMD$_{TS}$ (mg/cc)	286.60 (75.59)	264.40 (69.09)	0.924 (0.839, 0.965)	0.97
SMI	1.08 (1.14)	0.51 (1.16)	0.848 (0.711, 0.923)	0.953
EI	0.71 (0.36)	0.47 (0.23)	0.668 (0.446, 0.812)	0.965

Table 2.9: Descriptive statistics, Lin's Concordance Correlation Coefficient (CCC), the Pearson Correlation Coefficient (PCC) for bone measures obtained from FLASH and FORCE scanners, for randomly picked ROIs in 4-8% tibia length.

Variable	FLASH	FORCE	PCC
BMD (mg/cc)	1089.6 (44.72)	1087.7 (44.50)	0.951
PRR_{TS}	2.33 (0.76)	2.70 (0.79)	0.79
PRR_{VTA}	12.01 (5.47)	11.00 (5.20)	0.869
$PW_{TS}(\mu m)$	908.74 (228.83)	902.78 (216.75)	0.89
$PW_{VTA}(\mu m)$	741.20 (191.32)	741.14 (190.20)	0.883
PVF	0.90 (0.05)	0.90 (0.05)	0.879
TB-Sp (μm)	606.18 (227.05)	566.22 (226.69)	0.9
TB-Th (μm)	136.85 (21.21)	120.58 (17.00)	0.913
NAD (cm^{-1})	0.06 (0.03)	0.07 (0.04)	0.912
pBMD (mg/cc)	739.99 (214.49)	704.09 (222.21)	0.88
rBMD (mg/cc)	347.03 (179.58)	379.68 (186.48)	0.842
$t\text{-BMD}_{TS}$ (mg/cc)	198.78 (85.67)	183.99 (80.50)	0.918
SMI	0.61 (1.86)	0.65 (1.84)	0.909
EI	1.64 (1.54)	1.40 (1.44)	0.769

CHAPTER 3
COMPUTATIONAL AND MECHANICAL ANALYSIS OF
TRABECULAR BONE

3.1 Image Segmentation of Trabecular Bone

Osteoporosis is associated with an increased risk of fractures. Its incidence increases progressively with age [119]. In the United States, about 8 million women and 2 million men have osteoporosis with medical costs estimated at $22 billion in 2008 [13]. Clinically, osteoporosis is defined by low bone mineral density (BMD). However, BMD only accounts for approximately 60% to 70% of the variability in bone strength [177]. The remaining variability is due to the cumulative and synergistic effects of various factors, including trabecular bone (TB) microstructure [81, 118]. Thus, reliably measuring TB microstructure could be of clinical significance, particularly as trabecular bone may be more susceptible to hormonal, pharmacological, and toxic effects.

TB is a complex interconnected network of individual trabecular microstructures. The conventional tool for assessing TB structure is two-dimensional (2D) cross-sectional histomorphometry from bone biopsies [112]. Recent advancements in volumetric bone imaging, such as magnetic resonance (MR) [177, 108, 29], high resolution peripheral quantitative computed tomography (HR-pQCT) [17, 24], and clinical computed tomography (CT) [95, 139, 136], allow characterization of bone micro-architecture at peripheral sites without the need for biopsy.

Various methods related to digital topology and geometry [126], scale [121, 65],

and computational mechanics [116, 105, 79] have been reported in literature [91]. Saha *et al.* developed a skeletonization [122] based method of digital topological analysis [123, 124, 133, 125] for regional plate-rod characterization of individual trabeculae. This basic method has been further modified and applied by other research groups [156, 157, 97, 174] for assessment bone strength and fracture-risk. Segmentation of TB from the marrow space is essential for quantitative analysis of morphometric and biomechanical properties of TB microstructure. Irrespective of the methods used for quantitative *in vivo* assessment of TB microstructure, the fidelity of measures largely depends on the accuracy of TB segmentation. Although, current *in vivo* imaging technologies allow characterization of TB microstructure, accurate segmentation of TB network in such images remains challenging due to significant partial voluming effects, noise, and space varying background intensity for marrow voxels.

Clinical CT imaging is rapidly emerging as a frontrunner for imaging bone microstructure at peripheral sites due to its high availability in clinical environments, high spatial resolution, ultra-high speed scanning, ultra-low dose radiation, and large scan-length. A global threshold scheme [111, 127] is often used for TB segmentation in CT imaging. However, due to partial voluming, scattering and other CT imaging artifacts, trabecular bone regions with dense and thick trabeculae require higher values of the threshold to preserve marrow holes, while regions with sparse and thin trabeculae demands lower values of the threshold to preserve local connectivity of trabecular network. Therefore, locally adaptive thresholding is needed for accurate

and robust segmentation of TB that preserves both marrow holes as well as trabecular network connectivity. Waarsing *et al.* applied local thresholding on high resolution micro-CT imaging [170]. Burghardt *et al.* developed a locally adaptive thresholding approach using a hysteresis-based algorithm on gradient map, and applied the method on high resolution peripheral quantitative CT (HRpQCT) images [22]. In addition to threshold based methods, Scherf and Tilgner proposed the Ray Casting Algorithm, which utilizes local maximum, to segment fossil and cancellous bone in micro-CT images [142]. Tassani *et al.* applied a modified Chan-Vese method to segment TB on micro-CT images [163].

First, we introduce a space-variant hysteresis approach to preserve connectivity of trabecular structure, and a high quality mesh generator for accurate FEM analysis to overcome difficulties that limit the application of MDCT for FEM on TB network. The space-variant hysteresis method works well in preserving connections of trabecular network under in vivo MDCT imaging and is demonstrated useful for FEM. Nevertheless, it suffers from the problem that the selection of critical thresholds is manual and thus limits the application on other imaging modalities. To overcome the problem, we present a new method for TB segmentation from *in vivo* clinical CT imaging of distal tibia by computing spatial variation in the background marrow intensity and the bone-marrow contrast. First, it enhances local TB separability using a new anisotropic diffusion algorithm that uses Hessian matrix to encourage along-structure smoothing, while restricting cross-structure diffusion, thus, arresting edge-blurring. Subsequently, the method determines the spatial variation in the

background marrow intensity and the bone-marrow contrast using a new multi-scale morphological algorithm. Essentially, the algorithm is designed to determine local intensity values for TB structures resembling mountain-ridges as well as for marrow regions forming valleys running quasi-parallel to TB ridges.

3.1.1 Space-variant Hysteresis

TB is a connected network, and preservation of its connectivity is essential for effective FEM analysis in acquired images. At limited spatial resolution and signal-to-noise ratio, available at *in vivo* imaging, preservation of TB network as well as marrow pores is highly threshold sensitive [127]. Trabeculae near a tibial axis are generally thinner than those closer the cortical bone. Also, marrow spacing of TB network near cortical bone is smaller as compared to that near the tibial axis. See Fig. 3.1 for illustration. Therefore, a larger threshold is needed near cortical bone to preserve marrow pores (Fig. 3.1b), while a lower threshold is needed near the tibial axis to preserve trabecular connectivity(Fig. 3.1c).

As demonstrated in Fig. 3.1, single threshold fails to preserve the connectivity of trabeculae near the tibial axis, and the marrow pores near cortical bone. Therefore, a space-variant thresholding strategy is adopted to compensate for the difference in trabecular patterns in different regions. In addition, at a given region a hysteresis approach is applied instead of a hard threshold to take advantage of contextual infor-mation. Following the spirit of the hysteresis algorithm [26], a conservative threshold value is used to determine confident TB voxels, while a lenient threshold is used to
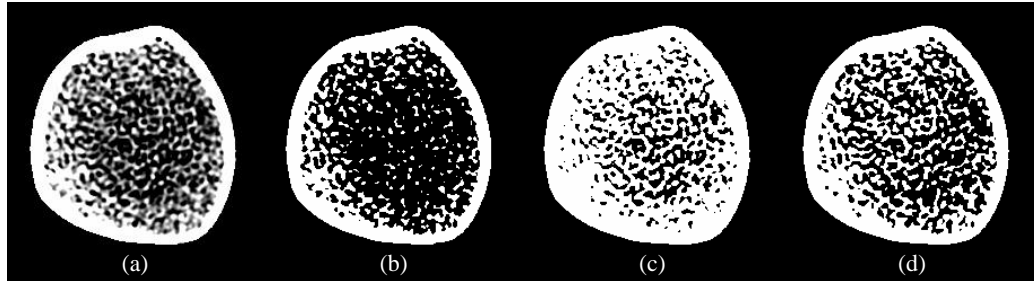
Figure 3.1: A matching slice of trabecular bone at distal tibia. (a) Fuzzy image, intensities are shown in the range [1000, 1300]. Binary image after applying (b) a high threshold to preserve marrow pores near cortical bone, and (c) a low threshold to preserve trabecular connectivity near tibial axis. (d) Binary image after space-variant hysteresis.

locate less confident TB voxels which are confirmed by the presence of confident TB voxels in their neighborhood. The method of determining the values of conservative and lenient thresholds for this application is described in the following.

The space-variant threshold parameters are defined as functions of distance from the outer boundary B_C of the segmented cortical bone region [89]. Let $f(p)$ denote the MDCT image intensity at a voxel p, and let $DT(p)$ be its distance value from the B_C. Also, let T denote the entire tibial region enclosed by B_C and let $d_{\max}$ be the maximum value of $DT(\cdot)$ within T. To determine the optimum values for conservative and lenient thresholds at different regions, inputs from multiple expert users are used. The tibial region T was divided into 3 sub-regions — 0 to 30% peel (R_{outer}), 30% to 60% peel (R_{interm}), and 60% peel (R_{inner}) sub-regions. An $x\%$ peel region on an axial slice is the set of all voxels with $DT(p) > x\%$ of $d_{\max}$. For each
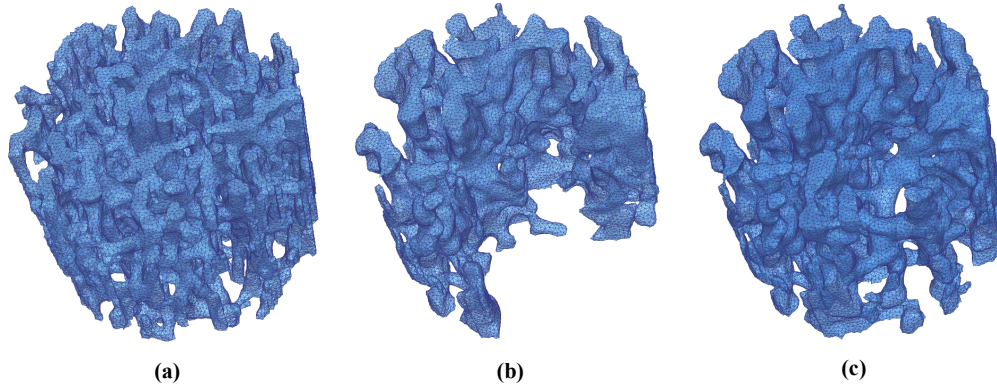
Figure 3.2: Mesh models of one cadaveric subject using (a) a μ-CT image, (b) an MDCT image without image processing, and (c) an MDCT image with space-variant hysteresis. ROI size is 8mm $\times$ 8mm $\times$ 6mm.

region, an expert user was asked to set two threshold values as follows — (1) conservative threshold (t_{con}): a threshold not including a noisy voxel from the marrow region and (2) lenient threshold (t_{lin}): a threshold preserving all TB connectivity. These threshold values were independently determined by three expert users on MDCT images of fourteen cadaveric tibia specimens. Observed mean $\pm$ std values for (t_{con},t_{lin}) over R_{outer}, R_{interm}, and R_{inner} are (1314$\pm$18, 1213$\pm$26), (1249$\pm$21, 1177$\pm$19), and (1177$\pm$26, 1125$\pm$23), respectively.

A space-variant thresholding scheme is defined using a two-step linear function, where the expert-guided average threshold values from R_{outer}, R_{interm}, and R_{inner} are assigned at 15%, 45%, and 80% peel locations. Finally, the space-variant hysteresis is defined as follows; the 26-neighborhood $N(p)$ [139] was used for our experiments.

Mesh representations of the central region of trabecular bone at distal tibia

are shown in Fig. 3.2. Meshes are generated from segmented results using the space-variant hysteresis method and a constant thresholding. The mesh generator will be described in Sec. 3.2. Figure 3.2(a) represent the same trabecular area from corresponding μ-CT image and was considered as ground truth. It is apparent that the mesh generated from space-variant hysteresis (c) is fully connected while the mesh of a constant threshold (b) fails to preserve the completeness of the network, similar to the result shown in Fig. 3.1. It emphasizes that due to the limited resolution and strong partial volume effect of *in vivo* MDCT imaging, an appropriate segmentation algorithm has a great influence to preserve the completeness and the topology of entire trabecular network.

For FEM analysis, preserving the completeness of the trabecular network is fundamental. Traditional thresholding scheme may fail to correctly identify thin connecting trabecular bone, resulting missing of parts of the structure. Therefore, I developed the space-variant hysteresis method to maximumly preserve the completeness of structure. This method has been demonstrated successful in segmentation of *in vivo* MDCT images and application in FEM [32]. However, the space-variant hysteresis method requires experts to decide critical parameters, i.e., the thresholds of $(t_{\text{con}}, t_{\text{lin}})$ over R_{outer}, R_{interm}, and R_{inner}. The method is therefore less adaptive to other imaging modalities. Further, if the imaging conditions change, those critical parameters have to be redetermined. The lack of automation is the biggest drawback. To overcome this problem, I developed a new segmentation algorithm that is fully automatic and adaptive to different imaging modalities. The method is described in

the following section.

Algorithm 3.1 Space-variant hysteresis

---

1. Segment cortical bone and compute $DT(\cdot)$
2. $\forall p \in T$, if $f(p) > t_{con}(p)$, add p in U_{con}
3. **While** Q is not empty
4.   pop p from Q
5. $\forall q \in N(p) - U_{con}$, if $f(q) > t_{lin}(q)$
6.   add q in U_{con}; add q in Q
7. **EndWhile**

3.1.2   Multi-scale Morphological Reconstruction

3.1.2.1   Anisotropic Diffusion

Anisotropic diffusion, first proposed by Perona and Malik [114], can be described using a divergence operator on an intensity flow vector field **F** as follows:

$$\frac{\partial I}{\partial t} = div\mathbf{F}, \tag{3.1}$$

where I is the image at time point t. The intensity flow vector, constructed as $\mathbf{F} = G(|\nabla I|) \cdot \nabla I$, controls the diffusion process that facilitates within-region diffusion, while arresting cross-structure blurring. Here, ∇I represents the intensity gradient, and the diffusion-conductance function G is a monotonocally decreasing nonlinear function that leads to generous diffusion within a homogeneous region, while a constricted diffusion across boundaries. Following the recommendation by

Perona and Malik, we use

$$G(|\nabla I|) = exp(-\frac{|\nabla I|^2}{\mu^2}).$$ (3.2)

The discrete formulation of the diffusion flow process is expressed as

$$I_{t+1}(p) = I_t(p) + \frac{k}{|N_8(p)| + 1} \sum_{q \in N_8(p)} G(|\nabla I_{p,q}|)\nabla I_{p,q},$$ (3.3)

where $t \geq 0$ is the iteration number; $I_0 = I$; N_8 is the 8-neighborhood; $\nabla I_{p,q}$ is the intensity gradient between two voxels p, q; and $k \in [0, 1]$ is a constant determining the overall speed of diffusion. In the above equation, the parameter μ serves as the fulcrum in the entire diffusion process selecting between within- and across-region image gradients. Thus, the choice of μ is critical, and a robust locally adaptive strategy is needed to improve the performance of anisotropic diffusion [166]. Inspired by Frangi's vesselness enhancement using Hessian matrix [54], we develop a locally adaptive strategy using the eigen values and eigen vectors of Hessian matrix that will facilitate diffusion along the structure, while constricting diffusion across an edge. The formulation of our locally adaptive diffusion process using Hessian matrix is described in the following.

Let $H(p)$ denote the Hessian at a voxel p; let $\lambda_1(p)$ and $\lambda_2(p)$ be the two eigenvalues of $H(p)$ and $\mathbf{i}_1(p)$ $\mathbf{i}_2(p)$ be corresponding eigenvectors. Let us assume that $|\lambda_1(p)| \leq |\lambda_2(p)|$. In general, when both $|\lambda_1(p)|$ and $|\lambda_2(p)|$ are small, the voxel p belongs to a homogeneous region; in this case, a generous diffusion should be allowed in all directions. When both $|\lambda_1(p)|$ and $|\lambda_2(p)|$ are large, p is an end- or a sharp corner-point, and the diffusion should be restricted in all directions. When $|\lambda_1(p)|$ is
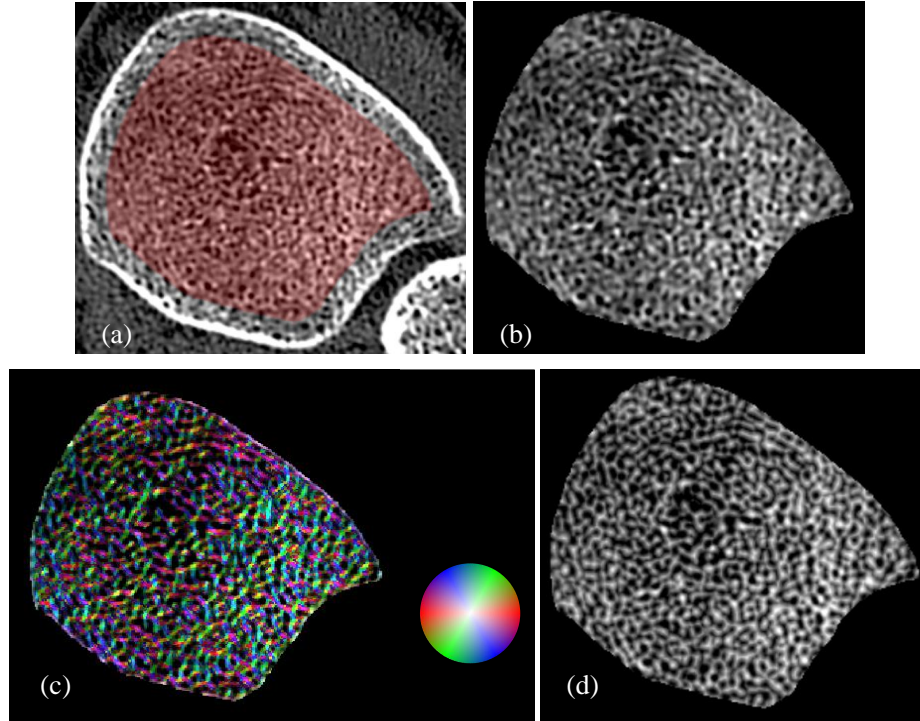
Figure 3.3: Results of Hessian matrix-guided anisotropic diffusion. (a) An axial view of an original BMD image and the region of interest (ROI). (b) BMD image within the ROI. (c) Color coded illustration of local tensor. Here, hue is the primary direction; saturation is the eccentricity of the tensor; and intensity is the BMD value. The color disk is shown. (d) Diffusion enhanced BMD image.

small but $|\lambda_2(p)|$ is large, p lies on an edge and a generous diffusion can be allowed along $\mathbf{i}_1(p)$, the eigenvector associated to the smaller eigenvalue, representing the direction along the structure, while the diffusion along $\mathbf{i}_2(p)$ representing the direction across the edge should be prohibited.

Here, we describe the computation of the parameter $\mu_{p,q}$ for the diffusion flow from a voxel p to its neighbor q. Let $\mathbf{i}_{p,q}$ denote the unit vector from p to q. The

second-order gradient magnitude $L_{p,q}$ from p to q is derived by projecting the Hessian matrix $H(p)$ along $\mathbf{i}_{p,q}$ as follows:

$$L_{p,q} = |\mathbf{i}_{p,q}^{\mathrm{T}} H(p) \, \mathbf{i}_{p,q}|. \tag{3.4}$$

To constrain diffusion in high-gradient regions, we use the the l_1 norm of the Hessian matrix as follows:

$$S_p = |\lambda_1(p)| + |\lambda_2(p)|. \tag{3.5}$$

Thus, the local diffusion control parameter $\mu_{p,q}$ should account for both directional gradient component $L_{p,q}$ as well as local isotropic gradient component S_p. The parameter $\mu_{p,q}$ is formulated as follows:

$$\mu_{p,q}^2 = \nabla_{\mathrm{avg}} \exp\left(-\frac{\mathrm{L_{p,q}} + \mathrm{S_p}}{2\lambda_{\mathrm{avg}}}\right), \tag{3.6}$$

where ∇_{avg} is the average gradient magnitude, and λ_{avg} is the average of $|\lambda_1|$ and $|\lambda_2|$ within the trabecular bone regions. Results of the new Hessian matrix-guided anisotropic diffusion is presented in Fig. 3.3. As it visually appears, the new diffusion algorithm has increased the contrast and local separability between trabecular bone microstructures and the marrow spacing. It is encouraging to note that, in bright regions containing thicker trabeculae, the algorithm enhances trabecular separation and preserves small marrow holes. At the same time, in darker regions containing thinner and sparse trabeculae, the algorithm preserves the trabecular structure. Therefore, it may be claimed that the algorithm improves local separability of trabecular structure.

3.1.2.2 Grayscale Morphological Reconstruction

The new TB segmentation algorithm models TB microstructures in a CT image as bright structures resembling ridges accompanied with quasi-parallel and relatively darker marrow regions resembling valleys. Our algorithm aims to determine spatial variation of intensity values for marrow valleys and TB ridges. Grayscale morphological algorithms [146, 147] are used as the underlying tool to determine local valley and ridge intensity profiles. A multi-scale strategy is incorporated to approximate the valleys and ridges, which are recognized over a large range of scales of morphological operations reducing the subjectivity of selecting a specific scale [183]. Let V and R denote the smooth intensity maps of marrow valleys and TB ridges, respectively, computed using multi-scale morphological algorithms. The segmentation of a TB network can be obtained using a space-varying thresholding scheme that accounts for spatial variation of both the valley intensity V and the trabeculae-marrow contrast $R-V$. The computation of V and R together with the space-varying thresholding algorithms are described in the following.

Let E_s denote a binary structuring element (SE) at a given scale s; the intensity map of the valley V_s is obtained after removing the trabecular structures using morphological opening as follows,

$$V_s^1 = I \circ E_s = (I \ominus E_s) \oplus E_s, \tag{3.7}$$

where $\circ, \ominus, \oplus$ denote the morphological opening, erosion, dilation operators, respectively. The morphological opening algorithm is repeated for a range of scales of SE. At a relatively smaller scale, the opening algorithm captures small variations in the
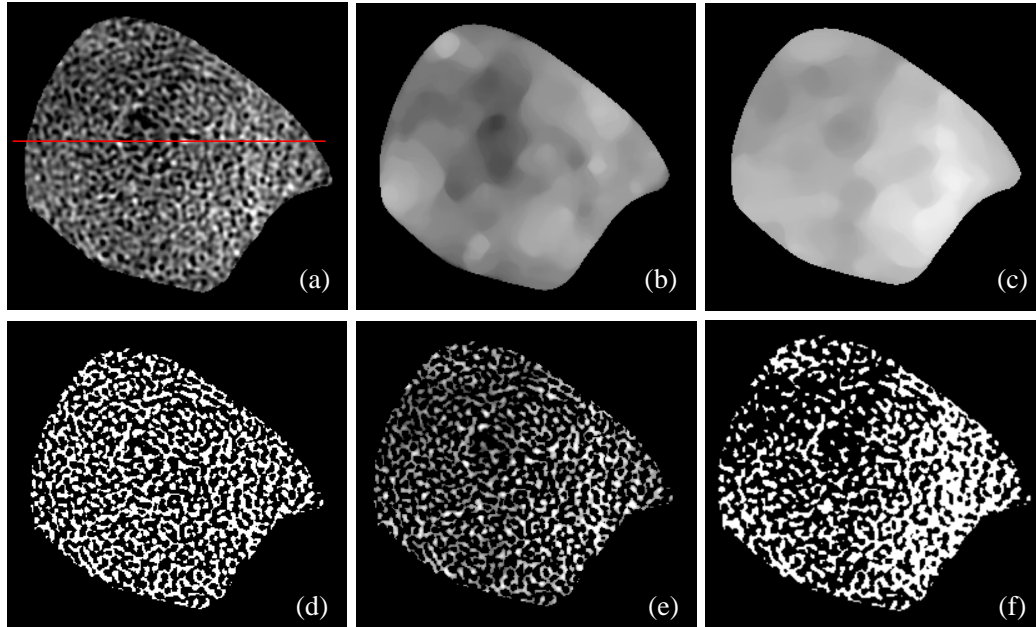
Figure 3.4: Illustration of TB segmentation using multi-scale morphological algorithms. (a) Original BMD image. (b) Regional intensity distribution of marrow valleys. (c) Same as (b) but for TB ridges. (d) Binary segmentation mask for TB microstructures. (e) BMD image on the TB mask of (d). (f) Segmented TB mask using manual global thresholding on the BMD image of (a).

background intensity, but, suffers the risk of being influenced by thicker trabeculae. At a larger scale, relatively small scale variations in the background intensity are ignored. To overcome these challenges and to reduce subjectivity errors of selecting a specific morphological scale, we used averaged intensity map over a large range of scales. The regional valley intensity V for marrow using the multi-scale strategy is given by

$$V = \sum_s w_s V_s, \tag{3.8}$$
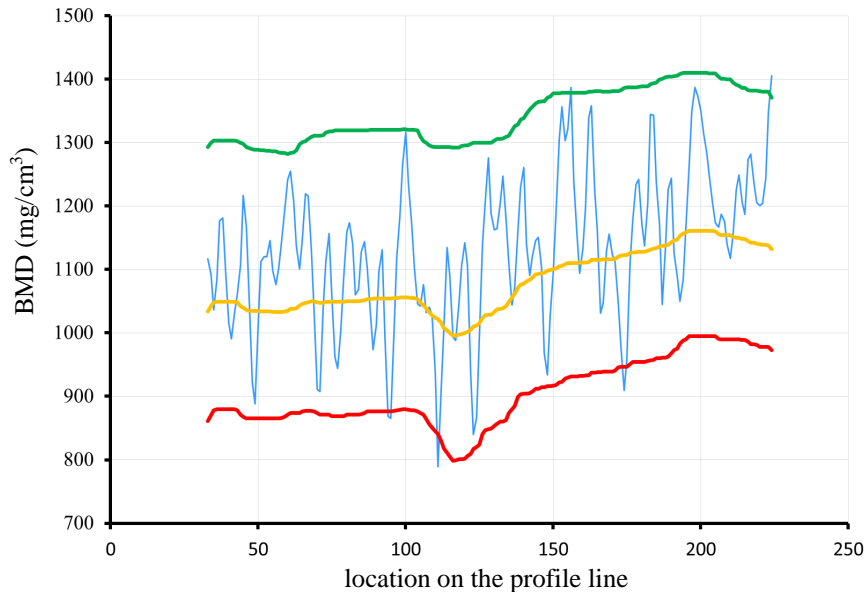
Figure 3.5: Illustration of marrow valley, TB ridge, and threshold detection on the intensity profile of the straight line shown in Fig. 3.4(a). The intensity profile is shown in blue, while the valley, ridge, and threshold profiles are shown in red, green, and gold colors, respectively.

where w_ss are equal weights such that $\sum_s w_s = 1$. Here, circular SEs with diameters $\{9, 11, \cdots, 21\}$ voxels are used; uniform weights are used for all scales.

The intensity map of the TB ridge R_s at a given scale s is computed using a morphological closing operation as follows:

$$R_s^1 = I \bullet E_s = (I \oplus E_s) \ominus E_s. \tag{3.9}$$

The regional TB ridge intensity R using the multi-scale strategy is given by

$$R = \sum_s w_s R_s. \tag{3.10}$$
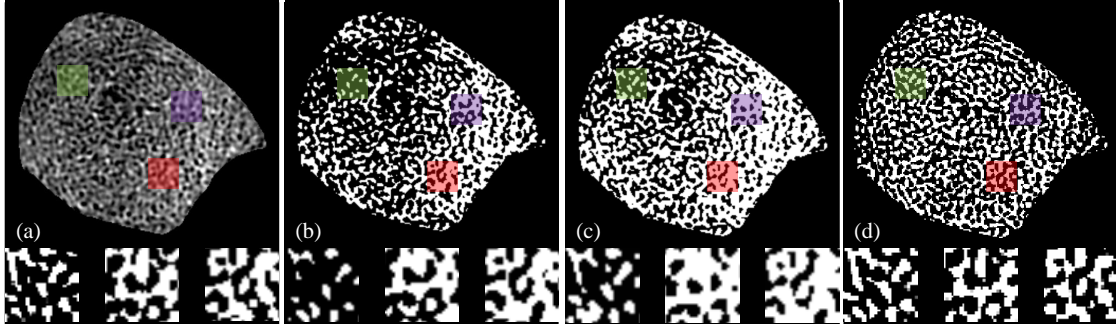
Figure 3.6: Comparison of regional TB segmentation using different methods. (a) Original BMD image and three random ROIs. (b, c, d) Segmentation results using global thresholding, Otsu's method, and our method, respectively. The enlarged display of each region is presented.

Finally, the binary segmentation of TB region is obtained by using a space varying thresholding map T that accounts both regional marrow intensity as well as bone-marrow contrast as defined in the following.

$$T = (1 - \alpha)V + \alpha R. \tag{3.11}$$

The value of α was empirically determined as 0.4, and used for all experiments presented in this paper; See Fig. 3.5. Results of computing spatial distribution of marrow valley and TB ridge intensity values are presented in Fig. 3.4. Detection of low-intensity TB microstructures while preserving high-intensity marrow holes is visually apparent in (d) as compared to the results of global manual thresholding in (f).

3.1.2.3 Segmentation Accuracy

The performance of the new TB segmentation method was evaluated in terms of sensitivity, specificity, accuracy and Jacaard Index by comparing with the results of regional manual thresholding. To study the implication of the new TB segmentation method on the TB thickness measure, we computed the measures from TB segmentations using the new and other methods and examined their abilities of predicting actual bone strength. These experiments and results are described in the following.

To quantitatively examine the sensitivity, specificity, accuracy and Jaccard Index, twenty *in vivo* CT images of distal tibia of healthy volunteers (age: 19 to 21 years; 10 males, 10 females) were used. Images were acquired at 120 kV, 200 effective mAs, 1 s rotation speed, pitch factor: 1.0, and reconstructed at 0.2 mm isotropic voxel. CT HU numbers were converted to BMD using a Gammex calibration phantom. For each image, twenty small region of interests (ROIs) ($30\times30\times3$ voxels) were randomly selected from the 30% peel ROI at 8% proximal site of the distal tibia covering 8% of the tibial length (see Fig. 3.3). Thus, we generated a total of 400 small ROIs for the accuracy experiment. As illustrated in Fig. 3.6, segmentation results on one slice of the TB image and three small ROIs are shown for each segmenation method.

Three mutually blinded readers independently selected the threshold value for TB segmentation in each small ROI, and the true TB segmentation for each ROI was determined using the average threshold value from three readers. For each method, true positive (TP), false negative (FN), true negative (TN) and false positive (FP) were computed. Sensitivity=TP/(TP+FN), specificity=TN/(TN+FP),

Table 3.1: Accuracy results of different methods on twenty *in vivo* CT images.

	Sensitivity	Specificity	Accuracy	Jaccard Index
Global threshold	0.94 ± 0.05	0.75 ± 0.14	0.81 ± 0.10	0.70 ± 0.12
Otsu's method globally	0.94 ± 0.13	0.70 ± 0.25	0.80 ± 0.14	0.69 ± 0.17
Otsu's method locally	0.95 ± 0.09	0.79 ± 0.20	0.85 ± 0.11	0.75 ± 0.17
Space-variant hysteresis	0.93 ± 0.15	0.85 ± 0.14	0.89 ± 0.07	0.79 ± 0.13
Our method	0.95 ± 0.05	0.90 ± 0.09	0.92 ± 0.04	0.84 ± 0.06

accuracy=(TP+TN)/(TP+TN+FP+FN), Jaccard Index = TP/(TP+FN+FP) and the results are summarized in Table 3.1.

The proposed method produced high sensitivity (0.95), specificity (0.90), accuracy (0.92) and Jaccard Index (0.84). In comparison, global threshold individually selected for each image by users, the space-variant hysteresis method, Otsu's method applying on the entire image and only in each of small ROIs are presented.

Overall, every method achieves a high sensitivity (≥ 0.93), which means that every method has successfully identified trabecular bone structures. However, the specificity has shown a great difference. Otsu's method applying globally on the entire image has shown lowest specificity of 0.70. Otsu's method applying on each ROI has shown better result of 0.79. The possible reason is that trabecular bone intensities across the whole MDCT images are nonuniform, rather a regional pattern likely occur such that the segmentation value of intensity to separate bone and marrow varies in different areas. Such effect has been visually observed and validated in Sec. 3.1.1. Manually selected global threshold has shown specificity of 0.75. The comparatively

low specificity indicates a problem that although these methods are able to identify trabecular bone network, the marrow hole are probably falsely filled, leading to violation of the topology of the whole network structure. Therefore the segmentation methods could influence the overall measurement of trabecular micro-architecture, including trabecular thickness, trabecular spacing, and etc. The space-variant hysteresis method uses the information of distance from cortical bone. Space-variant thresholds and hysteresis process are applied to capture the intensity variability. The algorithm is successful to partially compensate the variance of intensity and preserve marrow holes. The specificity was found 0.85, better than Otsu's and manual selected global thresholding scheme. Our proposed multi-scale morphological method greatly improved the segmentation by considering the variability of trabecular bone intensities in different regions automatically. It successfully identifies trabecular bone, sensitivity of 0.95, and avoids oversegmentation, achieving specificity of 0.90, which could preserve the marrow holes. Therefore, it is more accurate in computing trabecular bone micro-architectural measures. In addition, compared with the space-variant hysteresis method which requires a few critical parameters that need to be determined by experts from a set of in vivo images, the new algorithm is fully automatic and more robust to different imaging modalities. The proposed method also achieves the highest accuracy (0.92) and Jaccard Index (0.84). It is thus possible to conclude that the proposed algorithm is an accurate segmentation method of trabecular bone for in vivo imaging.

3.1.2.4 Ability to Predict Bone Quality Measures

To study the implication of the new TB segmentation method on the TB microstructural measures, we computed the thickness and spacing of TB network, from TB segmentations using the new and other methods and examined their abilities of predicting actual bone strength. For this purpose, twenty-two cadaveric ankle specimens were obtained from 11 body donors (age: 55-91 years). The ankle specimens were removed at the mid-tibia region. Exclusion criteria for this study were evidence of previous fracture of knowledge of bone tumor or bone metastasis. CT images were acquired using the same protocols as described in Sec. 3.3.1.

To determine TB strength, mechanical tests were applied on a cylindrical TB core from distal tibia of 8 mm in diameter and 20.9±3.3 mm in length for each subject using an electromechanical materials testing machine. To minimize specimen end effects, strain was measured with a 6 mm gauge length extensometer attached directly to the midsection of the bone. A compressive preload of 10 N was applied and strains were set to zero. At a strain rate of 0.005s^{-1}, each specimen was preconditioned to a low strain with at least ten cycles and then loaded to failure. Yield stress was determined as the intersection of the stress-strain curve and a 0.2% strain offset of the modulus.

The size and location of ROIs for image analysis was chosen as the information recorded during specimen preparation for mechanical tests. First the image was rotated to align the bone axis along the coordinate z-axis. Detailed descriptions can be found in the experiment section 3.3.1.
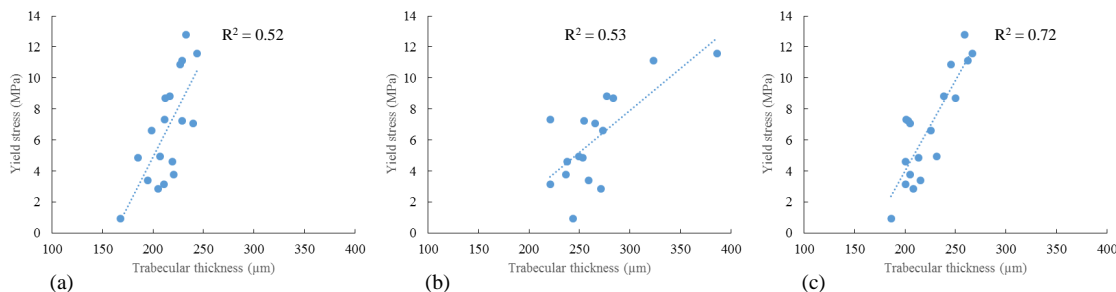
Figure 3.7: Ability to predict bone strength using TB thickness measures computed by different methods. Correlation between yield stress and TB thickness computed by manual global thresholding (a), Otsu's method (b), and our method (c).

The TB structures were obtained by segmentation using the proposed method, a global thresholding for each subject and Otsu's method. TB thickness was computed using the method described in [129]. The linear correlation between experimental yield stress and computed TB thickness is shown in Fig. 3.7.

As observed from the figure, the TB thickness measure using segmentation with the new method has higher correlation with actual bone strength as compared to those using TB segmentation with other two methods. The prediction error for each method was computed using the linear regression function. The paired t-tests of prediction errors showed that the prediction error of the new method was significantly smaller than the global thresholding (p = 0.03) and Otsu's method (p = 0.01), respectively.

The linear correlation between experimental yield stress and computed trabecular spacing is shown in Fig. 3.8. The new method has shown with $R^2 = 0.79$,
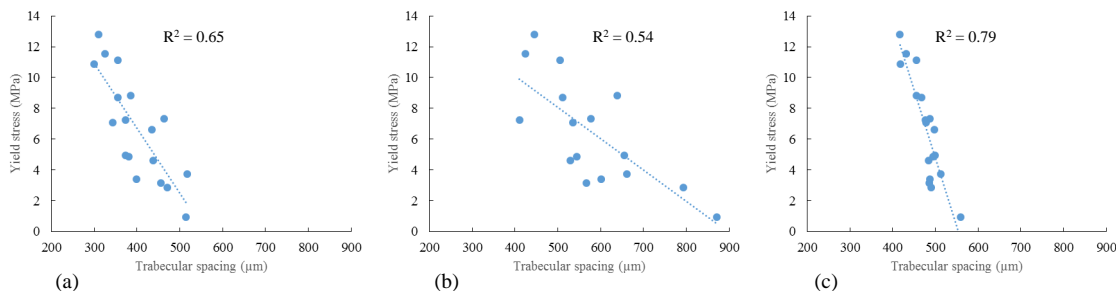
Figure 3.8: Ability to predict bone strength using TB spacing measures computed by different methods. Correlation between yield stress and TB spacing computed by manual global thresholding (a), Otsu's method (b), and our method (c).

better than Otsu's method and manually selected thresholds. The paired t-tests of prediction errors showed that the prediction error of the new method was also significantly smaller than the global thresholding ($p = 0.01$) and Otsu's method ($p < 0.01$), respectively. It can be explained as the new segmentation method has successfully identified trabecular network, as well as preserving marrow holes avoiding filling of marrow wholes or thickening of trabecular bone. Successful segmentation of trabecular network and marrow space preserve the topology of the structure, that is likely the reason computed thickness and spacing were found correlated with experimental yield stress. Together with the accuracy experiment, we may conclude that the new algorithm works well for trabecular bone segmentation for *in vivo* MDCT images.

In summary, a new TB segmentation algorithm using Hessian-based anisotropic diffusion and multi-scale morphological operations has been developed for *in vivo* CT imaging. Experimental results have established high sensitivity, specificity, and ac-

curacy of the new method as compared to manual global thresholding, space-variant hysteresis and individual ROI-specific regional thresholding with Otsu's method. The main reason behind the improved performance of the new segmentation method is that the method simultaneously accounts for background variation as well as local contrast. It was observed in experimental results of a cadaveric study that TB segmentation using the new method significantly improves the ability of computed TB thickness and spacing measure to predict actual bone strength determined by mechanical testing. These results reinforce the importance of accurate TB segmentation for assessment of TB micro-architecture and prediction of bone strength.

3.2   High Quality Mesh Generation

FEM has rigorous requirements of mesh. With respect to topology and geometry, FEM requires the mesh to be manifold, non-self-intersecting. With respect to precision, FEM relies on mesh quality determined by shape and size of elements [149]. A good mesh generator should guarantee the topological and geometrical correctness as well as producing elements with high quality. In this work, a high quality mesh generator is adopted, including a Delaunay surface mesh generator and a lattice-based volume mesh generator.

3.2.1   Surface Mesh Generation

Given volumetric imaging data I, surface mesh generator produces a mesh representation S of the isosurface $S = \{g(p) \mid g(p) = c, p \in I\}$, where each point on the surface has the same value c. c is a constant and f is an implicit function.

Specifically, in the application for TB surface generation, given the binary image I^*, $S = \{g(p) \mid p \in I^*\}$.

FEM has rigorous requirements of mesh. With respect to topology and geometry, FEM requires the mesh to be manifold, non-self-intersecting. With respect to sensitivity and precision, FEM relies on mesh quality determined by shape and size of elements. A good mesh generation method should have desired properties which guarantee the topological and geometrical correctness as well as producing elements with high quality.

In computer aided design, triangular mesh is the most common representation of surface mesh. Angles of triangles are therefore the measure of triangular mesh quality. Triangles with small angles are considered as bad elements, for example, a triangle whose smallest angle is less than 1 degree. The sensitivity of FE model is impacted by bad elements of the mesh. In other words, the ability of avoiding bad elements is the key to quality mesh generation.

Surface mesh generation algorithms for FEM are expected to produce elements with good quality that guarantee topology and geometry as well as being timely and computationally efficient. However, it is theoretically difficult for mesh generation algorithms to meet all desired properties. Among various methods for surface meshing in literature, they can be classified into three categories: lattice based method, dual based method, and Delaunay based method. Here, only the most widely used and applicable to FE modeling are reviewed.

Lattice based methods guarantee topology and geometry but fail to generate

mesh of good quality. Marching Cubes [103] is the most well-known and widely used method [180]. Marching Cubes iterates along the rectilinear grid, classifies each voxel into a predefined case depending on the local information of the voxel and produces triangular surface mesh. The advantage of Marching Cubes is that it is fast, easy for implementation, and generates manifold isosurface. However, the main drawback is that the triangular mesh may include triangles with small angles (less than 0.1 degree), which does not meet the criteria of FEM simulations. Therefore, a post-processing step is often inevitable to smooth the mesh and improve the quality. It requires additional time while the quality of surface mesh may not be guaranteed.

Dual based methods preserve features of the surface and produces triangles with adaptive sizes and thus time and memory efficient. However, these methods suffer from non-manifold elements and elements of bad quality. Dual Contouring (DC) [49] introduces the perception of dual grids. Octree is used to represent volumetric data. Therefore, sizes of triangles can be controlled by depth of the octree. An edge e with two end points $p, q \in I$ is marked as sign-change edge when $p \in S$ and $q \in S$. Whenever a sign-change edge is found, DC creates a dual edge and construct quads using dual edges. It is shown that dual edges could approximate the surface S and preserves sharp features of S by minimizing a quadratic error function. The advantage of DC is that it is adaptive in resolution, computationally efficient and preserves sharp features of the surface. However, the surface mesh generated by the original DC is non-manifold and also ambiguous under certain circumstances. Improved DC [182] addresses the ambiguity but the generated surface mesh is still

non-manifold. Similar to the lattice based methods, a post-processing step is necessary to improve quality of generated triangles. Yet, no guarantee of good qualities is ensured while non-manifold situations add difficulty for the post-processing procedure.

Delaunay based methods generate triangles subject to the given surface point set I^* to approximate the topology of the surface, where triangles satisfy the Delaunay criteria. Unlike lattice based and dual based method, Delaunay based methods are not heuristic and are strictly restricted by the Delaunay criteria. Therefore, Delaunay based methods can precisely state properties of the surface and generate surface mesh of good quality. Compared with lattice based and dual based methods, Delaunay based methods require more time and memory. Nevertheless, the ability to generate guaranteed quality mesh makes it suitable for FE calculation. Recently, Boissonnat and Oudot [14] introduce a Restricted Delaunay Triangulation (RDT) algorithm that returns a manifold, non-self-intersecting, topology preserving triangular surface mesh with provably good triangular quality. RDT iteratively computes Delaunay triangles and adds new points onto the surface to preserve desired properties, i.e., Delaunay criteria and manifold topology. The intersection point of the triangles dual edge on the corresponding Voronoi Diagram with the surface is added when the radius of triangles circumsphere is larger than a fraction of the distance from the point to the nearest point on the medial axis. Then the Restricted Delaunay Triangulation is locally updated, after which the manifold topology and Delaunay criteria are both satisfied.

Therere two major advantages of the RDT algorithm. First, the algorithm is proved to generate triangular mesh with the smallest angle larger than a user specification as long as it is no larger than 30 degree. The provable bounded angles ensure the availability for further FE calculations. Second, the algorithm eliminates the unnecessary time consuming post-processing step for quality improvement, which is a crucial component for lattice based and dual based methods to get satisfactory surface mesh quality. Besides, the post-processing step often relies on smoothing and is possible to break the correctness of topology and geometry, for example, introducing self-intersections or invert elements.

In the framework, the RDT based method is used as the surface mesh generator because of its desirable properties for FEM simulation. With the help of CGAL [165], surface mesh is generated with provably good mesh quality. The minimum angle is 30 degree and the maximum angle is 150 degree.

3.2.2   Volume Mesh Generation

Given surface mesh S, volumetric mesh generator produces a polygonal representation V of the interior volume of S. S_V, the surface of V, is an approximation to the isosurface S. Among feasible polygonal representations, tetrahedron is the dominant representation and attracts the most research interests. The equilateral tetrahedron with all dihedral angles equal to $\arccos(1/3) \approx 70.5$, is the ideal high-quality element. Divergence of dihedral angles from the ideal value measures the quality of tetrahedron elements. Specifically, minimum and maximum dihedral an-

gles of V have a great influence on the quality of volume mesh since they slow the convergence and reduce sensitivity of FEM simulations. Aspect ratio is another measurement for mesh quality. It is the ratio of the length of the longest edge over the shortest edge. Ideally, the best aspect ratio is 1 (equilateral tetrahedron). Large aspect ratio indicates the element is thin and ill-shaped.

Over the past two decades, an extensive study on volume mesh generation has been performed [171]. Various methods has been proposed to generate volumetric mesh with high-quality tetrahedron elements. These techniques can be classified into four categories: advancing-front-based, octree-based, Delaunay-refinement-based, and lattice-based methods.

Advancing-front-based methods generate tetrahedron elements by inserting Steiner points or elements inside the domain heuristically so that new elements satisfy desired size and shape criteria [1]. This technique preserves the input surface and terminates until the whole volume is tetrahedralized. An inevitable and difficult step is merging fronts because of intersections generated during the algorithm. Although advancing-front-based methods are fast, they cant offer any guarantees of mesh quality. As a result, in reality, global smoothing steps are usually required to improve the output quality. Still, mesh quality is not guaranteed and bad elements may exist.

Octree-based methods produces tetrahedron elements of adaptive sizes by controlling the octree depth. It subdivides the domain recursively into cubical cells adaptively according to local grid information. The advantage is that total number of elements of the domain is much less compared with uniform methods. Therefore,

it reduces computational time since computation in FEM simulation is determined by number of elements. Several variants are proposed to generate high quality mesh. Shephard et al. [148] introduced Finite Octree method which reproduces features of the input surface. Bielak et al. [11] presented a parallel method to speed up mesh generation. Mitchell and Vavasis [110] offer octree mesher with theoretical guarantee of avoiding bad tetrahedral by generalizing the quadtree mesher of Bern et al. [10] from two dimension to three dimensions.

Delaunay-refinement-based methods generates tetrahedron elements by inserting points to enforce tetrahedra satisfying constraints on size and quality, as well as maintaining a Delaunay or constrained Delaunay triangulation [150]. These methods produce volume mesh with surface exactly the same as the input. Delaunay criteria optimizes the radius to edge ratio but it doesnt guarantee dihedral angles in three dimension. Therefore, slivers, where the tetrahedron element has a good radius to edge ratio but dihedral angles can be arbitrarily between 0 and $180°$, may occur, and the near coplanar area of slivers may be over-refined [37]. Chew [39] presented an algorithm to eliminate most slivers. Cheng et al. [36] presented a technique called sliver exudation that takes as its input a Delaunay triangulation with good radius to edge ratios and returns output mesh without extremely bad slivers. Alliez et al. [1] proposed a variational algorithm to generate isotropic tetrahedral mesh and achieved to generate elements with good shape. However, slivers may still survive and there is no guarantee to completely remove them. In practical conditions, these methods usually eliminate most skinny tetrahedron elements and generate satisfactory volume

meshes. Tetgen [151] is arguably the most popular mesh generator. It generates exact constrained Delaunay triangulation and boundary conforming meshes by adding Steiner points to control user-specific element size.

Lattice-based methods construct rectilinear grids and generate tetrahedron elements based on pre-computed stencils. Labelle and Shewchuk [84] present a lattice-based algorithm called Isosurface Stuffing (IS) based on body centered cubic (BCC) lattice and prove that the generated volume mesh has bounded dihedral angles guaranteed by the computer-assisted proof. Bounded dihedral angles are between $10.7°$ and $164.8°$. The algorithm works similar to Marching Cubes algorithm except that a point snapping technique is introduced to adjust points on the surface to meet the quality and topology requirement. IS is one of few algorithms that provides theoretical guarantees on dihedral angles and generated mesh with good quality. Inspired by this method, Doran [45] introduces an algorithm using A15 lattice grid. Wang and Yu [171] propose a robust meshing algorithm based on adaptive BCC lattice grid, offering bounded dihedral angles larger than $10°$ if uniform mesh is generated and $5.71°$ in adaptive case. The drawback of these methods is that generated surface mesh is not exactly the same as the input because the point snapping procedure relocates several surface points.

In this work, IS is selected since it is the most recently developed technique for quality mesh generation and one of few guaranteed quality mesh generating algorithm.

The surface and volume mesh generation are both guaranteed to produce mesh of high quality, which ensures FEM simulation to be reliable and accurate. In addi-

tion, the mesh generator is also applicable to other types of imaging modalities and various applications. It is also a general tool for FEM modeling in a broader range.

3.3 Finite Element Modeling of Cadaver Study

3.3.1 Experiment

The experiment was designed to evaluate the advanced finite element model using mechanical tests on human cadaveric data in MDCT imaging. First, the reproducibility of computed Young's modulus (YM) across repeat scans was examined. Second, the relation between the computed YM and actual YM determined by mechanical test was studied. In comparison, we also present the result using the basic brick model that is widely used in bone study [50, 47].

Specimen preparation for mechanical testing:

Cylindrical TB specimens nominally 8 mm in diameter and 20.9±3.3 mm in length were cored from each distal tibia specimen in situ along the proximal-distal direction for mechanical testing. A-P and M-L radiographs were first used to determine the plane of an initial distal cut done to eliminate the growth plate from a test specimen, and then to determine the central axis of the bone and thus the core location; the initial distal cut was located 2 mm proximal to the growth plate. Each specimen was cored with saline immersion using an 8.25 mm inner diameter diamond coring bit (Starlite Industries, Rosemont, PA). The core was released from the distal radius by cutting it with a razor saw, and the specimen ends were sanded smooth, flat, and parallel. Specimen length and diameter were measured three times and
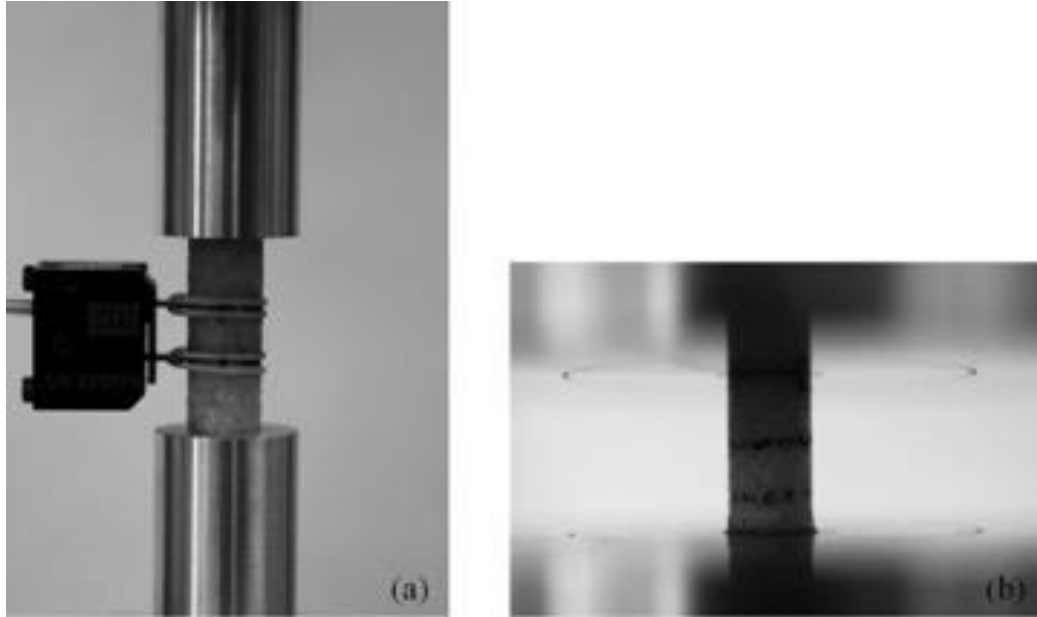
Figure 3.9: Mechanical tests of trabecular bone.

averaged, and the middle 6 mm of the specimen length was marked for extensometer attachment position.

Mechanical testing:

Compressive Youngs modulus of each TB core was mechanically determined on an electromechanical materials testing machine (MTS Insight, MTS Systems Corp., Eden Prairie, MN). Each specimen was placed between unlubricated, polished, plano-parallel steel platens. To minimize specimen end effects, strain was measured with a 6 mm gage length extensometer (model 632.29F-30, MTS Systems Corp., Eden Prairie, MN) attached directly to the midsection of the bone. A compressive preload of 10 N was applied and strains then set to zero. At a strain rate of $\sec^{-1}$, each specimen was preconditioned to a low strain with at least ten cycles and then loaded to failure.

Youngs modulus (E) was determined for each specimen as the highest 20% section slope of the stress-strain curve.

MDCT imaging.

Twenty two fresh-frozen human cadaveric ankle specimens were obtained from 12 body donors (age at death: 82.3 ± 12.5 years). The bodies were collected under the Deeded Bodies Program, The University of Iowa, Iowa City, Iowa, USA, and the ankle specimens were removed at mid-tibia. Exclusion criteria for this study were evidence of previous fracture or knowledge of bone tumor or bone metastasis. The ankle specimens were kept frozen until MDCT and μ-CT Imaging.

High resolution MDCT scans of the distal tibia were acquired at the University of Iowa Comprehensive Lung Imaging Center on a 128 slice SOMATOM Definition Flash scanner (Siemens, Munich, Germany) using the following CT parameters: Single tube Spiral acquisition at 120 kV, 200 effective mAs, 1 sec rotation speed, pitch factor: 1.0, nominal collimation: 16×0.3 mm, scan length of 10 cm beginning at the distal tibia end-plateau and total effective dose equivalent:17 mrem $\approx$ 20 days of environmental radiation in the USA. One AP projection scout scan of the entire tibia was acquired to locate the field of view (FOV) for the CT scan. High resolution MDCT scan mode: The Siemens Flash scanner has two 64 rows of equal 0.6 mm detectors under two X-ray guns allowing operation in both single and dual source scan modes. The highest resolution single gun scan mode was used, which activated 16 of the most inner 0.6 detectors to maximize beam quality. Siemens double z sampling allowed for a dual sampling of the 0.6 mm detectors, splitting the signal so that

each detector created a 0.3mm slice in the z plane [80]. As specified by the manufacturer, the z-UHR scan mode within the Siemens Flash scanner enabled high image detail with a maximum achievable isotropic resolution of 30 lp/cm (0.17 mm) at 0% modulation transfer function (MTF) ($\pm$ 10 %) and thus provided a more accurate slice profile and lowered partial volume artifact allowing for better separation of TB structures. After scanning each specimen in a helical mode with a 0.4 mm slice thickness, data were reconstructed at 0.2 mm slice thickness using a normal cone beam method with a special U70u kernel achieving high structural resolution. A calibration phantom was scanned once per specimen to calibrate CT Hounsfield units into BMD (mg/cm^3). Three repeat MDCT scans of each distal tibia specimen were acquired after repositioning the specimen on the CT table before each scan. Following MDCT repeat scans, each specimen was further scanned on an Imtek Micro-cat II scanner at 28.8 μm isotropic resolution, after removing soft tissue and dislocating the tibia from the ankle joint.

ROI Selection.

The objective of ROI selection for the cadaveric study was to select a region that is close to the region that was drilled during specimen preparation for mechanical testing. Size and location of these ROIs were chosen as per the information recorded during specimen preparation for each experiment. First, the bone was oriented to align its axis along the coordinate z-axis using the following two steps (1) generation of a cylinder C with its axis lying on the coordinate z-axis and its cross-sectional area equating the average tibial cross-sectional area, and (2) reorientation of the tibial vol-

ume to align its axis with C by maximizing the overlap between the tibial volume and the cylinder C. After reorienting the bone image, a ROI cylinder of 8 mm diameter along the coordinate z-axis was generated and its proximal end was manually positioned at the center of the cortical rim using in-plane translation through a graphical user interface. The location of the distal end of the ROI cylinder in the slice direction and its length were determined as per the core location and length recorded during specimen preparation; the growth plate was visually located in the CT data of each specimen. Finally, the central 6 mm region from the cylinder was used as ROI for the extensometer test.

FEM Simulation.

A linear FEM simulation model is applied on the generated volume mesh V to compute the compressive YM. A trabecular subject is modeled as an isotropic, linear elastic material with a YM of 10 GPa, and a Poisson ratio of 0.3. Abaqus is used as the FEM simulator. A uniaxial displacement equaling 2% of the bone segment height was applied perpendicularly to the distal surface of the tibia for determining axial strength. Bottom of the cylinder is fixed and constant forces are applied onto the top plane, which simulates the real mechanical test.

3.3.2   Results

The reproducibility of computed compressive YM across repeat scans is shown in Fig. 3.10. Intra-class correlation coefficient (ICC) values of the proposed model and the brick model were both 0.97. The result indicates that the proposed model and
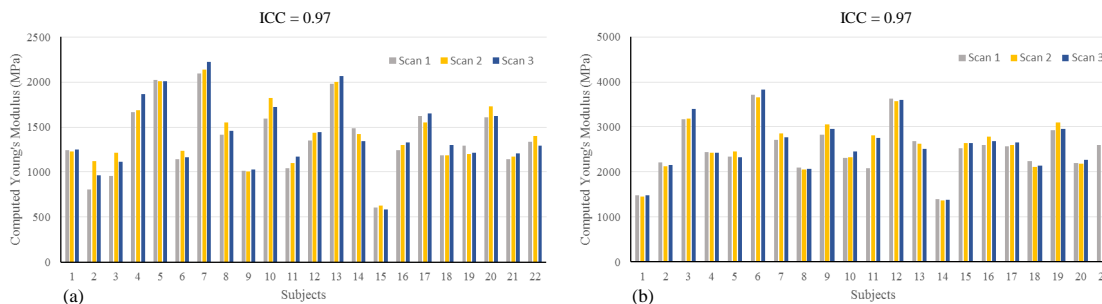
Figure 3.10: Intra-class correlation coefficient of three repeat scans of MDCT images from cadaveric subjects. (a) Proposed finite element model. (b) Brick model.

the brick model are both highly reproducible. In addition, the fact that both models achieve high reproducibility indicates that the new segmentation method worked equally well on repeat scans.

The correlation between averaged YM computed from two models and the actual YM determined by mechanical test is presented in Fig. 3.11. The YM of each subject is the average value of three repeat scans. The linear regression revealed that averaged YM computed with the advanced model was highly correlated (R^2=0.83) with the actual YM. In comparison, averaged YM computed with the brick model showed much less association (R^2=0.71). Since input images are the same and the only difference between these two models is the mesh, we owned the ability of accurately predicting TB strength to the high quality mesh generator.

In summary, a new segmentation method has been presented that effectively preserves TB network connectivity and guarantees a lower bound of mesh quality for FEM. The method is found highly reproducible under repeat MDCT scans. In a
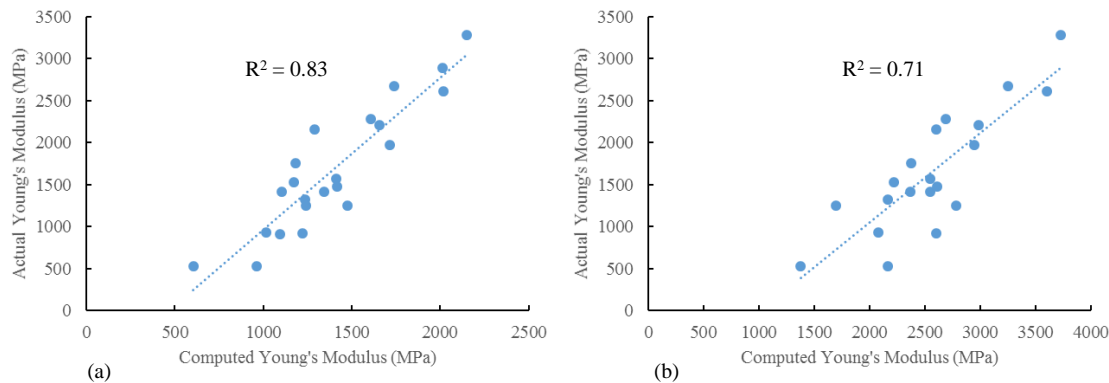
Figure 3.11: Bone strength correlation between computed Young's modulus and actual Young's modulus. (a) Young's modulus computed with advanced finite element model. (b) Young's modulus computed with the brick model.

cadaveric ankle study, a high linear correlation has been observed between computed bone strength using the new method and the actual strength determined experimentally. The new method improves the accuracy of applying FEM on *in vivo* MDCT imaging under limited spatial resolution. Therefore it enables us to apply FEM on human *in vivo* studies. In the following sections, I will present the application of the FEM onto different human groups.

3.4   Finite Element Modeling of Human Study

3.4.1   Experiment

Subjects.

In the study, several groups of human subjects are obtained. Studies involving human subjects were approved by the University of Iowa Institutional Review Board and all participants provided written informed consent. In total, four different human

groups are involved: Iowa Bone Development Study (IBDS), pilot selective serotonin reuptake inhibitors (SSRI) subjects, and pilot cystic fibrosis (CF) subjects.

In a human pilot study, eleven patients (5 male) with cystic fibrosis (CF), twelve patients (6 male) on continuous treatment with the SSRI-treated patients (male: height mean±SD 180.1±3.5 cm weight 86.0±16.1 kg; female: height 163.3±7.7 cm, weight 70.1±13.6 kg) were matched with an age-similar group of healthy IBDS cohort members (controls) by sex, height, and weight using a variable optimal matching algorithm with two to four controls/patient (total 36 controls). MDCT scans of the distal tibia and whole body (WB) DXA were acquired. The preliminary results from our pilot study indicate that ultra-high resolution CT imaging, together with our advanced computational algorithm are well-suited to detect structural differences in cortical and TB compartments with divergent fracture risk.

MDCT images of distal tibia bone scans were obtained for 46 healthy males and 51 healthy females (age: range 19 to 20 years; 19.4±0.4 years) as part of the ongoing Iowa Bone Development Study (IBDS). In general, observed heights and weights for male participants (height 180.4 ± 8.0 cm, weight 83.6 ± 14.8 kg) were greater that female participants (height 165.2 ± 6.8 cm, weight 67.9 ± 21.0 kg). MDCT scans were obtained on the left lower leg using the MDCT protocol.

MDCT Imaging

High resolution MDCT scans of the distal tibia were acquired at the University of Iowa Comprehensive Lung Imaging Center on a 128 slice SOMATOM Definition Flash scanner (Siemens, Munich, Germany). More details are described in Sec. 3.3.1.

(a)   (b)
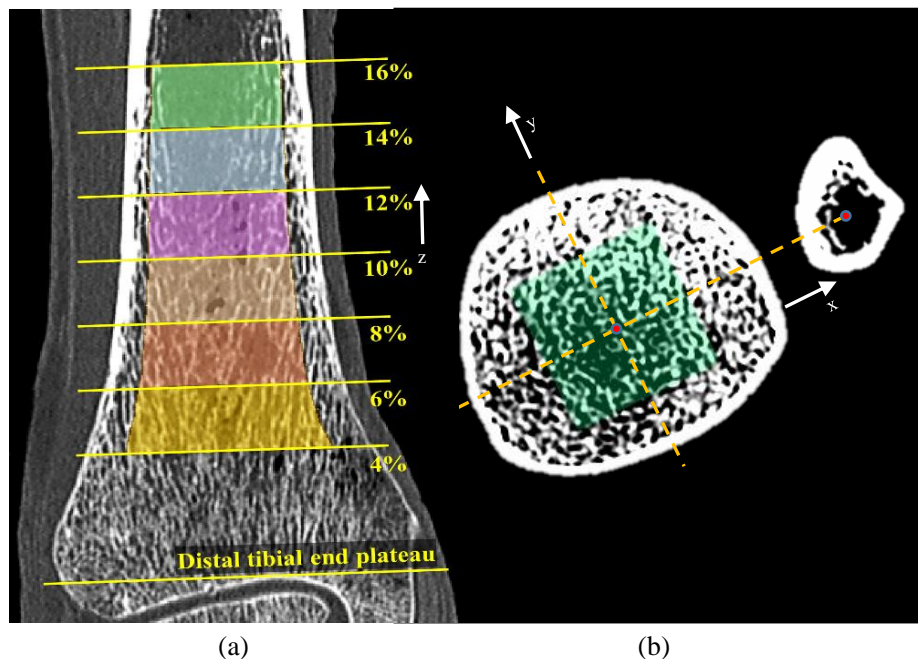
Figure 3.12: Subject-specific ROIs for bone measures on human distal tibia. This ROI selection scheme eliminates size-related bias for individuals distal tibias and distal radii.(a) different ROIs with respect to tibia vertical distance, (b) cubical ROI determined by centers of gravity of tibia and fibula. The coordinate system and directions are specified.

ROI Selection.

Trabecular bone structure in human distal tibia varies according to the vertical distance to the most distal point (Fig. 3.12(a)). Trabecular bone network near and below the growth plate is much denser than that in the proximal end. It is observed that trabecular bone structure that is further from the most distal point has less density in human distal tibia. Clinically, identifying the anatomical significance of

different regions of trabecular bone structure is an interesting research area. However, it is beyond the scope of this study. Here, to select ROIs that is reliable and capable of differentiating properties of trabecular bone network, we take distance, direction, peeling, etc into consideration. First, the distal tibia and fibula bone image were automatically filled and aligned to Z-axis using the algorithm described in [81]. ROI of 4-8% of vertical bone length from the most distal point was used. After that, for each slice, a ROI was obtained by applying 45% peel from the cortical bone. Center of gravity (CG) of tibia was computed for each slice in 4-8%. Then a cubic ROI was generated such that its volume is the same as the peeling ROI. The averaged CG (red point in Fig. 3.12(b)) is the center of the cubic ROI. The cubic ROI was then reoriented such that the line joining CG of tibia and fibula is perpendicular to the edge of the cubic ROI (Fig. 3.12(b)). By using the fibula as the reference direction, the ROI is anchored and reliable across different subjects. We refer the direction that joining two center of gravities as X axis. The perpendicular direction to X in the same plane is Y axis. And Z is vertical axis.

FEM Simulation:

A linear FEM simulation model is applied on the generated volume mesh V to compute the compressive YM. A trabecular subject is modeled as an isotropic, linear elastic material with a YM of 10 GPa, and a Poisson ratio of 0.3. Abaqus is used as the FEM simulator. A uniaxial displacement equaling 2% of the bone segment height was applied perpendicularly to the distal surface of the tibia for determining axial strength. Bottom of the cylinder is fixed and constant forces are applied onto the top

plane, which simulates the real mechanical test.

For the cubical ROI defined for human studies of distal tibia, Fig. 3.12, we compute FEM modulus measures: compressive Young's modulus along X, Y, Z direction and shear modulus along six directions, named as X_shear_Y, X_shear_Z, Y_shear_X, Y_shear_Z, Z_shear_X, Z_shear_Y. X_shear_Y represents the direction that the object is fixed on one side of the bounding box of X direction, and the other side is sheared along Y direction. Similar naming convention applies to other directions.

3.4.2   Data Analyses

Matching criteria:

(1) Separate matching by gender to get equal percentage of male and female subjects in case and control groups. Two matching variables are included: height (weight=1), scale weight (weight=1).

(2) Total number of matched IBDS subjects equals (number of pilot group subjects) $\times$ 3 with equal proportion of female subjects in case and control group.

(3) Minimize distance between groups as $D_{ij} = \sum w_k * |X_k^i - X_k^j|$, where the sum is over the number of matching factors X (with index k) and w_k is the weight assigned to matching factor k and X_k^i is the value of variable X_k for subject i.

Two-sample analysis:

In the two-sample analysis, three controls per one case were selected. Results for t-tests with equal variance were reported if tests for equality of variances (p-value > 0.15), otherwise Satterthwaites method was used. Since all pilot groups have small

Table 3.2: Two-sample analysis result for cystic fibrosis group. Three controls per case are used for matching IBDS group.

	Case	N=11	Control	N=33	T-test	Wilcoxon	Effect size
Variable (MPa)	Mean	StdDev	Mean	StdDev	p-value	p-value	
X_shear_Y	14.1305	10.666	21.5817	6.8404	0.0491	0.0258	-0.76
X_shear_Z	23.9874	17.9991	32.9859	10.3448	0.141	0.0322	-0.55
Y_shear_X	15.1402	11.8444	23.1888	8.5376	0.0185	0.0154	-0.85
Y_shear_Z	22.6034	17.842	35.9224	15.6507	0.0229	0.0064	-0.82
Z_shear_X	60.6436	28.1412	80.8895	17.663	0.0433	0.0423	-0.78
Z_shear_Y	55.303	25.7149	82.759	17.8595	0.0057	0.0009	-1.14
compressive_X	91.2501	60.5427	128.1	45.975	0.0394	0.0917	-0.74
compressive_Y	90.7846	55.6138	140.1	58.316	0.0286	0.0452	-0.79
compressive_Z	585.0	249.1	775.8	128.3	0.0317	0.0268	-0.85

size, non-parametric exact Wilcoxon rank-sum test was used to confirm t-test results.

Paired analysis:

In accordance with two-sample analysis, results for comparison with control group use three controls per one case. Non-parametric Wilcoxon matched pairs signed ranks exact test (SRT) p-value was used. Effect size was defined as mean paired difference standardized by its standard deviation.

3.4.3 Results and Discussions

3.4.3.1 FEM distinguishes bone quality between different groups

Statistical analysis has been applied on FEM measures for CF, SSRI and IBDS groups. The independent two-sample t-test analysis tests whether there is

Table 3.3: Two-sample analysis result for SSRI group. Three controls per case are used for matching IBDS group.

	Case	N=11	Control	N=33	T-test	Wilcoxon	Effect size
Variable (MPa)	Mean	StdDev	Mean	StdDev	p-value	p-value	
X_shear_Y	13.5288	6.1826	20.122	6.7297	0.0058	0.0052	-0.96
X_shear_Z	22.8241	10.221	28.9161	11.0306	0.1103	0.131	-0.54
Y_shear_X	15.3441	7.789	21.0937	6.6449	0.0166	0.0454	-0.83
Y_shear_Z	25.8757	15.7176	29.416	11.1488	0.4815	0.2709	-0.24
Z_shear_X	62.0204	26.3268	78.4332	23.5016	0.0477	0.0282	-0.68
Z_shear_Y	59.8147	27.066	74.8339	19.5226	0.0963	0.063	-0.59
compressive_X	92.5293	44.7407	122.6	50.9398	0.0747	0.0389	-0.61
compressive_Y	89.9111	45.4566	120.4	46.0155	0.052	0.1134	-0.66
compressive_Z	595.1	237.3	689.3	161	0.2201	0.1287	-0.43

a significant difference between means of two independent samples from a normal distribution. Here, pilot groups are CF and SSRI. IBDS group consists of healthy age-, gender-, height-, and weight-matched volunteers, and three controls per case for pilot group are used. The paired t-test is also using three controls per case.

The comparison of CF and IBDS group is summarized in table 3.2. T-test p-value of two-sample analysis has shown all measures but X_shear_Z are significantly different in the mean values between these two groups. T-test p-values in paired analysis (table 3.4), reported X_shear_Z, Z_shear_X, and compressive_X were not significant. The CF group were found of less mean values of each measure than the healthy controls.

For CF group, the deficit in mean values of each measure suggest that trabecular structure is weaker than normal healthy young people. The observation agrees to previous studies [5] that $50 - 75\%$ of adults with CF have low bone density and increased rates of fractures. Compressive_Z measure of CF group was found with 24.49% less than the healthy groups and the difference is statistically significant. According to Wolff's law, the remodeling of trabecular bone reacts to the load under which it is placed. Since the bone structure needs to carry the body weight, trabecular bone along the Z direction undertakes more compressive loads than other trabecular compartments, which is also shown in mean values (table 3.4). The significant deficit in compressive modulus along Z direction is a strong signal of bone quality.

The comparison of SSRI and IBDS group is summarized in table 3.3. Compressive measures were not found significant. Significant differences were found in shear directions, including X_shear_Y, Y_shear_X, Z_shear_X. Paired analysis results (table 3.5) also reported significant difference for the three directions.

For SSRI group, deficit in mean values of each measure was also found. It indicates the trabecular structure is not as strong as the healthy controls. Evidence in literature has reported loss of bone mass in SSRI patients [172]. In a previous study, the same SSRI group was reported with 12.5% lower mean TB plate-width ($p = 0.052$) as compared to age-similar and sex-, height-, and weight-matched healthy controls. In this experiment, the compressive modulus along Z direction was found 12.9% less but not significant. The deficit of mean values of compressive and shear modulus suggests that trabecular network in X-Y direction is of higher differences.

Table 3.4: Paired analysis result for cystic fibrosis group. Three controls per case are used for matching IBDS group.

Variable (MPa)	Case Mean	N=11 StdDev	Paired Mean	Diff StdDev	% Diff	Paired t-test p-value	SRT p-value	Effect size
X_shear_Y	14.1305	10.666	-7.4512	10.4628	-34.94	0.0398	0.0674	-0.71
X_shear_Z	23.9874	17.9991	-8.9985	17.9769	-26.83	0.1279	0.123	-0.5
Y_shear_X	15.1402	11.8444	-8.0486	11.3576	-35.76	0.0406	0.1016	-0.71
Y_shear_Z	22.6034	17.842	-13.319	16.8204	-37.9	0.0253	0.0674	-0.79
Z_shear_X	60.6436	28.1412	-20.2458	32.1258	-22.7	0.0631	0.1748	-0.63
Z_shear_Y	55.303	25.7149	-27.456	24.2782	-33.55	0.0038	0.0049	-1.13
compressive_X	91.2501	60.5427	-36.8948	68.8773	-24.9	0.106	0.1475	-0.54
compressive_Y	90.7846	55.6138	-51.7231	54.2601	-35.9	0.0212	0.0391	-0.95
compressive_Z	585.0168	249.0998	-190.801	247.1914	-24.49	0.0284	0.0674	-0.77

It is possible the deterioration happens first in X-Y plane, while trabecular network must sustaining body weight in Z direction and therefore is less variant compared with healthy groups.

3.4.3.2 FEM and quantitative bone micro-structural measures

Studies of human trabecular bone developed from DXA and BMD analysis to advanced imaging methods and FEM. Micro-structural methods that measure the quality of trabecular bone has been found more accurate and sensitive than the BMD [121, 34]. FE methods provide information of bone strength and simulates the behavior of the bone network. It is therefore worth investigating the relations between

Table 3.5: Paired analysis result for SSRI group. Three controls per case are used for matching IBDS group.

Variable (MPa)	Case Mean	N=11 StdDev	Paired Mean	Diff StdDev	% Diff	Paired t-test p-value	SRT p-value	Effect size
X_shear_Y	13.5288	6.1826	-6.6686	5.4685	-33.02	0.0023	0.0029	-1.22
X_shear_Z	22.8241	10.221	-6.174	9.559	-20.09	0.0578	0.042	-0.65
Y_shear_X	15.3441	7.789	-5.7496	7.241	-26.78	0.0189	0.0425	-0.79
Y_shear_Z	25.8757	15.7176	-3.5403	15.0165	-10.82	0.4314	0.2036	-0.24
Z_shear_X	62.0204	26.3268	-16.4128	24.8777	-20.39	0.0431	0.0522	-0.66
Z_shear_Y	59.8147	27.066	-15.0192	26.8314	-19.1	0.0786	0.1294	-0.56
compressive_X	92.5293	44.7407	-30.1051	36.8998	-24.79	0.0165	0.0122	-0.82
compressive_Y	89.9111	45.4566	-30.5043	44.8013	-23.72	0.0379	0.0425	-0.68
compressive_Z	595.0562	237.3089	-94.2776	234.7836	-12.9	0.1917	0.2036	-0.4

trabecular bone micro-architectural measures using quantitative imaging methods and measures of FEM.

In this work, I have constructed a comprehensive set of quantitative measures using advanced imaging algorithms and a framework of FEM using *in vivo* MDCT imaging. It is a interesting to explore the connections or correlations between imaging based measures and FEM outcomes.

First, we consider the compressive Young's modulus computed using the FEM framework. Linear correlation was computed between compressive Young's modulus and other bone measures on different study groups. Compressive Young's modulus reflects the stiffness of trabecular structure and is therefore an important overall in-

dicator of bone quality. For compressive Young's modulus along X, Y, Z directions, BMD was found not a good predictor, which is not in accordance to common knowledge that BMD explains 60-70% variances of bone strength. A further study is needed to better understand the relation of BMD and compressive modulus.

Table 3.6: Correlations between finite element measures and micro-architectural measures of SSRI group.

	lBMD	pBMD	PW
Compressive X	0.39	0.68	0.76
Compressive Y	0.24	0.23	0.38
Compressive Z	0.48	0.66	0.83
X_shear_Y	0.02	0.01	0.04
X_shear_Z	0.01	0.04	0.08
Y_shear_X	0.36	0.38	0.55
Y_shear_Z	0.21	0.35	0.45
Z_shear_X	0.44	0.54	0.74
Z_shear_Y	0.4	0.38	0.57

Trabecular bone is often classified into plate and rod [139, 134]. An increasing evidence in literature [121, 34] suggests that the amount of plate structure reflects the quality of bone. More plate structure often means better quality bone structure. I hypothesize that the compressive modulus has a correlation with the plate structure. With the VTA and tensor scale algorithm, I am able to define BMD of plate-like trabecular bone, denoted as pBMD, and the average plate-width of trabecular bone,

Table 3.7: Correlations between finite element measures and micro-architectural measures of CF group.

	lBMD	pBMD	PW
Compressive X	0.65	0.61	0.62
Compressive Y	0.69	0.73	0.75
Compressive Z	0.65	0.67	0.74
X_shear_Y	0.61	0.63	0.64
X_shear_Z	0.43	0.47	0.51
Y_shear_X	0.52	0.56	0.57
Y_shear_Z	0.32	0.38	0.41
Z_shear_X	0.69	0.65	0.71
Z_shear_Y	0.67	0.65	0.72

denoted as PW. High correlations were observed between compressive Young's modulus along Z direction and pBMD, R^2 is 0.66, 0.67, 0.77, for SSRI, CF, and IBDS groups, respectively. In addition, PW was found more correlated with compressive Young's modulus, R^2 is 0.83, 0.74, 0.90, for SSRI, CF, and IBDS groups, respectively. It is an interesting and encouraging result that trabecular bone micro-architecutral measures have a close bond with compressive Young's modulus determined by FEM. Both imaging based algorithms and FEM methods provide irreplaceable information and characterization of trabecular network properties. They together could offer a better understanding of trabecular bone.

Besides compressive modulus, other interesting results were observed for shear modulus. Unlike compressive modulus, especially the one along Z direction, which

Table 3.8: Correlations between finite element measures and micro-architectural measures of IBDS group.

	lBMD	pBMD	PW
Compressive X	0.24	0.49	0.61
Compressive Y	0.19	0.36	0.36
Compressive Z	0.22	0.77	0.90
X_shear_Y	0.24	0.51	0.56
X_shear_Z	0.15	0.47	0.59
Y_shear_X	0.27	0.51	0.57
Y_shear_Z	0.15	0.38	0.41
Z_shear_X	0.24	0.64	0.77
Z_shear_Y	0.24	0.63	0.70

could be explained as body weight loading to the trabecular network, shear modulus could be interpret as the unusual forces loading to bone, for example, sports activity, falling, crushing. According to Wolff's law, trabecular bone network seldom reacts to these uncommon forces, thus it is more difficult to predict the properties of shear modulus. Nevertheless, we still find interesting results. First, BMD was not well correlated with shear modulus. Possibly, BMD isn't a good linear predictor. It may indicate that FEM describes properties of trabecular bone that are not overlapped with those BMD could explain, at least not in a simple linear form. Second, shear modulus has shown strong directionality in this study. The shear modulus along Z direction correlates better with lBMD, pBMD, PW, than that along X or Y direction, in every group. In comparison, shear modulus along X and Y direction doesn't show

significant difference. It can be explained as the shear modulus along Z direction is more meaningful while X, Y direction doesn't have a clear geometric meaning. It is possible that trabecular network has almost the same ability dealing with the shear force from any direction perpendicular to Z. And shear of trabecular structure along Z direction is a regular behavior and thus more predictable by micro-architectural measures.

This study has proposed a new angle of understanding trabecular bone network. Micro-architectural measures from digital and volumetric algorithms and FEM describes different aspects of bone architecture. The relation between these different measures could help us to reveal the mechanism of bone and inspire to discover new and more accurate means to model the complex trabecular network system. A few hypotheses were proposed but not experimentally validated, and therefore the study is preliminary. Designing appropriate experiments is difficult because various methods and algorithms are involved. And the most challenging problem is the limitation of resolution under *in vivo* MDCT imaging. It is necessary to start from μ-CT scans with high resolution that is reliable and accurate, which is often considered as the ground truth. Although the study in this work has lots of physical limitations, we successfully constructed a FEM system that could be useful for *in vivo* studies.

3.5 Conclusion

FEM has been a successful tool in the field of bone study using high resolution imaging, which is critically important in identifying trabecular bone quality related

fracture risk. However, limited spatial resolution and partial volume effect of in vivo MDCT imaging are still challenging to FE models. In this work, a segmentation algorithm that reliably identifies trabecular bone and preserve marrow topology is proposed, followed by a mesh generator that produces high quality mesh for FEM analysis. The effectiveness of proposed FEM framework was experimentally validated. The application of FEM has shown the ability of detecting differences of trabecular bone quality. The relation of FEM computed measures and micro-architectural measures was explored. The FEM framework was successful for in vivo MDCT imaging and is probably applicable for future studies.

CHAPTER 4
REGIONAL ANALYSIS USING SHAPE MODELING

Shape model is an effective tool to solve segmentation and registration problems for medical imaging applications [42]. Shape modeling involves many techniques, for example, model construction, shape matching, shape deformation, feature extraction, etc, making it a comprehensive problem. Many of these technical problems are of great diversity. Although there exists various solutions to each problem, individual application places unique requirements that are generally not easy to solve using a specific method. In terms of our application, i.e., segmentation of sub-regions of bone in different anatomic sites, there are several desired properties that inspire the development of shape modeling.

First, the targets have obvious geometric and topological features, because our target shapes are human bones, including proximal femur, distal femur, distal radius, etc, which share similar appearances. They are anatomically meaningful and have correspondence at specific places. Therefore, landmark system is a natural fit for these target shapes, making advantages of these prior information. In addition, if landmarks are able to capture geometric information on these shapes, automatic detection and matching of feature points can accelerate the process and reduce manual work.

The regional segmentation of human bones requires a method that is automatic and reliable. From the landmark system, we can build up a shape model. Shape model has the advantage that once established, it is able to apply onto any new

shape. Unlike other methods, shape model does not allow free deformation, rather is restricts the shape in a subspace that maintains basic information and essential features of the target. Training from a set of shapes, for example, proximal femur bones, the shape model will always produce a valid shape instance which is desirable. In this work, I developed a shape model framework that is robust as well as automatic to achieve the segmentation task. The framework involves several components that ensures the model achieve great performance in the specific application, as well as fit general applications in a broader range.

4.1 Shape Smoothing for Low Resolution MRI Images

In 3D space, $X = \{L_1, L_2, L_3, \cdots, L_n\}$ denotes a vector that contains n landmarks, $L_i = \{(x_i, y_i, z_i)\}$. Given a training set of shapes X_i, a mean shape $\bar{X}$ can be generated using principle component analysis (PCA). The landmark can be defined implicitly using a set of coordinates. However, these landmarks are often drawn on a given surface mesh S, through a graphical user interface. In medical imaging applications, the raw dataset is 3D scan image, represented as I. To construct the landmark system, the first step is to generate surface mesh S from I. The surface mesh generator has been described in Sec 3.2.

Due to the scanning principle of medical equipment, image spacing is not always isotropic in 3D. Often, the slice spacing is much larger than in-plane spacing. The resulting images and derived surface mesh have staircase artifacts, as shown in Fig 4.1. Such artifacts misrepresent the original shape appearance and influence the
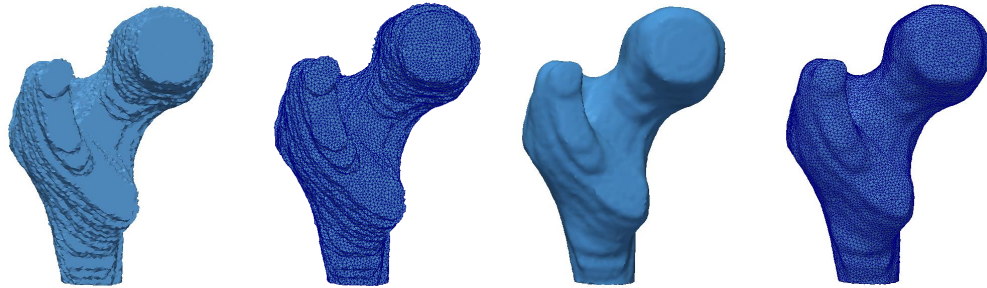
Figure 4.1: (a). Surface mesh generated from a low resolution MRI image. (b). Surface mesh using isotropic distance smoothing.

placing of landmark, and further impact the accuracy of shape model construction. Ever worse, the artifacts will be inherited by the shape model, such that if landmarks are placed on false geometric feature points, the shape model will retain the artifact, making matching the shape model to new shape instances inaccurate.

To reduce the staircase artifact, I introduced an image smoothing scheme using signed distance transform on isotropic grids. The method applies on the digital image I, and it produces a smooth result that satisfies the requirement of landmark placement; see 4.1(b). Although the method does not directly apply on the surface mesh S, I argue that it also works by first doing a grid scanning and the method has advantages that is adaptive to general surface smoothing tasks.

In this work, the shape model to be constructed is human proximal femur. We thus need an isotropic representation. The original binary anisotropic image is first interpolated to isotropic I. Holes or cavities inside the shape body are filled using image closing operator: $I \bullet E_s = (I \oplus E_s) \ominus E_s$. E_s denote a binary structuring

element at a given scale s. Let's denote the foreground object by O, and background by Ω, then $I = O \cup \Omega$.

The smoothing method starts by computation of distance map. Initially, boundary points are identified and their distance values are set to zero. Signed distance transform is computed on both the object and background to get the distance map M, such that $\forall p \in O, M(p) > 0$ and $\forall q \in \Omega, M(q) < 0$.

A smoothing step follows by applying the smoothing kernel Θ to get smoothed image $I^* = f(I) = \Theta * I$. The new boundary is the level set at distance value of zero, $f(I) = 0$. The properties of the smoothing kernel determines the appearance of smoothed image. An isotropic kernel is radial symmetric and rotation invariant. The most common kernel is Gaussian kernel $G(x) = \frac{1}{\sqrt{2\pi}\sigma}e^{-x^2/2\sigma^2}$. Anisotropic kernels takes advantages of directional information and selectively smooth the image in certain direction. In other words, anisotropic kernels are feature-preserving smoothing kernels. As an example, Perona and Malik's anisotropic diffusion [114], $\frac{\partial I}{\partial t} = \mathrm{div}(c(x, y, t)\nabla I)$, works as an anisotropic kernel to facilitate edge-preserving smoothing. The notion of feature-preserving smoothing has been introduced into mesh smoothing [7, 164]. These methods directly apply on the mesh representation instead of digital images. Nevertheless, the advantage of the smoothing scheme here is that the choice of smoothing kernel is more flexible depending on the application and the smoothing result one wants to achieve. In this work, the Gaussian kernel is adopted to reduce the staircase artifacts and the result is promising 4.1.

The proposed method can also be applied to meshes. Given a mesh represen-
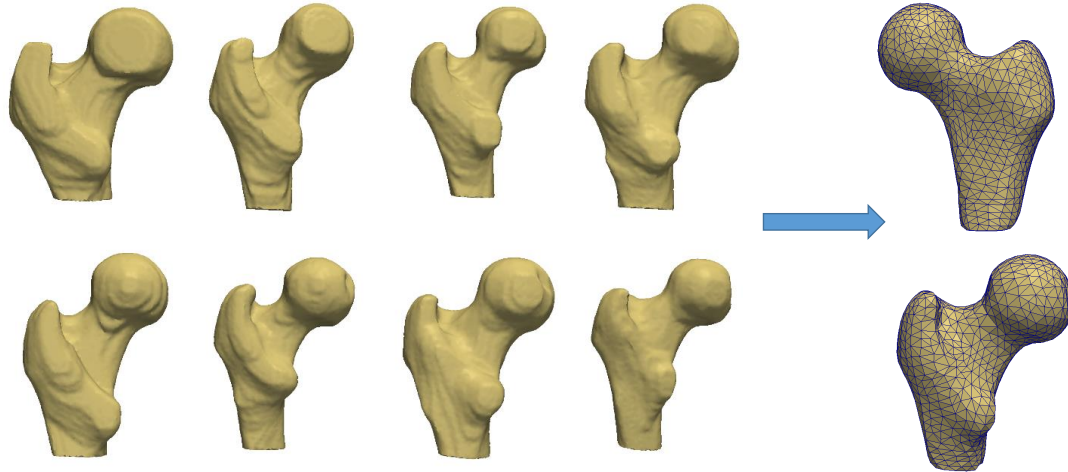
Figure 4.2: Proximal femur shapes from different subjects and the generated mean shape.

tation S of object O, a scanning step, which is often referred to as scan-conversion or voxelization [76], converts the mesh into volume images. In the scan-conversion step, the key is to determine the grid to separate inside and outside of O. A few existing algorithms achieves the voxelization. Some detect the intersection between uniform grid and polygons [67]. Some uses more advanced structures like octree [76]. Once the voxelization is achieved. The mesh smoothing can be converted into the smoothing of digital images. The advantage here is that the smoothing kernel is selective and thus able to handle different requirements of smoothing.

After smoothing, surface shapes of femur subjects are obstained. In the next step, a new landmark system is defined by experts to represent the object shape. Construction of the system will be presented in the following section.
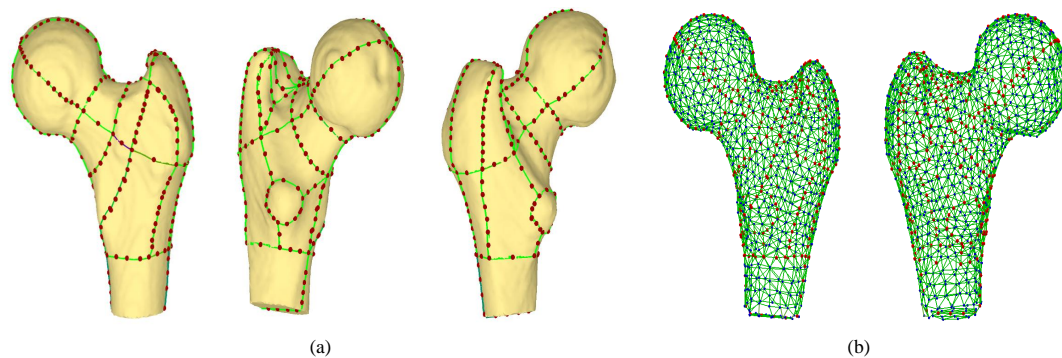
Figure 4.3: Landmark system of human proximal femur. (a) primary landmark (red dots) and landmark lines. (b) Landmark mesh (red dots are primary landmarks and blue dots are innner landmarks).

4.2 Landmark System Construction

The landmark system is a crucial component for mean shape generation. Salient landmarks should capture the geometric features of the given shape surface. They should also be highly reproducible across different subjects. An appropriate number of landmarks are required to represent the shape in a discrete form. These landmarks are considered as a sampling of target shape, and therefore uniformly distributed landmarks are preferred. In this work, the landmark system **L** is generated for the shape model of a given 3D femur shape. The training set is a set of proximal femur subjects.

Landmarks that are of geometric importance and with high reproducibility are referred as primary landmarks. They are generated by experts on each training shape surface using a graphical user interface (GUI). Experts are asked to interactively

place landmark points onto the surface and use corresponding landmark curves as reference to divide the entire surface into subsurface regions, such that each region is homogeneous with regular shape, avoiding significant shape variations, such as large curvature, large protrusion or sharp edges. Figure 4.3 (a) shows primary landmarks, landmark curves and corresponding subsurface regions defined on a training shape. Inside each surface subregion, an inner landmark is added if there exist a salient feature point that must be maintained. With the reference of primary landmarks, additional landmarks are automatically placed in each subregion to achieve a dense distribution. These landmarks are referred as secondary landmarks. By defining primary landmarks to represent geometric features and secondary landmarks to meet a predefined density, we argue that such an approach is a robust and efficient way to construct the landmark system toward an optimal tradeoff.

Establishing the landmark system on each training shape is fulfilled in five sequential steps: (1) Define the primary landmark system; (2) place primary landmarks on individual training shapes; (3) define complete landmark set on one prototype training shape; (4) generate landmark mesh on the prototype shape; (5) warp the complete set of prototype landmarks on each individual training shape using the correspondence of primary landmarks.

primary landmark system: primary landmarks that represent geometric features are determined for human proximal femur by experts. They are reproducible across shapes and are then used to divide the anatomic shape surface into subsurfaces. An example of a primary landmark system on human proximal femur is illustrated

in Fig 4.3 (a).

primary landmarks placement: primary landmarks are drawn by two experts using a GUI following a prototype, which defines the order of landmark curves and several geometric points, that has been defined for human proximal femur. Each user follows the order of landmark curves and places primary landmarks. A third user reviews the landmark and makes corrections if needed.

Complete landmark set on prototype shape: Secondary landmarks are generated to achieve the predefined density only on one prototype training shape. Here secondary landmarks doesn't carry geometric information.

Generate landmark mesh: A surface mesh is generated from the complete set of landmarks $\mathbf{L}$ defined on the prototype shape, using a manifold Delaunay triangulation based on the computation of manifold distance transform. Manifold distance is defined on the surface S. Given two points p, q on $S(V, E)$, where V is surface vertices and E is surface edges, a path π between p and q is the sequential set of edges $(e_1, e_2, \cdots, e_n)$. $N(p)$ is the set of neighbor vertices of p. The length of π, denoted as $\mathcal{L}(\pi)$, is the sum of edge lengths of $(e_1, e_2, \cdots, e_n)$. Let $\mathcal{P}$ denote all paths from p to q. Manifold distance $\mathcal{D}(p, q)$ is therefore represented as

$$\mathcal{D}(p, q) = \min_{\pi \in \mathcal{P}} \mathcal{L}(\pi). \tag{4.1}$$

The manifold distance transform yields a manifold distance map $(\mathbf{M}_{dt})$ and a nearest landmark map $(\mathbf{M}_{lm})$ for all landmarks. The algorithm to compute manifold distance transform is summarized in Algo. 4.1. Using the information of $\mathbf{M}_{lm}$, the landmark mesh $S_{lm} = (\mathbf{L}, E_{lm})$, where $\mathbf{L}$ is the set of landmark, E_{lm} is the set of

edges, is generated following the Algo. 4.2. The generated landmark mesh is shown

in Fig. 4.3 (b).

Algorithm 4.1 Manifold distance transform

Input: $S(V, E), \mathbf{L}$
Output: $\mathbf{M}_{dt}$, $\mathbf{M}_{lm}$
Algorithm:

1. Initialize an empty queue Q
2. **for** all $v \in V$
3. $\mathbf{M}_{dt}(v) = $ MaxValue
4. $\mathbf{M}_{lm}(v) = $ -1
5. **for** all $l \in \mathbf{L}$
6. $\mathbf{M}_{dt}(l) = 0$
7. $\mathbf{M}_{lm}(l) = l$
8.   push l into Q
9. **While** Q is not empty
10.   pop v from Q
11.   **for** all $v' \in N(v)$
12.   **if** $\mathbf{M}_{dt}(v') > \mathbf{M}_{dt}(v) + |vv'|$
13. $\mathbf{M}_{dt}(v') = \mathbf{M}_{dt}(v) + |vv'|$
14. $\mathbf{M}_{lm}(v') = \mathbf{M}_{lm}(v)$
15.   push v' into Q
16. **EndWhile**

Warp landmarks onto individual shape: The complete landmark set defined on the prototype training shape was deformed onto any individual training shape using the correspondence of primary landmarks. The idea is using piecewise deformation such that each surface subregion are transformed from the prototype shape to individual shape, where the correspondence of two subregions is defined by their primary landmarks. Let R denote a subregion on the prototype shape, which contains

---

Algorithm 4.2 Manifold landmark mesh generation

Input: $S(V, E), \mathbf{L}, \mathbf{M}_{lm}$
Output: $S_{lm}(\mathbf{L}, E_{lm})$
Algorithm:

1. Initialize $E_{lm} =$ empty set
2. **for** all $v \in V$
3. $l_1 = \mathbf{M}_{lm}(v)$
4.   **for** all $v' \in N(v)$
5. $l_2 = \mathbf{M}_{lm}(v')$
6.   **if** $l_1 \neq l_2$ and $\overline{l_1 l_2} \notin \min E_{lm}$
7. $E_{lm} = E_{lm} \cup \overline{l_1 l_2}$

---

primary landmarks $p_1, p_2, \cdots, p_n$ and secondary landmarks $s_1, s_2, \cdots, s_m$. R' denotes the subregion on the target shape, with $p'_1, p'_2, \cdots, p'_n$ as primary landmarks. The task is to determine secondary landmarks $s'_1, s'_2, \cdots, s'_m$, on the target shape. The criteria is to minimize the change of landmark mesh after mapping R to R'. A process that simulates the physical deformation of a spring system is adopted. For the landmark mesh, each edge is treated as a spring, and each landmark is a mass node. Primary landmarks of R are gradually moved to R' under an external force, in each iteration of time period Δt. The movement of node will lead to deformation of springs and spring forces tend to maintain the original shape and impede the change. The system will achieve convergence after all springs are balanced. After a few iterations, the whole landmarks are warped to R', and $s'_1, s'_2, \cdots, s'_m$ are placed. An extended deformation system will be described in more details in Sec. 4.5.2.

4.3 Landmark Based Active Shape Model

Following previous sequential steps, the landmark system can be established on every training shape. The active shape model is then generated following the outline by Cootes [42]. The mean as well as variations in an anatomic shape is computed using the Procrustes method [59] and principal component analysis (PCA).

Shape models are a set of objects that have similar shapes and therefore are able to be represented using a generic form of representation. 2D and 3D objects are usually target shapes. In medical imaging, the representation of 3D objects are volumetric imaging data or a mesh representation or a point cloud. Landmarks that capture the outline of the shape are marked on the representation of the object. These landmarks are generally geometric features and important points that maintain the topology and connectivity. In 3D space, let $\mathbf{X} = \{L_1, L_2, L_3, \cdots, L_n\}$ denote a vector that contains n landmarks, $L_i = \{(x_i, y_i, z_i) \mid x_i, y_i, z_i \in R^3\}$. Given a training set of shapes $\mathbf{X}_i$, a mean shape $\bar{\mathbf{X}}$ can be generated using PCA and the family of shape model is represented as

$$\mathbf{X} = \bar{\mathbf{X}} + \mathbf{Pb} \tag{4.2}$$

where $\mathbf{P} = \{p_1, p_2, \cdots, p_m\}$ is the m dimensional eigenvectors and $\mathbf{b}$ is a m dimensional vector. To generate the mean shape using PCA, first one computes the mean of all training data,

$$\bar{\mathbf{X}} = \frac{1}{n} \sum_{i=1}^{n} \mathbf{X}_i \tag{4.3}$$

and the covariance,

$$\mathcal{V} = \frac{1}{n-1}\sum_{i=1}^{n}(\mathbf{X}_i - \bar{\mathbf{X}})(\mathbf{X}_i - \bar{\mathbf{X}})^T \tag{4.4}$$

Eigenvectors p_i and corresponding eigenvalues λ_i are computed and sorted $(\lambda_i \geq \lambda_{i+1})$. The total variance is computed as $V_x = \sum \lambda_i$. For the sake of model simplicity, we reduce the dimensions of the shape model. The first m eigenvalues are selected and smaller eigenvalues are truncated such that

$$\sum_{i=1}^{m}\lambda_i > rV_x \tag{4.5}$$

where r is the ratio that the model explains, for instance, $r = 0.95$.

Following the above steps, a mean shape $\bar{\mathbf{X}}$ will be generated from a set of training shapes $\mathbf{X}_i$. The eigenvalues λ_i represent the shape information and govern the change of shape appearance. By controlling the shape descriptive vector $\mathbf{b}$, one can generate a family of shapes that is analogous to the mean shape.

4.4   Automatic Shape Matching

Shape models solve segmentation and registration problems for a set of objects that have similar shapes. Once the shape model is constructed, the goal is to find a shape deformation procedure to match the shape model to the target object. The advantage of shape model is its adaptability from the shape model to other objects based on shape deformation. The deformation process is called shape matching or shape registration. However, the shape matching has been a challenging part for 3D modeling. Establishing the correspondence between the mean shape and target shapes and the matching criteria largely influence the quality of shape modeling. In

some applications of medical imaging, manual registration is used to match source and target shapes [135] using graphical user interface. In some other applications, since target objects all have similar shapes and the variability between objects is small, shape model is capable to provide reliable and accurate registration results. In this study, I proposed a new scheme for shape matching. The matching process consists of two steps. In the first step, an automatic initial shape alignment is achieved using feature point matching. Secondly, an iterative shape matching step based on the shape model accomplishes the shape registration. Successful shape matching reduces tedious and time-consuming expert works for identification of salient anatomic features on each object, making it automatic and much easier to define region of interests that are clinically concerned.

Shape matching algorithm automatically computes correspondences between the involved shapes. Given the reference shape X and a target shape $\tilde{X}$, shape matching is to find the deformation $D : X \to \tilde{X}$. In this study, we assume the deformation of femur bone shape is affine transform. Let $\phi(s, t, \theta)$ denote the affine transform, s is scale factor, t is translation and θ is rotation angle. The optimum affine transformation minimizes the error metrics between the reference shape and the target shape. In addition to the affine transform, we consider the generic shape deformation of active shape model restricted by its eigenvectors and eigenvalues. Rather than arbitrary shape deformation, eigenvalues and eigenvectors preserve the shape model and guide the deformation. Let $\delta(\mathbf{b}, m)$ denote the deformation parameter, $\mathbf{b}$ is corresponding control parameters, m is the dimension. Now the deformation is written

as $D_{\delta,\phi} : X \to \tilde{X}$. And the shape matching is formalized as a joint optimization problem

$$D = \arg\min_{\delta,\phi}|X - \tilde{X}|_2 \tag{4.6}$$

In 3D space, the Euclidean distance is often used as the error metric ϵ, to represent the similarity of shapes. The error metric $\epsilon = |X - \tilde{X}|_2$ can be written as the sum of closest distances from points on the reference shape to the target shape.

In a simple situation, where the reference shape X and the target shape have the same number of landmarks and the landmark correspondence has been established, there exists a close form solution to find the best affine transform that aligns reference and target shapes [42]. Let H_s denote the surface of target shape, x_i is a point on the reference shape. The affine transform $\phi(s, t, \theta)$ maps x_i to the closest point $\tilde{x}_i$ on the target shape surface H_s. Then we rewrite the optimization as

$$D = \arg\min_{\delta} \sum_{i=0}^{n}|X - \phi^{-1}(H_s, x_i)|_2. \tag{4.7}$$

This method utilizes landmark correspondence to achieve shape matching. However, in most applications, numbers of landmarks of reference and target shapes differ. And the prior knowledge of established correspondence of landmarks is not available or needs manual identification. In this study, our goal is to automatically generate landmark system defined in Sec. 4.2, through shape matching. Here, the reference shape is the mean shape, $X = \bar{X} + P\mathbf{b}$, generated in Sec. **??**. The target shape $\tilde{X}$ is a surface mesh representation of any given femur subject. A shape matching method based on feature points extraction and matching is presented in following paragraphs.

4.4.1   Feature Points Extraction

Feature points extraction of target shape dates back to 2D digital images. Harris corner detector introduces the earliest feature points identification in 2D images [63]. More advanced feature points were proposed to maintain invariant properties of images, such as rotation, scaling, by incorporating local descriptive features. Therefore, these feature points are suitable to be used as anchor points to match a few images that share the same scene but with different filming conditions like angle and illumination. The most widely known invariant feature point extraction in 2D images is the SIFT feature detector [104]. Inspired by the success of descriptive features in 2D images, feature descriptors that extract salient points from a surface mesh also made great progress. Several researchers extended 2D image descriptors into mesh. Harris 3D [154] extends Harris corner detector into 3D meshes. Mesh-SIFT [44] borrows the notion of SIFT and has achieved scale invariance in feature detection in 3D meshes. Several methods uses the differences of Gaussians (DOG), which is also a classical method in 2D image processing, as feature detector [181, 86]. These methods enables us to capture important features of the shape that can be used for shape registration.

In this work, I adopted a feature point extraction method based on the canonical heat diffusion process on a shape. The method, called Heat Kernel Signature (HKS) [161], captures global information of the geometry of the shape, and renders a feature map based on the geometric importance of each point. HKS models a heat diffusion process on a Riemannian manifold. Heat dissipates over time in the neighborhood of a point on the manifold. The scale information is intrinsically incor-

porated in the diffusion time. The heat propagation on the shape is governed by the heat diffusion equation,

$$(\nabla_X + \frac{\partial}{\partial_t})u = 0 \tag{4.8}$$

where, ∇_X represents the positive semi-definite Laplace-Beltrami operator. The solution $u(x, t)$, denoted as heat kernel $_t(x, y)$, describes the amount of heat at point x on time t, with initial condition $u(x, 0) = \delta(x - y)$. For compact manifolds, the heat kernel has the following eigendecomposition:

$$k_t(x, y) = \sum_{i=0}^{\infty} e^{-\lambda_i t}\psi_i(x)\psi_i(y) \tag{4.9}$$

where λ_i is ith eigenvalue and $\psi_i(x)$, $\psi_i(y)$ are corresponding eigenvectors of ∇_X.

The heat kernel signature proposed in [161] is written as

$$h = k_t(x, x) = \sum_{i=0}^{\infty} e^{-\lambda_i t}\psi_i^2(x) \tag{4.10}$$

and further improved to scale invariance to the input shape X by taking the logarithm of h, and then shifting the phase after discrete-time Fourier transform [21]. Finally, scale-invariant heat kernel signature (SI-HKS) was obtained to describe feature of any point on the shape X.

SI-HKS has several advantages that satisfy feature point extraction in our study. To begin with, it is scale-invariant to shape size. Often, the reference and target shapes are of different size. Usually, scale normalization is an necessary step to convert matching shapes to the same scale. However, in this study, the mean shape consists of only n landmarks (Fig. 4.3) and the target shape is a dense mesh with m

vertices (Fig. 4.1) ($m \gg n$). The common normalization would fail due to different number of vertices.

SI-HKS captures essential geometric features of the shape, with less spurious feature points. Unlike other feature point detectors that depend on local descriptive measures, SI-HKS conveys the global information. Therefore, feature points identified by SI-HKS are robust to local shape variances. In this study, human femur shapes have various appearances and some subjects may even suffer from osteoporosis or osteophyte which alternate local appearances of shape. As a result, local descriptive feature detectors are likely to highlight such abnormal regions and lead to failure of shape matching from the normal healthy shape to the abnormal target. SI-HKS detects salient features in a larger neighborhood when the time period is appropriately set.

4.4.2 Automatic Matching Algorithm

The flow chart of shape deformation. The workflow of automatic shape matching consists of five sequential steps as shown in Fig. **??**: (1) mesh decimation of target shape, (2) feature points extraction, (3) feature points clustering, (4) shape alignment, (5) shape model matching.

Mesh decimation. Initially, the target shape mesh is decimated to approximate the number of vertices of the reference mesh, or the mean shape. Let's denote the mean shape by $X = \bar{X} + \mathbf{P}\mathbf{b}$, $\mathbf{b} = 0$, with n vertices (each vertex is also the landmark, refer to the mesh generation of mean shape in Sec. 4.2). The target shape

is a dense triangular mesh Y with m $(m \gg n)$. A decimate rate $r = 1 - n/m$, is approximately applied on Y to generate a new mesh Y′ with m' vertices. The principle of decimation [144] is maintaining mesh topology, without splitting or deletion of boundaries. Therefore, the geometric features of the original mesh are kept. With the topology constraint, the yield mesh Y′ may not have the exact same number of vertices as X. Duplicate points should be removed in a post-processing step.

Feature points extraction. After mesh decimation, SI-HKS computes the feature value map on mesh X and Y′. A large time scale is used to avoid local extrema as discussed in above paragraphs. An example showing the computed feature map is presented in Fig. 4.4. SI-HKS captures salient points that represent salient features of the shape. It can be observed in the figure that a large number of feature points often concentrate in a few regions with salient geometric features, such as the femur head, where the surface is of uniform importance of notice, and the protrusion at the great trochanter, where the surface curvatures change rapidly. The mesh decimation ensures the mean shape X and target shape Y have similar number of vertices. Therefore, salient points also distribute similarly in each salient regions.

Feature points clustering. The first N salient points are identified based on the feature value. They are clustered into C centers, using the K-means method. The clustering center is shown in Fig 4.4. In this work, $N = 300$ and $C = 6$ has been chosen determined by experiments of on the training dataset of femur subjects. The location of clustering centers matches well with anatomic feature points of proximal femur, covering the femoral head, the great trochanter, and the lesser trochanter.
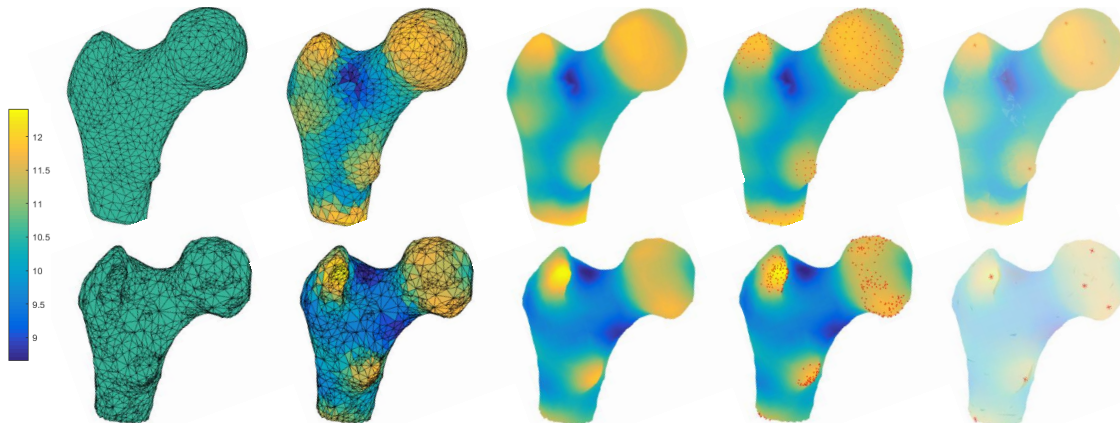
Figure 4.4: Automatic feature point extraction on human femur shapes using scale-invariant heat kernel signature. From left to right of each row, each shape represents: mesh of a sample femur subject; feature value overlay on the mesh using scale-invariant heat kernel signature; smoothed feature map; first 300 important points extracted from the feature map; clustering centers of feature points. The first row represents the mean shape. The second row shows an example of another femur subject. The color bar is shown on the left.

Clustering centers, center of gravity on the mean shape and the target shape are denoted as c_i, c_g and $\tilde{c}_i$, $\tilde{c}_g$ respectively. Generally, distances from several salient points to the center of gravity of proximal femur have certain order. For example, the distance from the point at great trochanter to the center of gravity is larger than that of the point at lesser trochanter. Our extracted clustering centers correspond to specific anatomic points, and thus can be ordered based on the distance to the center of gravity. c_is and $\tilde{c}_i$s are sorted in order of distance $dist_i = \|c_i - c_g\|$, and paired $\{c_i, \tilde{c}_i\}$.

Shape alignment. Affine transform τ is computed from the paired centers $\{c_i,\ \tilde{c}_i\}$ and then used to approximately align the mean shape X onto the target shape $\tilde{X}$. In implementation, $\tilde{X}$ is projected on to the mean shape frame using τ^{-1}. The classical iterative closest point (ICP) algorithm refines the shape alignment by minimizing the cost of Euclidean distance. Let φ represent the transform obtained by ICP, then the optimal transform from shape model to the target shape is $\phi = \varphi(\tau)$. Notably, although the ICP algorithm is able to minimize the distance between two point clouds, and could be used to register two shapes, it fails without the initial affine transform τ. Without the shape alignment determined by matching clustering centers $\{c_i,\ \tilde{c}_i\}$, the ICP algorithm would converge to a local minimum, resulting in mismatch between mean and target shape, due to differences of coordinate system between mean shape and target shape, as well as the large variety of human proximal femur subjects; see some examples of femur subjects in Fig. 4.2. The feature point extraction and clustering take advantages of the geometric information of the femur shape and make the alignment reliable and robust.

Shape model matching. Shape alignment finds the optimal transform mapping the target shape on to the coordinate system of the mean shape. Still, the mean and target shape are only partially overlapped. The next task is to matching the mean shape to the target such that finally these two shapes are close to identical. In other words, the differences between mean and target shape after shape alignment are unique features of the target. We can find the best fit to the target shape features using the active shape model. The shape model, represented as $X = \bar{X} + \mathbf{Pb}$, is a

generalization of shape instances in a high dimensional feature space Θ, determined by the training models. Finding the best fit to the target shape is to find the best projection of the shape model in the subspace constrained by the eigensystem and the control parameter $\mathbf{b}$. $\delta(\mathbf{b}, m)$ denotes the critical parameter; m is the dimension of subspace. The optimization process is to solve

$$D = \arg\min_{\delta}|X - \phi^{-1}(\tilde{X})|_2, \tag{4.11}$$

where ϕ is the transform found in shape alignment step.

Inspired by the work of Cootes [42], I developed an iteratively algorithm to solve the problem. In each iteration, the method contains two steps. In the first step, we generate and modify a shape instance by allowing it deforming freely in the high dimensional space Θ. The shape instance is an approximation of the target shape. Let X_i' denote the shape instance in current ith iteration, $X_{i-1} = \bar{X} + \mathbf{P}\mathbf{b}_{i-1}$ denote the actual shape generated by the active shape model in i-1 th iteration, where $\mathbf{b}_0 = 0$, when $i = 1$ and $X_0 = \bar{X}$ is the mean shape. In each iteration, X_{i-1} and target shape $\tilde{X}$ are first aligned, such that the scale, pose are matched. X_i' is generated by minimizing cost function $\epsilon = |\tilde{X} - X_{i-1}|_2$. For the first iteration, X_0 and $\tilde{X}$ are already aligned by affine transform ϕ. In future iterations, the ICP algorithm is used to optimize the pose and rotation of $\tilde{X}$ to align with X_{i-1}.

In the second step, the shape instance is projected onto the subspace constrained by the shape model. At ith iteration, X_i' is obtained by sampling $\tilde{X}$. Then features of the target shape are approximated by the differences between X_i' and X_{i-1}, represented as $f = X_i' - X_{i-1}$. The residual of parameter $\Delta\mathbf{b}_i$ is computed by

generalizing the active shape model.

$$f = X_i' - X_{i-1} = \mathbf{P}\Delta\mathbf{b}_i, \tag{4.12}$$

$$\Delta\mathbf{b}_i = \mathbf{P}^{-1}(X_i' - X_{i-1}) \tag{4.13}$$

Then the shape parameter and actual shape are updated:

$$\mathbf{b}_i = \mathbf{b}_{i-1} + \Delta b_i, \tag{4.14}$$

$$X_i = \bar{X} + \mathbf{P}\mathbf{b}_i. \tag{4.15}$$

Let $d = |X_i - X_{i-1}|_2$ measures the change of generated shape between adjacent iterations. The iterative process terminates when ϵ is smaller than the predefined threshold γ_ϵ, or d is sufficient small (less than γ_d), or i is larger than maximum number of iterations (i_{max}). The process is guaranteed to converge in finite number of iterations because the error metric d decreases in each iteration. The iterative process can be summarized in Algo. 4.3.

Following the active shape model matching algorithm, the final shape X is generated as a close approximation to the target shape. X is governed by the eigensystem that has shown to cover 98% features of femur subjects, with much fewer dimension m. The landmark system $\{L_i\}, i = 1, 2, \cdots, m$ of the shape model have been successfully deployed onto the target shape. Now vertex v_i of X corresponds to landmark L_i in the landmark system.

In summary, given any femur shape, the automatic shape matching algorithm generates a shape instance from the active shape model. The shape instance, which

---

Algorithm 4.3 Iterative shape model matching

Input: $\tilde{X}, \bar{X}, P, \tau, \phi, \gamma_\epsilon, \gamma_d, i_{max}$
Output: $\mathbf{b}, X$
Algorithm:

1. $i = 1, \mathbf{b}_0 = 0, X_0 = \bar{X}$
2. **While** $i < i_{max}$ and $(d > \gamma_d$ or $\epsilon > \gamma_\epsilon)$
3.   Apply affine transform τ on $\tilde{X}$ to match the coordinate system of X_{i-1}.
4.   Minimize $|X_{i-1} - \tau^{-1}(\tilde{X})|_2$ using ICP algorithm and get the transform φ.
5.   Sampling $\tilde{X}$ by finding closest points from X_{i-1} to $\varphi^{-1}(\tau^{-1}(\tilde{X}))$ and get X_i'.
6.   Compute:
7. $\Delta\mathbf{b}_i = \mathbf{P}^{-1}(X_i' - X_{i-1})$
8. $\mathbf{b}_i = \mathbf{b}_{i-1} + \Delta\mathbf{b}_i$
9. $X_i = \bar{X} + \mathbf{P}\mathbf{b}_i$
10. $\epsilon = |\varphi^{-1}(\tau^{-1}(\tilde{X})) - X_i|_2$
11. $d = |X_i - X_{i-1}|_2$
12. $i = i + 1$
13. **EndWhile**
14. $\mathbf{b} = \mathbf{b}_i, X = X_i$

---

contains m landmarks, is a close approximation to the target femur shape. Each landmark of the shape instance locates on the target shape. The correspondence of landmarks is established. Therefore, the landmark system has been established on the target femur shape.

4.5   Volume Shape Deformation

Clinically, different anatomic sites indicate distinct properties of bone metrics, for example, BMD and trabecular microarchitecture [60]. Automatic segmentation of subregions of the target volume is a challenging task. In this work, I proposed a shape model based framework to solve the problem. As discussed in previous sections, the shape model with a landmark system has been constructed to describe

the shape. Here, the active shape model and the landmark system are rooted on the surface of the shape. Given any femur shape, the algorithm is able to achieve accurate registration of the shape model and target shape, and deploy the surface landmark system onto the target shape. Nevertheless, to subdivide the target volume into demand regions that are ready for clinical studies, for example, trabecular bone micro-architectural analysis, we need to define the volume landmark system. The system contains a few landmarks and landmark connection information. On the mean shape, each landmark has been classified into one of the subregions and has a unique label. A volume shape deformation algorithm is used to transform the landmark system defined on the mean shape onto the target shape. The process is similar to the surface landmark deformation. Once the deformation is successfully achieved, the subregion segmentation can be achieved with the information of volume landmarks. Here, the whole process contains two major components: construction of the volume landmark system and automatic shape deformation.

4.5.1   Volume Landmark System

Volume landmark system is a structure similar to the surface landmark system described in previous sections. The construction of volume landmark was developed based on the requirements of the study. The ultimate goal is to achieve regional segmentation on a 3D digital image I. In other words, for any pixel $p \in I$, we need to classify and assign a label $l(p)$ to p. The transformation of the grid pixel p between the structured grid (Z^3) is an interpolation process using landmarks defined in the

Figure 4.5: Volume mesh of the mean shape.

unstructured 3D volume (R^3). Uniform distributed landmarks are preferred in terms

of interpolation. The number of volume landmarks are generated with the average

distance of adjacent landmarks less or approximately equal to the average distance

of surface landmarks. In this way, the number of volume landmarks are controlled

to reduce the computational complexity. The system also records the connection

of volume landmarks. We can represent the system with a volume mesh V, with

landmarks $\{V_j\}, j = 1, 2, \cdots, N$.

First, the system is generated as a volume mesh with quasi-uniform points

inside the surface of generated shape instance X from active shape model. Surface

landmarks $\{L_i\}$ are naturally a subset of the volume landmarks. For volume mesh construction, Delaunay-refinement-based methods generates tetrahedron elements by inserting points to enforce tetrahedra satisfying constraints on size and quality, as well as maintaining a Delaunay or constrained Delaunay triangulation [150]. In addition, these methods produce volume mesh with surface exactly the same as the input. By inserting "steiner points", we can generate quasi-uniform points with the average edge length similar to the grid size. In this work, the volume mesh is generated using Tetgen [151], a quality volume mesh generator. An example of the volume mesh is shown in Fig. 4.5.

After the construction of the volume mesh V, a labeling process $L : V_j \rightarrow r$ is applied to each landmark V_j, where r is the set of subregions $r_1, r_2, \cdots, r_k$. (Mathematical representation of the volume landmark system somewhere?)

4.5.2   Automatic Deformation Algorithm

For a group of similar shapes, one can deform one shape instance to another, such that the reference shape overlaps with the target. The goal of deformation is that the information of the reference shape is carried during the deformation. Finally the deformed shape is able to deploy the carried information on the overlapped target. Specifically, in this work, I developed an automatic shape deformation algorithm to deploy the landmark system onto any given volume shape. With the information of landmark labels, subregions of the shape can therefore be defined.

The deformation from reference to the target shape requires a matching cri-

teria between the two shapes. In previous sections, the complete volume landmark system has been constructed on the mean shape, and we already have the surface landmark system deployed onto the target shape using automatic shape matching. The correspondence of surface landmarks on the reference and target shape is therefore established. The criteria that guides the deformation process contains two components: (1) matching corresponding surface landmarks and (2) minimizing a function that measures volume differences between the reference and target shapes.

Volume landmark meshes are denoted as $O = \{V, G\}$ and $O' = \{V', G'\}$, for the mean shape and the target shape, respectively. $V = \{L, B\}$ represents the vertices of mean shape, where L, B are surface landmarks and inner volume landmarks. $G = \{G_s, G_t\}$ represents the connected graph of vertices, where G_s, G_t are then triangles of surface landmarks and tetrahedra of inner volume landmarks. The deformation process is then obtained by solving the following minimization problem:

$$\min_{V} \left(\sum_{i=1}^{n} |L - L'|_2 + \alpha \, g(B, B') \right), \tag{4.16}$$

where the function $g(B, B')$ measures the criteria of volume difference, and α is a constant balancing the two components.

In this work, volume landmarks inside the surface are generated uniformly. The uniform system has several advantages. First, volume landmarks are finally used for interpolation and determine labels of regions. Uniform landmarks are stable and reliable for interpolation. Second, the uniform system avoids tetrahedron with extreme elements that could cause violation of topology during mesh deformation. The deformation process should keep as much information for the reference shape, and

thus the uniformity of volume landmarks should not be damaged during deformation. I therefore define a similarity measure to constrain the deformation process using the function:

$$g(B, B') = \sum_{i=1}^{m} |T_i - T_i'|,$$ (4.17)

where T_i represents the volume of the ith tetrahedron. And the minimization problem is re-written as:

$$\min_{V} \left(\sum_{i=1}^{n} |L - L'|_2 + \alpha \sum_{i=1}^{m} |T_i - T_i'| \right).$$ (4.18)

In this application, the femur shape can be modeled as a solid material with elastic springs connecting all landmarks V. The whole shape is treated as an deformable shape and initially springs are at a stable stage with forces balanced. The deformation process can be thought as the reference shape being driven by an external force F_s that matches surface landmarks L on to L'. Under the driven force F_s, the shape will change and the elastic system reacts to the change such that inner springs deform and finally reach stable. According to physics law, spring force is along the spring when it is compressed or stretched. We can write the force as:

$$F_s = k_s * \frac{\Delta l}{l_{orig}}$$ (4.19)

where k_s is a constant, Δl is the difference of spring length, l_{orig} is the original length of the spring. (more description about the spring) Also, during the deformation process, the constrain that maintains the uniformity of tetrahedral volumes, can be modeled as reaction force F_v. Similar to the definition of spring force, I define the reaction force F_v with respect to the difference of volume. The direction of F_v is

along the movement direction of the barycenter of one tetrahedron. We can write the equation as:

$$F_v = k_v * \frac{\Delta v}{v_{orig}} \tag{4.20}$$

where k_v is a constant, Δv is the difference of tetrahedral volume, v_{orig} is the original volume of the tetrahedron.

The volume mesh deformation process is an iterative process that simulates the physical behavior of the elastic system. The duration of each iteration is a predefined constant Δt. At any time/iteration t during the deformation process, a force $F_s(L, t)$ is applied on the surface landmarks of the shape model to gradually move L_i toward L_i' and is defined as a constant force along the vector $L_i - L_i'$. In one iteration, L_i moves Δt closer to L_i'. Δt is small such otherwise the system can not stabilize. After a few iterations, L_i may get very close to L_i', while oscillate around L_i' due to the dynamics of the elastic system. The oscillation around the target point L_i' is avoided by forcing L_i to move to L_i' at the end of iteration when they become sufficiently close.

In each iteration, the movement of L_i leads to compression or stretch of springs. Spring forces gradually move inner volume landmarks B_i to achieve the next stabilization. All springs (edges) adjacent to B_i contribute spring forces for displacement. The total force is computed and applied on B_i such that it is moved from e_i to e_i'. Due to the change of volume, the constraint force F_v reacts to slow the change of original volume. It then moves B_i to a balanced point e_i''. B_i is thus guided under F_s and F_v where a balance is achieved. B_i moves freely inside the volume as long as the

displacement satisfies topology constraints: no collision, self-intersection, or cavity. Specifically, the vector $e_i'' - e_i$ are not allowed to collide on to other landmarks or triangles. If collision is detected, the movement of B_i will be marked as illegal and discarded. Similar to surface landmarks, if a volume landmark oscillates around a point, the cumulated force in the latest l iterations are computed to determine the position of the oscillated landmark. The movement of inner landmarks finally reach stabilization.

The deformation process stops when all surface landmarks L_i on the shaped model have been successfully deformed to corresponding landmarks L_i'. Through the elastic deformation, the reference and target shape maximumly overlapped and a uniformly distributed volume landmark system has been deployed on the target shape.

4.6   Regional Segmentation

After volume shape deformation, a complete landmark system on the target shape has been established. The uniformly distributed landmarks are samples of the three dimensional space R^3. The transform in R^3 could then be approximated by corresponding landmarks V and V'. For each grid pixel $p \in Z^3$ of the target image that we want to segment, we first find its k nearest neighbor landmarks $V_1'(p), V_2'(p), \cdots, V_k'(p)$. Corresponding landmarks $V_1(p), V_2(p), \cdots, V_k(p)$ are determined on the mean shape. A transform $\Omega_p(V, V')$ is computed using corresponding landmarks. The label of p is determined as the label of the transformed grid pixel

on the mean shape. For this application, femur shapes are known as smooth surfaces and of limited degree of freedom in variation. We therefore choose the thin plate spline (TPS) as the transform to imply a penalty involving the smoothness of the fitted surface.

The above method demands a labeled image of the mean shape; let's denote it as prototype labeled image $\bar{G} \in Z^3$. We generate the labeled image following strategies described below. Let $\Omega(V_j, \bar{V}) : R^3 \to R^3$ denote the transform from the coordinate system of any given shape to the coordinate of the mean shape, where V_j and $\bar{V}$ are volume landmarks of training shape j and mean shape. $\bar{G}$ is generated using TPS transform from a set of ground truth images where subregions are manually labeled by experts (Fig. 4.7), represented as $G_1, G_2, \cdots, G_k$. Following the automatic shape matching and volume deformation step described in previous sections, the complete landmark system of the mean shape ($\bar{V}$) is deployed onto G_j and the corresponding landmark system V_j are obtained. TPS transform $\Omega(V_j, \bar{V})$ maps G_j to G'_j, the labeled image in the coordinate space of the mean shape. The average of I'_j is used to decide the label for each pixel $p \in \bar{G}$. Finally, the prototype segmented image $\bar{G}$ which corresponds to the mean shape $\bar{\mathbf{X}}$ is constructed.

The regional segmentation of any digital femur image I^* are achieved following the proposed pipeline. The complete work flow can be summarized as: (1) smooth the original digital image I^*, and generate a surface mesh S^* from smoothed image; (2) extract feature points from decimated mesh of S^* using SI-HKS, align S^* to mean shape using clustered centers of feature points; (3) generalize mean shape to match S^*

and place surface landmarks on S^*; (4) deform mean shape volume landmark system to S^* using corresponding surface landmarks and get volume landmarks V^* for S^*; (5) compute $\Omega(V, V^*)$ and apply it to $\bar{G}$ to get final regional segmented image G^*.

4.7   Experiment

The aim of our experimental plan is to assess the methods ability to subdivide the proximal femur into predefined subregions.

MR Imaging

The femur MRI was collected at New York University [30]. The right proximal femur of each subject was scanned on a 7 T whole body MR scanner (Siemens Medical Solutions, Erlangen, Germany) using a quadrature knee coil (18 cm diameter, transmit-receive). A high-resolution 3D-fast low angle shot (FLASH) sequence was employed to obtain all images (TR/TE = 20/4.5; flip angle 10°; bandwidth 130 Hz/pixel; one signal acquired; 130 axial images with resolution 0.242 mm × 0.242 mm × 1.50 mm). Scanning time was ~12 min total.

Subjects

MRI bone data of thirty human subjects were recruited in the Department of Radiology at New York University. Each subject was scanned twice within the same day with repositioning between scans.

Manual segmentation

For the training phase, the trabecular bone region outline was manually segmented for each image slice. A example of MRI proximal femur image is shown in

Fig. 4.7(a), manual segmented tarbecular bone region overlaid on the proximal femur bone is shown in Fig. 4.7(b).

Inside the trabecular region, subregions are defined by expert users to subdivide the proximal femur into femoral head, femoral neck, great trochanter, lesser trochanter, inter trochanter, etc, following the guidance proposed for clinical research. Figure 4.7(c) shows an example of manual segmented subregions, where each color represents one subregion.

4.8   Results

A mean shape and corresponding active shape model has been generated using thirty training shapes with manually drawn surface landmarks. The ability of generalizing the shape model to match individual shapes was tested using leave-one-out strategy, to maximumly make use of training samples. Average error per landmark is approximate 7 pixels of the image size. Eigenvalues that represent main information of shape variability were calculated and shown in Fig. 4.6(a). The coverage rate which is the ratio of cumulated eigenvalues to the sum of all eigenvalues is shown in Fig. 4.6(b). Twenty-two eigenvalues were required to achieve 0.95 coverage rate.

The mean shape was constructed and the prototype labeled image was generated using average of transformed manual labeled images. Given a new image with trabecular ROI, our shape model was able to subdivide it into subregions. One example is illustrated in Fig. 4.7(d). The overall accuracy of subregions were found 0.80 $\pm$ 0.08.
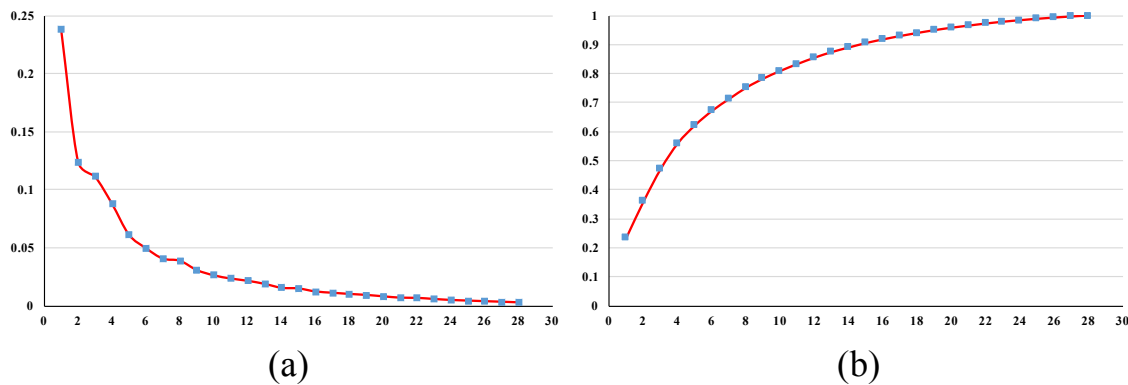
Figure 4.6: (a). Eigenvalues of active shape model. (b). Coverage rate of active shape model computed as ratio of cumulated eigenvalues to the sum of all eigenvalues.

4.9   Conclusion

Shape model is an effective tool to solve segmentation and registration problems for medical imaging applications. In this work, a shape model based framework has been constructed to achieve the purpose of subdividing proximal femur trabecular bone region into predefined subregions. The framework solves the segmentation problem of 3D digital images by transforming from digital lattice grid to the space of volume shape. A new landmark system and an active shape model were built to aid establishing the correspondence between shape model and individual shape instance. Generated uniform and dense volume landmarks establishes the transform that maps the segmented mean shape image to the target image. Finally the subregion segmentation is achieved.
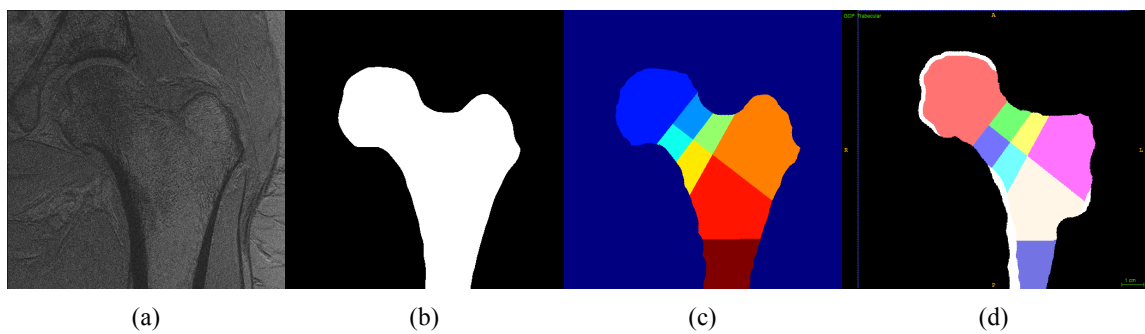
Figure 4.7: (a). A example slice of human proximal femur from an MRI image. (b). Manual segmented trabecular bone ROI. (c). Manual labeled subregions. (d). An example showing the overlay of segmented subregions using our method over the original ROI.

CHAPTER 5
CONCLUSION

Osteoporosis is a bone disease associated with an increased risk of low trauma fractures that entails massive medical costs. Osteoporosis is clinically defined by low bone mineral density (BMD), which explains 65-75% of the variance in bone stiffness. The remaining variability is due to the cumulative and synergistic effects of various factors, including trabecular bone micro-architecture. Effective measures of TB micro-architecture are useful to assess bone strength and fracture risk in the realm of clinical therapy and treatment guidance. The advance of high resolution imaging provides a tool for understanding of trabecular bone micro-architecture and its properties.

Quantitative assessment of trabecular bone has drawn great research interests and applications of quantitative methods are the main stream in the field of bone research. In this work, volumetric imaging algorithms, named Volumetric Topological Analysis (VTA) and Tensor Scale (TS), were applied on *in vivo* imaging to measure the quality of trabecular bone micro-architecture. These methods offer reproducible measures of TB plate/rod micro-architecture at in vivo MRI, and were experimentally demonstrated suitable for cross-sectional and follow-up studies toward answering clinical and biological questions, under limited spatial resolution. The morphologic interpretations of our measures are well defined, and histologic evidence confirms the relationship between osteoporosis and the gradual conversion of trabecular plates to rods, a process well known to increase fracture risk.

We have shown the effectiveness of two state-of-the-art scanners, in terms of accuracy and reproducibility of our micro-architectural measures as well as their ability to predict actual bone strength. The bone measures derived from the two scanners with notably different spatial resolution features were found of high correlation. It revealed that a longitudinal study can jump scanners and still maintain longitudinal continuity. Therefore keeping data uniformity in large-scale or multi-site or longitudinal studies is feasible.

We constructed a finite element model (FEM) to quantitatively assess bone strength by in vivo MDCT imaging. New segmentation algorithms that reliably identifies trabecular bone and preserve marrow topology were proposed to overcome limited spatial resolution and partial volume effect. The effectiveness of proposed FEM was experimentally validated. The application of FEM has shown the ability of detecting differences of trabecular bone quality on different in vivo human groups. The relation of FEM computed measures and micro-architectural measures was explored.

In osteoporosis, bone structure decreases systematically which leads to loss of bone mass and deterioration of micro-architecture. However, the severity of bone loss and deterioration were different in various anatomic sites in human body. A shape model based segmentation algorithm was developed to subdivide human proximal femur into predefined subregions, which helps to further understand trabecular properties in different regions. The method solves the segmentation problem of 3D digital images by transforming from digital lattice grid to the space of volume shape. A new landmark system and an active shape model were built to aid establishing

the correspondence between shape model and individual shape instance. Generated uniform and dense volume landmarks establishes the mapping between the segmented mean shape image and the target image. The model achieved automatic subregional segmentation of proximal femur and provided a general solver for subregional segmentation for other shapes.

In summary, this work has made contributions to understanding trabecular bone micro-structures using quantitative imaging measures at in vivo imaging. Various studies, including cadeveric and in vivo groups, have shown that these quantitative measures are capable to assess quality of bone and predict the fracture risk. Therefore, it is of high potential to help prevent osteoporosis and guide the treatment clinically.

CHAPTER 6
FUTURE WORK

Digital and volumetric imaging algorithms have been proved effective to quantitatively measure trabecular bone micro-structure. However, there are rooms for improvement. Current algorithms, i.e., volumetric topological analysis (VTA) and tensor scale (TS) depends on the skeleton representation. More accurate skeleton algorithms could improve the accuracy of these two methods. In terms of clinical researches, the full potential of these methods needs to be evaluated in other imaging modalities.

We successfully constructed FEM for in vivo MDCT imaging. However, the segmentation is still a great impact factor due to the fact that the complex topology of trabecular bone network highly affects FEM results. The FEM demands more accurate segmentation algorithm that correctly preserve the completeness of trabecular network under limited spatial resolution. In addition, current linear FE model could be improved to non-linear with unisotropic materia properties.

Subregion segmentation consists of a few technical components, each of which can still be optimized. For example, we may introduce automatic feature point extraction algorithms to identify salient surface landmarks in the training phase, which could reduces large amount of manual work. The automatic shape matching method could also be improved with more robust identification of feature points on target shapes. In this work, it is optimized for proximal femur, but in more general cases, a robust and efficient approach is required. The deformation of volume landmarks is

possible to be improved by adding a regularization term that constrains the process, or we can speed up the deformation process.

The future research direction is combining imaging and FEM based methods, and applies on different anatomic sites determined by the subregional segmentation method. It is interesting to investigate the properties of trabecular bone network and understand its behaviors. In the future, with more advanced imaging tools, quantitative methods may become more accurate and robust to measure the quality of bone from different aspects.

REFERENCES

[1] Pierre Alliez, David Cohen-Steiner, Mariette Yvinec, and Mathieu Desbrun. Variational tetrahedral meshing. In *ACM Transactions on Graphics (TOG)*, volume 24, pages 617–625. ACM, 2005.

[2] C. Arcelli and Gabriella Sanniti di Baja. A width-independent fast thinning algorithm. *IEEE Trans Patt Anal Mach Intell*, 7(4):463–474, 1985.

[3] C. Arcelli and Gabriella Sanniti di Baja. Finding local maxima in a pseudo-euclidean distance transform. *Comp Vis Graph Imag Proc*, 43:361–367, 1988.

[4] C. Arcelli, Gabriella Sanniti di Baja, and L. Serino. Distance-driven skeletonization in voxel images. *IEEE Trans Patt Anal Mach Intell*, 33(4):709–720, 2011.

[5] Robert M Aris, Peter A Merkel, Laura K Bachrach, Drucy S Borowitz, Micheal P Boyle, Sarah L Elkin, Theresa A Guise, Dana S Hardin, Charles S Haworth, Michael F Holick, et al. Guide to bone health and disease in cystic fibrosis. *The Journal of Clinical Endocrinology & Metabolism*, 90(3):1888–1896, 2005.

[6] Daniel T Baran, Michele A Bergfeld, Steven L Teitelbaum, and Louis V Avioli. Effect of testosterone therapy on bone formation in an osteoporotic hypogonadal male. *Calcified tissue research*, 26(1):103–106, 1978.

[7] Y Belyaev and H Seidel. Mesh smoothing by adaptive and anisotropic gaussian filter applied to mesh normals. In *Vision, modeling, and visualization*, pages 203–210, 2002.

[8] Maria Benito, Bryon Gomberg, Felix W Wehrli, Richard H Weening, Babette Zemel, Alexander C Wright, Hee Kwon Song, Andrew Cucchiara, and Peter J Snyder. Deterioration of trabecular architecture in hypogonadal men. *The Journal of Clinical Endocrinology & Metabolism*, 88(4):1497–1502, 2003.

[9] Maria Benito, Branimir Vasilic, Felix W Wehrli, Benjamin Bunker, Michael Wald, Bryon Gomberg, Alexander C Wright, Babette Zemel, Andrew Cucchiara, and Peter J Snyder. Effect of testosterone replacement on trabecular architecture in hypogonadal men. *Journal of Bone and Mineral Research*, 20(10):1785–1791, 2005.

[10] Marshall Bern, David Eppstein, and John Gilbert. Provably good mesh generation. In *Foundations of Computer Science, 1990. Proceedings., 31st Annual Symposium on*, pages 231–241. IEEE, 1990.

[11] Jacobo Bielak, Omar Ghattas, and E Kim. Parallel octree-based finite element method for large-scale earthquake ground motion simulation. *Computer Modeling in Engineering and Sciences*, 10(2):99, 2005.

[12] Dennis M Black, Pierre D Delmas, Richard Eastell, Ian R Reid, Steven Boonen, Jane A Cauley, Felicia Cosman, Péter Lakatos, Ping Chung Leung, Zulema Man, et al. Once-yearly zoledronic acid for treatment of postmenopausal osteoporosis. *New England Journal of Medicine*, 356(18):1809–1822, 2007.

[13] Steven W Blume and Jeffrey R Curtis. Medical costs of osteoporosis in the elderly medicare population. *Osteoporosis International*, 22(6):1835–1844, 2011.

[14] Jean-Daniel Boissonnat and Steve Oudot. Provably good sampling and meshing of surfaces. *Graphical Models*, 67(5):405–451, 2005.

[15] G. Borgefors. Distance transform in arbitrary dimensions. *Comp Vis Graph Imag Proc*, 27:321–345, 1984.

[16] G. Borgefors. Distance transformations in digital images. *Comp Vis Graph Imag Proc*, 34:344–371, 1986.

[17] Stephanie Boutroy, Mary L Bouxsein, Francoise Munoz, and Pierre D Delmas. In vivo assessment of trabecular bone microarchitecture by high-resolution peripheral quantitative computed tomography. *The Journal of Clinical Endocrinology & Metabolism*, 90(12):6508–6515, 2005.

[18] Stephanie Boutroy, Bert Van Rietbergen, Elisabeth Sornay-Rendu, Francoise Munoz, Mary L Bouxsein, and Pierre D Delmas. Finite element analysis based on in vivo hr-pqct images of the distal radius is associated with wrist fracture in postmenopausal women. *Journal of Bone and Mineral Research*, 23(3):392–399, 2008.

[19] Mary L Bouxsein, Stephen K Boyd, Blaine A Christiansen, Robert E Guldberg, Karl J Jepsen, and Ralph Müller. Guidelines for assessment of bone microstructure in rodents using micro–computed tomography. *Journal of bone and mineral research*, 25(7):1468–1486, 2010.

[20] Steven K Boyd. Site-specific variation of bone micro-architecture in the distal radius and tibia. *Journal of Clinical Densitometry*, 11(3):424–430, 2008.

[21] Michael M Bronstein and Iasonas Kokkinos. Scale-invariant heat kernel signatures for non-rigid shape recognition. In *Computer Vision and Pattern Recognition (CVPR), 2010 IEEE Conference on*, pages 1704–1711. IEEE, 2010.

[22] Andrew J Burghardt, Galateia J Kazakia, and Sharmila Majumdar. A local adaptive threshold strategy for high resolution peripheral quantitative computed tomography of trabecular bone. *Annal Biomed Eng*, 35(10):1678–1686, 2007.

[23] Andrew J Burghardt, Thomas M Link, and Sharmila Majumdar. High-resolution computed tomography for clinical imaging of bone microarchitecture. *Clinical Orthopaedics and Related Research®*, 469(8):2179–2193, 2011.

[24] Andrew J Burghardt, Jean-Baptiste Pialat, Galateia J Kazakia, Stephanie Boutroy, Klaus Engelke, Janina M Patsch, Alexander Valentinitsch, Danmei Liu, Eva Szabo, Cesar E Bogado, et al. Multicenter precision of cortical and trabecular bone quality measures assessed by high-resolution peripheral quantitative computed tomography. *Journal of Bone and Mineral Research*, 28(3):524–536, 2013.

[25] M Burrows, D Liu, and H McKay. High-resolution peripheral qct imaging of bone micro-structure in adolescents. *Osteoporosis international*, 21(3):515–520, 2010.

[26] J Canny. A computational approach to edge detection. *IEE Trans. Pat. Anal. Mach. Intel.*, (6):679–698, 1986.

[27] Jane A Cauley, Frances L Lucas, Lewis H Kuller, Katie Stone, Warren Browner, and Steven R Cummings. Elevated serum estradiol and testosterone concentrations are associated with a high risk for breast cancer. *Annals of internal medicine*, 130(4_Part_1):270–277, 1999.

[28] Gregory Chang, Stephen Honig, Yinxiao Liu, Cheng Chen, Kevin K Chu, Chamith S Rajapakse, Kenneth Egol, Ding Xia, Punam K Saha, and Ravinder R Regatte. 7 tesla mri of bone microarchitecture discriminates between women without and with fragility fractures who do not differ by bone mineral density. *Journal of bone and mineral metabolism*, 33(3):285–293, 2015.

[29] Gregory Chang, S Kubilay Pakin, Mark E Schweitzer, Punam K Saha, and Ravinder R Regatte. Adaptations in trabecular bone microarchitecture in olympic athletes determined by 7t mri. *Journal of Magnetic Resonance Imaging*, 27(5):1089–1095, 2008.

[30] Gregory Chang, Ligong Wang, Guoyuan Liang, James S Babb, Punam K Saha, and Ravinder R Regatte. Reproducibility of subregional trabecular bone micro-architectural measures derived from 7-tesla magnetic resonance images. *Magnetic Resonance Materials in Physics, Biology and Medicine*, 24(3):121–125, 2011.

[31] Gregory Chang, Ding Xia, Cheng Chen, Guillaume Madelin, Steven B Abramson, James S Babb, Punam K Saha, and Ravinder R Regatte. 7t mri detects deterioration in subchondral bone microarchitecture in subjects with mild knee osteoarthritis as compared with healthy controls. *Journal of Magnetic Resonance Imaging*, 41(5):1311–1317, 2015.

[32] Cheng Chen, Ryan E Amelon, Anneliese Heiner, and Punam K Saha. Assessment of trabecular bone strength at in vivo ct imaging with space-variant hysteresis and finite element modelling. In *Biomedical Imaging (ISBI), 2016 IEEE 13th International Symposium on*, pages 872–875. IEEE, 2016.

[33] Cheng Chen, Dakai Jin, Yinxiao Liu, Felix W Wehrli, Gregory Chang, Peter J Snyder, Ravinder R Regatte, and Punam K Saha. Volumetric topological analysis on in vivo trabecular bone magnetic resonance imaging. In *Advances in Visual Computing*, pages 501–510. Springer, 2014.

[34] Cheng Chen, Dakai Jin, Yinxiao Liu, Felix W Wehrli, Gregory Chang, Peter J Snyder, Ravinder R Regatte, and Punam K Saha. Trabecular bone characterization on the continuum of plates and rods using in vivo mr imaging and volumetric topological analysis. *Physics in Medicine and Biology*, 61(18):N478, 2016.

[35] Cheng Chen, Dakai Jin, and Punam K Saha. Fuzzy skeletonization improves the performance of characterizing trabecular bone micro-architecture. In *International Symposium on Visual Computing*, pages 14–24. Springer, 2015.

[36] Siu-Wing Cheng, Tamal K Dey, Herbert Edelsbrunner, Michael A Facello, and Shang-Hua Teng. Silver exudation. *Journal of the ACM (JACM)*, 47(5):883–904, 2000.

[37] Siu-Wing Cheng, Tamal K Dey, and Jonathan Shewchuk. *Delaunay mesh generation*. CRC Press, 2012.

[38] Charles H Chesnut, Sharmilla Majumdar, David C Newitt, Andrew Shields, Jan Van Pelt, Ellen Laschansky, Moise Azria, Audrey Kriegman, Melvin Olson, Erik F Eriksen, et al. Effects of salmon calcitonin on trabecular microarchitecture as determined by magnetic resonance imaging: results from the quest study. *Journal of bone and mineral research*, 20(9):1548–1561, 2005.

[39] L Paul Chew. Guaranteed-quality delaunay meshing in 3d (short version). In *Proceedings of the thirteenth annual symposium on Computational geometry*, pages 391–393. ACM, 1997.

[40] Krzysztof Chris Ciesielski, Jayaram K Udupa, Punam K Saha, and Ying Zhuge. Iterative relative fuzzy connectedness for multiple objects with multiple seeds. *Computer Vision and Image Understanding*, 107(3):160–182, 2007.

[41] Campion Cooper, G Campion, and LJ Melton Iii. Hip fractures in the elderly: a world-wide projection. *Osteoporosis international*, 2(6):285–289, 1992.

[42] Tim Cootes, E Baldock, and J Graham. An introduction to active shape models. *Image processing and analysis*, pages 223–248, 2000.

[43] Steven R Cummings, Stephen Eckert, Kathryn A Krueger, Deborah Grady, Trevor J Powles, Jane A Cauley, Larry Norton, Thomas Nickelsen, Nina H Bjarnason, Monica Morrow, et al. The effect of raloxifene on risk of breast cancer in postmenopausal women: results from the more randomized trial. *Jama*, 281(23):2189–2197, 1999.

[44] Tal Darom and Yosi Keller. Scale-invariant features for 3-d mesh models. *IEEE Transactions on Image Processing*, 21(5):2758–2769, 2012.

[45] Crawford Doran, Athena Chang, and Robert Bridson. Isosurface stuffing improved: acute lattices and feature matching. In *ACM SIGGRAPH 2013 Talks*, page 38. ACM, 2013.

[46] A. S. Issever et al. Trabecular bone structure analysis in the osteoporotic spine using a clinical in vivo setup for 64-slice MDCT imaging: Comparison to μCT imaging and μFE modeling. *J. Bone Min. Res.*, 24(9):1628–1637, 2009.

[47] J. S. Bauer et al. Prediction of bone strength by μCT and MDCT-based finite-element-models: How much spatial resolution is needed? *Euro. J. Rad.*, 83(1):e36–e42, 2014.

[48] S. V. N. Jaecques et al. Individualised, micro CT-based finite element modelling as a tool for biomechanical analysis related to tissue engineering of bone. *Biomat.*, 25(9):1683–1696, 2004.

[49] T. Ju et al. Dual contouring of hermite data. *ACM Trans. Graph.*, 21(3):339–346, 2002.

[50] X. H. Zhang et al. In vivo μMRI-based finite element and morphological analyses of tibial trabecular bone in eugonadal and hypogonadal men before and after testosterone treatment. *J. Bone Min. Res.*, 23(9):1426–1434, 2008.

[51] Lee A Feldkamp, Steven A Goldstein, Michael A Parfitt, Gerald Jesion, and Michael Kleerekoper. The direct examination of three-dimensional bone architecture in vitro by computed tomography. *Journal of bone and mineral research*, 4(1):3–11, 1989.

[52] Thomas Flohr, K Stierstorfer, R Raupach, S Ulzheimer, and H Bruder. Performance evaluation of a 64-slice ct system with z-flying focal spot. In *RöFo-Fortschritte auf dem Gebiet der Röntgenstrahlen und der bildgebenden Verfahren*, volume 176, pages 1803–1810. © Georg Thieme Verlag KG Stuttgart· New York, 2004.

[53] R Mm Francis, Munro Peacock, JE Aaron, PL Selby, GA Taylor, J Thompson, DH Marshall, and A Horsman. Osteoporosis in hypogonadal men: role of decreased plasma 1, 25-dihydroxyvitamin d, calcium malabsorption, and low bone formation. *Bone*, 7(4):261–268, 1986.

[54] Alejandro F Frangi, Wiro J Niessen, Koen L Vincken, and Max A Viergever. Multiscale vessel enhancement filtering. In *Med Imag Comput Comput-Assist Inter (MICCAI)*, pages 130–137. Springer, 1998.

[55] HK Genant, K Engelke, and S Prevrhal. Advanced ct bone imaging in osteoporosis. *Rheumatology*, 47(suppl 4):iv9–iv16, 2008.

[56] HK Genant, C Gordon, Y Jiang, TF Lang, TM Link, and S Majumdar. Advanced imaging of bone macro and micro structure. *Bone*, 25(1):149–152, 1999.

[57] BR Gomberg, FW Wehrli, B Vasilić, RH Weening, PK Saha, HK Song, and AC Wright. Reproducibility and error sources of μ-mri-based trabecular bone structural parameters of the distal radius and tibia. *Bone*, 35(1):266–276, 2004.

[58] Bryon R Gomberg, Punam K Saha, Hee Kwon Song, Scott N Hwang, and Felix W Wehrli. Topological analysis of trabecular bone mr images. *IEEE Transactions on Medical Imaging*, 19(3):166–174, 2000.

[59] Colin Goodall. Procrustes methods in the statistical analysis of shape. *Journal of the Royal Statistical Society. Series B (Methodological)*, pages 285–339, 1991.

[60] Lindsay M Griffin, Stephen Honig, Cheng Chen, Punam K Saha, Ravinder Regatte, and Gregory Chang. 7t mri of distal radius trabecular bone microarchitecture: How trabecular bone quality varies depending on distance from end-of-bone. *Journal of Magnetic Resonance Imaging*, 2016.

[61] Junfeng Guo, Chao Wang, Kung-Sik Chan, Dakai Jin, Punam K Saha, Jered P Sieren, RG Barr, MeiLan K Han, Ella Kazerooni, Christopher B Cooper, et al. A controlled statistical study to assess measurement variability as a function of test object position and configuration for automated surveillance in a multi-center longitudinal copd study (spiromics). *Medical physics*, 43(5):2598–2610, 2016.

[62] M Hahn, M Vogel, M Pompesius-Kempa, and G Delling. Trabecular bone pattern factora new parameter for simple quantification of bone microarchitecture. *Bone*, 13(4):327–330, 1992.

[63] Chris Harris and Mike Stephens. A combined corner and edge detector. In *Alvey vision conference*, volume 15, page 50. Citeseer, 1988.

[64] Tor Hildebrand, Andres Laib, Ralph Müller, Jan Dequeker, and Peter Rüegsegger. Direct three-dimensional morphometric analysis of human cancellous bone: microstructural data from spine, femur, iliac crest, and calcaneus. *Journal of bone and mineral research*, 14(7):1167–1174, 1999.

[65] TOR Hildebrand and PETER RÜEGSEGGER. Quantification of bone microarchitecture with the structure model index. *Computer Methods in Biomechanics and Bio Medical Engineering*, 1(1):15–23, 1997.

[66] Alexandra Hotca, Chamith S Rajapakse, Chen Cheng, Stephen Honig, Kenneth Egol, Ravinder R Regatte, Punam K Saha, and Gregory Chang. In vivo measurement reproducibility of femoral neck microarchitectural parameters derived from 3t mr images. *Journal of Magnetic Resonance Imaging*, 42(5):1339–1345, 2015.

[67] Jian Huang, Roni Yagel, Vassily Filippov, and Yair Kurzion. An accurate method for voxelizing polygon meshes. In *Volume Visualization, 1998. IEEE Symposium on*, pages 119–126. IEEE, 1998.

[68] SVN Jaecques, Hans Van Oosterwyck, Luiza Muraru, Tim Van Cleynenbreugel, Els De Smet, Martine Wevers, Ignace Naert, and Jos Vander Sloten. Individualised, micro ct-based finite element modelling as a tool for biomechanical analysis related to tissue engineering of bone. *Biomaterials*, 25(9):1683–1696, 2004.

[69] D. Jin and P. K. Saha. A new fuzzy skeletonization algorithm and its applications to medical imaging. In *Proc of 17th Int Conf Image Anal Proc (ICIAP)*, volume LNCS 8156, pages 662–671, Naples, Italy, 2013.

[70] Dakai Jin, Cheng Chen, and Punam K Saha. Filtering non-significant quench points using collision impact in grassfire propagation. In *International Conference on Image Analysis and Processing*, pages 432–443. Springer, 2015.

[71] Dakai Jin, Junfeng Guo, Timothy M Dougherty, Krishna S Iyer, Eric A Hoffman, and Punam K Saha. A semi-automatic framework of measuring pulmonary arterial metrics at anatomic airway locations using ct imaging. In *SPIE Medical Imaging*, pages 978816–978816. International Society for Optics and Photonics, 2016.

[72] Dakai Jin, Krishna S Iyer, Cheng Chen, Eric A Hoffman, and Punam K Saha. A robust and efficient curve skeletonization algorithm for tree-like objects using minimum cost paths. *Pattern Recognition Letters*, 2015.

[73] Dakai Jin, Krishna S Iyer, Eric A Hoffman, and Punam K Saha. Automated assessment of pulmonary arterial morphology in multi-row detector ct imaging using correspondence with anatomic airway branches. In *International Symposium on Visual Computing*, pages 521–530. Springer, 2014.

[74] Dakai Jin, Krishna S Iyer, Eric A Hoffman, and Punam K Saha. A new approach of arc skeletonization for tree-like objects using minimum cost path. In *Proceedings of the... IAPR International Conference on Pattern Recognition/sponsored by the International Association for Pattern Recognition in cooperation with the IEEE Computer Society...[et al]. International Conference on Patt.*, volume 2014, page 942. NIH Public Access, 2014.

[75] Dakai Jin, Yinxiao Liu, and Punam K Saha. Application of fuzzy skeletonization ot quantitatively assess trabecular bone micro-architecture. In *2013 35th Annual International Conference of the IEEE Engineering in Medicine and Biology Society (EMBC)*, pages 3682–3685. IEEE, 2013.

[76] Tao Ju. Robust repair of polygonal models. *ACM Transactions on Graphics (TOG)*, 23(3):888–895, 2004.

[77] Galateia J Kazakia, Benedict Hyun, Andrew J Burghardt, Roland Krug, David C Newitt, Anne E de Papp, Thomas M Link, and Sharmila Majumdar. In vivo determination of bone structure in postmenopausal women: a comparison of hr-pqct and high-field mr imaging. *Journal of Bone and Mineral Research*, 23(4):463–474, 2008.

[78] Tony M Keaveny, Robert E Borchers, Lorna J Gibson, and Wilson C Hayes. Trabecular bone modulus and strength can depend on specimen geometry. *Journal of Biomechanics*, 26(8):991–1000, 1993.

[79] Tony M Keaveny, Elise F Morgan, Glen L Niebur, and Oscar C Yeh. Biomechanics of trabecular bone. *Annual review of biomedical engineering*, 3(1):307–333, 2001.

[80] Sundeep Khosla, B Lawrence Riggs, Elizabeth J Atkinson, Ann L Oberg, Lisa J McDaniel, Margaret Holets, James M Peterson, and L Joseph Melton. Effects of sex and age on bone microstructure at the ultradistal radius: a population-based noninvasive in vivo assessment. *Journal of Bone and Mineral Research*, 21(1):124–131, 2006.

[81] M Kleerekoper, AR Villanueva, J Stanciu, D Sudhaker Rao, and AM Parfitt. The role of three-dimensional trabecular microstructure in the pathogenesis of vertebral compression fractures. *Calc Tis Int*, 37(6):594–597, 1985.

[82] Anne Klibanski, Lucile Adams-Campbell, Tamsen L Bassford, Steven N Blair, Scott D Boden, Kay Dickersin, David R Gifford, Lou Glasse, Steven R Goldring, Keith Hruska, et al. Osteoporosis prevention, diagnosis, and therapy. *Journal of the American Medical Association*, 285(6):785–795, 2001.

[83] R. Krug, A. J. Burghardt, S. Majumdar, and T. M. Link. High-resolution imaging techniques for the assessment of osteoporosis. *Radiol Clin North Am*, 48(3):601–21, 2010.

[84] François Labelle and Jonathan Richard Shewchuk. Isosurface stuffing: fast tetrahedral meshes with good dihedral angles. In *ACM Transactions on Graphics (TOG)*, volume 26, page 57. ACM, 2007.

[85] Shing Chun Benny Lam, Michael J Wald, Chamith S Rajapakse, Yinxiao Liu, Punam K Saha, and Felix W Wehrli. Performance of the mri-based virtual bone biopsy in the distal radius: serial reproducibility and reliability of structural and mechanical parameters in women representative of osteoporosis study populations. *Bone*, 49(4):895–903, 2011.

[86] Chang Ha Lee, Amitabh Varshney, and David W Jacobs. Mesh saliency. In *ACM transactions on graphics (TOG)*, volume 24, pages 659–666. ACM, 2005.

[87] Erick Legrand, Daniel Chappard, Christian Pascaretti, Marc Duquenne, Stéphanie Krebs, Vincent Rohmer, Michel-Félix Basle, and Maurice Audran. Trabecular bone microarchitecture, bone mineral density, and vertebral fractures in male osteoporosis. *Journal of Bone and Mineral Research*, 15(1):13–19, 2000.

[88] Cheng Li, Dakai Jin, Trudy L Burns, James C Torner, Steven M Levy, and Punam K Saha. A new algorithm for cortical bone segmentation with its validation and applications to in vivo imaging. In *International Conference on Image Analysis and Processing*, pages 349–358. Springer, 2013.

[89] Cheng Li, Dakai Jin, Cheng Chen, Elena M Letuchy, Kathleen F Janz, Trudy L Burns, James C Torner, Steven M Levy, and Punam K Saha. Automated cortical bone segmentation for multirow-detector ct imaging with validation and application to human studies. *Medical physics*, 42(8):4553–4565, 2015.

[90] Cheng Li, Dakai Jin, Elena Letuchy, Trudy Burns, Kathleen Janz, James Torner, Steven Levy, and Punam K Saha. In vivo characterization of cortical bone at distal tibia using multi-detector ct imaging-validation and results of application in healthy young adults. In *JOURNAL OF BONE AND MINERAL RESEARCH*, volume 28. WILEY-BLACKWELL 111 RIVER ST, HOBOKEN 07030-5774, NJ USA, 2013.

[91] T. M. Link and S. Majumdar. Osteoporosis imaging. *Radiol Clin North Am*, 41(4):813–39, 2003.

[92] Thomas M Link. Osteoporosis imaging: state of the art and advanced imaging. *Radiology*, 263(1):3–17, 2012.

[93] Thomas M Link and Sharmila Majumdar. Osteoporosis imaging. *Radiologic Clinics of North America*, 41(4):813–839, 2003.

[94] Thomas M Link, Sharmila Majumdar, Peter Augat, John C Lin, David Newitt, Ying Lu, Nancy E Lane, and Harry K Genant. In vivo high resolution mri of the calcaneus: differences in trabecular structure in osteoporosis patients. *Journal of Bone and Mineral Research*, 13(7):1175–1182, 1998.

[95] Thomas M Link, Volker Vieth, Christoph Stehling, Albrecht Lotter, Ambros Beer, David Newitt, and Sharmila Majumdar. High-resolution mri vs multislice spiral ct: which technique depicts the trabecular bone structure best? *European radiology*, 13(4):663–671, 2003.

[96] X Sherry Liu, Adi Cohen, Elizabeth Shane, Perry T Yin, Emily M Stein, Halley Rogers, Shannon L Kokolus, Donald J McMahon, Joan M Lappe, Robert R Recker, et al. Bone density, geometry, microstructure, and stiffness: Relationships between peripheral and central skeletal sites assessed by dxa, hr-pqct, and cqct in premenopausal women. *Journal of bone and mineral research*, 25(10):2229–2238, 2010.

[97] X Sherry Liu, Paul Sajda, Punam K Saha, Felix W Wehrli, Grant Bevill, Tony M Keaveny, and X Edward Guo. Complete volumetric decomposition of individual trabecular plates and rods and its morphological correlations with anisotropic elastic moduli in human trabecular bone. *Journal of Bone and Mineral Research*, 23(2):223–235, 2008.

[98] X Sherry Liu, Emily M Stein, Bin Zhou, Chiyuan A Zhang, Thomas L Nickolas, Adi Cohen, Valerie Thomas, Donald J McMahon, Felicia Cosman, Jeri Nieves, et al. Individual trabecula segmentation (its)-based morphological analyses and microfinite element analysis of hr-pqct images discriminate postmenopausal fragility fractures independent of dxa measurements. *Journal of Bone and Mineral Research*, 27(2):263–272, 2012.

[99] Xiaowei S Liu, Paul Sajda, Punam K Saha, Felix W Wehrli, and X Edward Guo. Quantification of the roles of trabecular microarchitecture and trabecular type in determining the elastic modulus of human trabecular bone. *Journal of Bone and Mineral Research*, 21(10):1608–1617, 2006.

[100] Yinxiao Liu, Dakai Jin, Cheng Li, Kathleen F Janz, Trudy L Burns, James C Torner, Steven M Levy, and Punam K Saha. A robust algorithm for thickness computation at low resolution and its application to in vivo trabecular bone ct imaging. *IEEE Transactions on Biomedical Engineering*, 61(7):2057–2069, 2014.

[101] Yinxiao Liu, Dakai Jin, and Punam K Saha. A new algorithm for trabecular bone thickness computation at low resolution achieved under in vivo condition. In *2013 IEEE 10th International Symposium on Biomedical Imaging*, pages 390–393. IEEE, 2013.

[102] Melton LJIII. How many women have osteoporosis now. *J Bone Miner Res1995*, 10:175–7, 1995.

[103] William E Lorensen and Harvey E Cline. Marching cubes: A high resolution 3d surface construction algorithm. In *ACM siggraph computer graphics*, volume 21, pages 163–169. ACM, 1987.

[104] David G Lowe. Distinctive image features from scale-invariant keypoints. *International journal of computer vision*, 60(2):91–110, 2004.

[105] Joshua A MacNeil and Steven K Boyd. Bone strength at the distal radius can be estimated from high-resolution peripheral quantitative computed tomography and the finite element method. *Bone*, 42(6):1203–1213, 2008.

[106] S Majumdar, HK Genant, S Grampp, DC Newitt, V-H Truong, JC Lin, and A Mathur. Correlation of trabecular bone structure with age, bone mineral density, and osteoporotic status: in vivo studies in the distal radius using high resolution magnetic resonance imaging. *Journal of Bone and Mineral Research*, 12(1):111–118, 1997.

[107] S Majumdar, D Newitt, A Mathur, D Osman, A Gies, E Chiu, J Lotz, J Kinney, and H Genant. Magnetic resonance imaging of trabecular bone structure in the distal radius: relationship with x-ray tomographic microscopy and biomechanics. *Osteoporosis international*, 6(5):376–385, 1996.

[108] Sharmila Majumdar. Magnetic resonance imaging of trabecular bone structure. *Topics in Magnetic Resonance Imaging*, 13(5):323–334, 2002.

[109] L Joseph Melton III et al. Epidemiology of fractures. *Osteoporosis: etiology, diagnosis, and management*, pages 133–154, 1988.

[110] Scott A Mitchell and Stephen A Vavasis. Quality mesh generation in three dimensions. In *Proceedings of the eighth annual symposium on Computational geometry*, pages 212–221. ACM, 1992.

[111] N. Otsu. A threshold selection methods from grey-level histograms. *IEEE Trans Patt Anal Mach Intel*, 9:62–66, 1979.

[112] A Michael Parfitt, Marc K Drezner, Francis H Glorieux, John A Kanis, Hartmut Malluche, Pierre J Meunier, Susan M Ott, and Robert R Recker. Bone histomorphometry: standardization of nomenclature, symbols, and units: report of the asbmr histomorphometry nomenclature committee. *Journal of bone and mineral research*, 2(6):595–610, 1987.

[113] AM Parfitt, CH Mathews, AR Villanueva, M Kleerekoper, B Frame, and DS Rao. Relationships between surface, volume, and thickness of iliac trabecular bone in aging and in osteoporosis. implications for the microanatomic and cellular mechanisms of bone loss. *Journal of clinical investigation*, 72(4):1396, 1983.

[114] Pietro Perona and Jitendra Malik. Scale-space and edge detection using anisotropic diffusion. *IEEE Trans Patt Anal Mach Intel*, 12(7):629–639, 1990.

[115] Martin Petersilka, Herbert Bruder, Bernhard Krauss, Karl Stierstorfer, and Thomas G Flohr. Technical principles of dual source ct. *European journal of radiology*, 68(3):362–368, 2008.

[116] Chamith S Rajapakse, Mary B Leonard, Yusuf A Bhagat, Wenli Sun, Jeremy F Magland, and Felix W Wehrli. Micro-MR imaging-based computational biomechanics demonstrates reduction in cortical and trabecular bone strength after renal transplantation. *Radiology*, 262(3):912–920, 2012.

[117] Chamith S Rajapakse, Jeremy F Magland, and Felix W Wehrli. Fast prospective registration of in vivo mr images of trabecular bone microstructure in longitudinal studies. *Magnetic resonance in medicine*, 59(5):1120–1126, 2008.

[118] R. R. Recker. Architecture and vertebral fracture. *Calc Tiss Int*, 53 Suppl 1:S139–142, 1993.

[119] B. L. Riggs, S. Khosla, and 3rd Melton, L. J. Better tools for assessing osteoporosis. *J Clin Invest*, 122(12):4323–4, 2012.

[120] B Lawrence Riggs, L Joseph Melton, Richard A Robb, Jon J Camp, Elizabeth J Atkinson, James M Peterson, Peggy A Rouleau, Cynthia H McCollough, Mary L Bouxsein, and Sundeep Khosla. Population-based study of age and sex differences in bone volumetric density, size, geometry, and structure at different skeletal sites. *Journal of Bone and Mineral Research*, 19(12):1945–1954, 2004.

[121] P. K. Saha. Tensor scale: a local morphometric parameter with applications to computer vision and image processing. *Computer Vision and Image Understanding*, 99:384–413, 2005.

[122] P. K. Saha, G. Borgefors, and G. Sanniti di Baja. A survey on skeletonization algorithms and their applications. *Pattern Recognition Letters*, 76:3–12, 2016.

[123] P. K. Saha and B. B. Chaudhuri. Detection of 3-D simple points for topology preserving transformations with application to thinning. *IEEE Transactions on Pattern Analysis and Machine Intelligence*, 16:1028–1032, 1994.

[124] P. K. Saha and B. B. Chaudhuri. 3D digital topology under binary transformation with applications. *Comp Vis Imag Und*, 63:418–429, 1996.

[125] P. K. Saha, B. R. Gomberg, and F. W. Wehrli. Three-dimensional digital topological characterization of cancellous bone architecture. *Int J Imag Sys Tech*, 11:81–90, 2000.

[126] P. K. Saha, R. Strand, and G. Borgefors. Digital topology and geometry in medical imaging: A survey. *IEEE Trans Med Imaging*, 34(9):1940–64, 2015.

[127] P. K. Saha and J. K. Udupa. Optimum image thresholding via class uncertainty and region homogeneity. *Pattern Analysis and Machine Intelligence, IEEE Transactions on*, 23(7):689–706, 2001.

[128] P. K. Saha, J. K. Udupa, and D. Odhner. Scale-based fuzzy connected image segmentation: Theory, algorithms, and validation. *Comp Vis Imag Und*, 77:145–174, 2000.

[129] P. K. Saha and F. W. Wehrli. Measurement of trabecular bone thickness in the limited resolution regime of in vivo MRI by fuzzy distance transform. *IEEE Trans Med Imag*, 23:53–62, 2004.

[130] P. K. Saha, F. W. Wehrli, and B. R. Gomberg. Fuzzy distance transform: Theory, algorithms, and applications. *Comp Vis Imag Und*, 86:171–190, 2002.

[131] Punam K Saha and Bidyut Baran Chaudhuri. 3d digital topology under binary transformation with applications. *Computer vision and image understanding*, 63(3):418–429, 1996.

[132] Punam K Saha, Bidyut Baran Chaudhuri, Bhabatosh Chanda, and D Dutta Majumder. Topology preservation in 3d digital space. *Pattern Recognition*, 27(2):295–300, 1994.

[133] Punam K Saha, Bidyut Baran Chaudhuri, and D Dutta Majumder. A new shape preserving parallel thinning algorithm for 3d digital images. *Pattern Recognition*, 30(12):1939–1955, 1997.

[134] Punam K Saha, Bryon R Gomberg, and Felix W Wehrli. Three-dimensional digital topological characterization of cancellous bone architecture. *International Journal of Imaging Systems and Technology*, 11(1):81–90, 2000.

[135] Punam K Saha, Guoyuan Liang, Jacob M Elkins, Alexandre Coimbra, LT Duong, Donald S Williams, and Milan Sonka. A new osteophyte segmentation algorithm using the partial shape model and its applications to rabbit femur anterior cruciate ligament transection via micro-ct imaging. *IEEE Transactions on Biomedical Engineering*, 58(8):2212–2227, 2011.

[136] Punam K Saha, Yinxiao Liu, Cheng Chen, Dakai Jin, Elena M Letuchy, Ziyue Xu, Ryan E Amelon, Trudy L Burns, James C Torner, Steven M Levy, et al. Characterization of trabecular bone plate-rod microarchitecture using multirow detector CT and the tensor scale: Algorithms, validation, and applications to pilot human studies. *Med Phy*, 42(9):5410–5425, 2015.

[137] Punam K Saha and Jayaram K Udupa. Fuzzy connected object delineation: axiomatic path strength definition and the case of multiple seeds. *Computer Vision and Image Understanding*, 83(3):275–295, 2001.

[138] Punam K Saha and Jayaram K Udupa. Relative fuzzy connectedness among multiple objects: theory, algorithms, and applications in image segmentation. *Computer Vision and Image Understanding*, 82(1):42–56, 2001.

[139] Punam K Saha, Yan Xu, Hong Duan, Anneliese Heiner, and Guoyuan Liang. Volumetric topological analysis: a novel approach for trabecular bone classification on the continuum between plates and rods. *IEEE transactions on medical imaging*, 29(11):1821–1838, 2010.

[140] Punam Kumar Saha and Felix W Wehrli. A robust method for measuring trabecular bone orientation anisotropy at in vivo resolution using tensor scale. *Pattern Recognition*, 37(9):1935–1944, 2004.

[141] Gabriella Sanniti di Baja. Well-shaped, stable, and reversible skeletons from the (3,4)-distance transform. *J Vis Comm Imag Repr*, 5:107–115, 1994.

[142] Heike Scherf and Rico Tilgner. A new high-resolution computed tomography (CT) segmentation method for trabecular bone architectural analysis. *Amer J Phys Anthr*, 140(1):39–51, 2009.

[143] RA Schlenker and WW VonSeggen. The distribution of cortical and trabecular bone mass along the lengths of the radius and ulna and the implications forin vivo bone mass measurements. *Calcified tissue research*, 20(1):41–52, 1976.

[144] William J Schroeder, Jonathan A Zarge, and William E Lorensen. Decimation of triangle meshes. In *ACM Siggraph Computer Graphics*, volume 26, pages 65–70. ACM, 1992.

[145] Ego Seeman and Pierre D Delmas. Bone qualitythe material and structural basis of bone strength and fragility. *New England Journal of Medicine*, 354(21):2250–2261, 2006.

[146] J. Serra. *Image Analysis and Mathematical Morphology*. Academic Press, London, 1982.

[147] Jean Serra. *Image analysis and mathematical morphology, Vol II: Theoretical Advances.* Academic press, New York, NY, 1988.

[148] Mark S Shephard and Marcel K Georges. Automatic three-dimensional mesh generation by the finite octree technique. *International Journal for Numerical methods in engineering*, 32(4):709–749, 1991.

[149] J. Shewchuk. What is a good linear finite element? interpolation, conditioning, anisotropy, and quality measures. *Univ. Cal. Berkeley*, 73, 2002.

[150] Jonathan Richard Shewchuk. Delaunay refinement algorithms for triangular mesh generation. *Computational geometry*, 22(1):21–74, 2002.

[151] Hang Si and A TetGen. A quality tetrahedral mesh generator and three-dimensional delaunay triangulator. *Weierstrass Institute for Applied Analysis and Stochastic, Berlin, Germany*, 2006.

[152] Sajid M Siddiqi, Byron Boots, and Geoffrey J Gordon. A constraint generation approach to learning stable linear dynamical systems. Technical report, DTIC Document, 2008.

[153] MJ Silva and LJ Gibson. Modeling the mechanical behavior of vertebral trabecular bone: effects of age-related changes in microstructure. *Bone*, 21(2):191–199, 1997.

[154] Ivan Sipiran and Benjamin Bustos. Harris 3d: a robust extension of the harris operator for interest point detection on 3d meshes. *The Visual Computer*, 27(11):963–976, 2011.

[155] M. Sonka, V. Hlavac, and R. Boyle. *Image Processing, Analysis, and Machine Vision.* Thomson Engineering, Toronto, Canada, 3rd edition, 2007.

[156] M. Stauber and R. Muller. Volumetric spatial decomposition of trabecular bone into rods and plates–a new method for local bone morphometry. *Bone*, 38(4):475–84, 2006.

[157] M. Stauber, L. Rapillard, G. H. van Lenthe, P. Zysset, and R. Muller. Importance of individual rods and plates in the assessment of bone quality and their contribution to bone stiffness. *J Bone Miner Res*, 21(4):586–95, 2006.

[158] Martin Stauber and Ralph Müller. Volumetric spatial decomposition of trabecular bone into rods and platesa new method for local bone morphometry. *Bone*, 38(4):475–484, 2006.

[159] Martin Stauber and Ralph Müller. A sensitivity analysis of the volumetric spatial decomposition algorithm. *Computer methods in biomechanics and biomedical engineering*, 10(1):25–37, 2007.

[160] Martin Stauber, Laurent Rapillard, G Harry van Lenthe, Philippe Zysset, and Ralph Müller. Importance of individual rods and plates in the assessment of bone quality and their contribution to bone stiffness. *Journal of Bone and Mineral Research*, 21(4):586–595, 2006.

[161] Jian Sun, Maks Ovsjanikov, and Leonidas Guibas. A concise and provably informative multi-scale signature based on heat diffusion. In *Computer graphics forum*, volume 28, pages 1383–1392. Wiley Online Library, 2009.

[162] S. Svensson. Aspects on the reverse fuzzy distance transform. *Pat Recog Lett*, 29:888–896, 2008.

[163] S Tassani, V Korfiatis, and GK Matsopoulos. Influence of segmentation on micro-CT images of trabecular bone. *J Micro*, 256(2):75–81, 2014.

[164] Gabriel Taubin. Linear anisotropic mesh filtering. *Res. Rep. RC2213 IBM*, 1:4, 2001.

[165] The CGAL Project. *CGAL User and Reference Manual*. CGAL Editorial Board, 4.9 edition, 2016.

[166] Chourmouzios Tsiotsios and Maria Petrou. On the choice of the parameters for anisotropic diffusion in image processing. *Patt Recog*, 46(5):1369–1381, 2013.

[167] Jayaram K Udupa, Vicki R LaBlanc, Hilary Schmidt, Celina Imielinska, Punam K Saha, George J Grevera, Ying Zhuge, LM Currie, Pat Molholt, and Yinpeng Jin. Methodology for evaluating image-segmentation algorithms. In *Medical Imaging 2002*, pages 266–277. International Society for Optics and Photonics, 2002.

[168] Jayaram K Udupa and Punam K Saha. Fuzzy connectedness and image segmentation. *Proceedings of the IEEE*, 91(10):1649–1669, 2003.

[169] A Vesterby, HJG Gundersen, and F Melsen. Star volume of marrow space and trabeculae of the first lumbar vertebra: sampling efficiency and biological variation. *Bone*, 10(1):7–13, 1989.

[170] Jan H Waarsing, Judd S Day, and Harrie Weinans. An improved segmentation method for in vivo μCT imaging. *J Bone Min Res*, 19(10):1640–1650, 2004.

[171] Jun Wang and Zeyun Yu. Feature-sensitive tetrahedral mesh generation with guaranteed quality. *Computer-Aided Design*, 44(5):400–412, 2012.

[172] Stuart J Warden, Alexander G Robling, Megan S Sanders, Michael M Bliziotes, and Charles H Turner. Inhibition of the serotonin (5-hydroxytryptamine) transporter reduces bone accrual during growth. *Endocrinology*, 146(2):685–693, 2005.

[173] Nelson B Watts, E Michael Lewiecki, Paul D Miller, and Sanford Baim. National osteoporosis foundation 2008 clinician's guide to prevention and treatment of osteoporosis and the world health organization fracture risk assessment tool (frax): what they mean to the bone densitometrist and bone technologist. *Journal of Clinical Densitometry*, 11(4):473–477, 2008.

[174] Felix W Wehrli, Bryon R Gomberg, Punam K Saha, Hee Kwon Song, Scott N Hwang, and Peter J Snyder. Digital topological analysis of in vivo magnetic resonance microimages of trabecular bone reveals structural implications of osteoporosis. *Journal of bone and mineral research*, 16(8):1520–1531, 2001.

[175] Felix W Wehrli, Glenn A Ladinsky, Catherine Jones, Maria Benito, Jeremy Magland, Branimir Vasilic, Andra M Popescu, Babette Zemel, Andrew J Cucchiara, Alexander C Wright, et al. In vivo magnetic resonance detects rapid remodeling changes in the topology of the trabecular bone network after menopause and the protective effect of estradiol. *Journal of Bone and Mineral Research*, 23(5):730–740, 2008.

[176] Felix W Wehrli, Punam K Saha, Bryon R Gomberg, and Hee Kwon Song. Non-invasive assessment of bone architecture by magnetic resonance micro-imaging-based virtual bone biopsy. *Proceedings of the IEEE*, 91(10):1520–1542, 2003.

[177] Felix W Wehrli, Punam K Saha, Bryon R Gomberg, Hee Kwon Song, Peter J Snyder, Maria Benito, Alex Wright, and Richard Weening. Role of magnetic resonance for assessing structure and function of trabecular bone. *Topics in Magnetic Resonance Imaging*, 13(5):335–355, 2002.

[178] Felix W Wehrli, Hee Kwon Song, Punam K Saha, and Alexander C Wright. Quantitative mri for the assessment of bone structure and function. *NMR in Biomedicine*, 19(7):731–764, 2006.

[179] FW Wehrli, MB Leonard, PK Saha, and BG Gomberg. Quantitative high-resolution mri reveals structural implications of renal osteodystrophy on trabecular and cortical bone. *J Magn Reson Imaging*, 20:83–89, 2004.

[180] Zeyun Yu, Michael J Holst, Yuhui Cheng, and J Andrew McCammon. Feature-preserving adaptive mesh generation for molecular shape modeling and simulation. *Journal of Molecular Graphics and Modelling*, 26(8):1370–1380, 2008.

[181] Andrei Zaharescu, Edmond Boyer, Kiran Varanasi, and Radu Horaud. Surface feature detection and description with applications to mesh matching. In *Computer Vision and Pattern Recognition, 2009. CVPR 2009. IEEE Conference on*, pages 373–380. IEEE, 2009.

[182] Yongjie Zhang and Jin Qian. Dual contouring for domains with topology ambiguity. *Computer Methods in Applied Mechanics and Engineering*, 217:34–45, 2012.

[183] Ying Zhuge, Jayaram K Udupa, Jiamin Liu, Punam K Saha, and Tad Iwanage. Scale-based method for correcting background intensity variation in acquired images. In *Medical Imaging 2002*, pages 1103–1111. International Society for Optics and Photonics, 2002.